The Dissertation Committee for Myungchin Kim Certifies that this is the approved version of the following dissertation:

Design and Operation of Modular Microgrids

Committee:

Ross Baldick, Supervisor

Alexis Kwasinski, Co-Supervisor

Aristotle Arapostathis

Gary Hallock

Robert Hebner

Design and Operation of Modular Microgrids

by

Myungchin Kim, B.S.; M.S.

Dissertation

Presented to the Faculty of the Graduate School of

The University of Texas at Austin

in Partial Fulfillment

of the Requirements

for the Degree of

Doctor of Philosophy

The University of Texas at Austin

August 2015

Acknowledgements

First, I would like to thank my two supervisors, Professor Kwasinski and Professor Baldick, for their continuous and gracious support throughout my graduate studies. Whenever I was struggling either because of academic or personal issues, I was able to find solutions through the discussions with my advisors. I would like to thank Professor Kwasinski for opening my view on microgrids. I learned from him that power electronics could also be studied from a system perspective. His encouragement for taking control or math oriented courses was always a challenge, but did help me to overcome my fear against using math and learning advanced control engineering theory. Furthermore, I would like to thank him for his support and trusting me so that I could work on research with flexibility and a broader view. Based on his continuous support, I could focus more on research. I also thank Professor Baldick for his patience, advice, and support. I am very thankful for his guidance, both academically and personally, regarding the transient period of my studies so that I could finally reach this step. Furthermore, I would also like to thank my other distinguished committee members, Professor Arapostathis, Professor Hallock, and Dr. Hebner. Their advice and continuous support did help my research in many ways, and I cannot forget their warm and positive attitudes whenever I approached them. In addition, I should also thank Malanie Gulick for giving tips and encouragement during my studies in Austin. I was able to realize why her name is frequently mentioned in this section of dissertations written by other colleagues.

I would also like to mention the generous support for this research from the United States Office of Naval Research and Google Inc.

During my studies, I did have a pleasant interaction with the lab-mates in the Power Electronics Research Group (PERG) at UT-Austin. Those include Juyoung Jung,

Hunter Estes, Mahesh Srinvasan, Rossen Tsartzev, JoonHyun Kim, Youngsung Kwon, Amir Toliyat, Vaidynathan Krishnamurthy, Ruichen Zhao, Sheng-Yang Yu, Junsoek Song, Harsha Kumar, and Sungwoo Bae. I would like to specially thank Dr. Bae for helping me during the initial settling and continuous advices, Dr. Krishnamurthy for his energy and valuable feedback during our discussions, Mr. Jung for his help and advice for preparing the experiments, Mr. Kwon, and Mr. Kim for keeping me entertained. My chats with Mr. Estes were also refreshing. The discussions with Mr. Toliyat, Mr. Srinvasan, and Mr. Tsartzev also helped me with understanding power systems. I also would like to thank the other students in the Energy Track for every chat, or short discussion I had. I do believe that I grew either personally or academically by every interaction I had with these brilliant and smart people. Especially, I would like to thank Cheolhee Cho, Duehee Lee, Jihoon Yoon, Kyungwoo Min, Wangi Lee, and Hunyoung Shin. I should also thank Sungpil Yang from the Aerospace department for helping my studies with control engineering.

I also thank the brothers and sisters at the Evergreen Church of Austin for their continuous prayers and inspirations. Especially, I will never forget the good memories with the folks at Mokjang.

I cannot forget my deep thanks to the people at ADD for this opportunity to study abroad.

I would like to thank my father, mother, my parents-in-law, brothers-in-law, sisters-in-law, and my beautiful, lovely, and cute daughter, Jiah. This journey would not have been possible without their support, patience, love and sacrifices. Especially, I feel very sorry for not being with my mother during the last few years, but I believe that God will make her recover. Last but not least, I would like to really thank my wife, Jeongji. As I write down this section, I realize that she was always with me starting from my

undergraduate studies through now, as my friend, girl-friend and eventually my wife. Her continuous support, encouragement, laugh, prayers, and love did make this dissertation to be actually present.

Design and Operation of Modular Microgrids

Myungchin Kim, Ph.D.

The University of Texas at Austin, 2015

Supervisors: Ross Baldick

Alexis Kwasinski

Microgrids are being considered as a solution for implementing more reliable and flexible power systems compared to the conventional power grid. Various factors, such as low system inertia, might make the task of microgrid design and operation to be nontrivial. In order to address the needs for operational flexibility in a simpler manner, this dissertation discusses modular approaches for design and operation of microgrids.

This research investigates Active Power Distribution Nodes (APDNs), which is a storage integrated power electronic interface, as an interface block for designing modular microgrids. To perform both voltage/current regulation and energy management of APDNs, two hierarchical control frameworks for APDNs are proposed. The first framework focuses on maintaining the charge level of the embedded energy storage at the highest available level to increase system availability, and the second framework focuses on autonomous power sharing, and storage management. The detailed design process, control performance and stability characteristics are also studied. The performance is also verified by both simulation and experiments. The control approaches enable application of APDNs as a power router realizing distributed energy management. The decentralized

configuration also increases modularity and availability of power networks by preventing single point-of-failures.

The advantages of using APDNs as a connection interface inside a power network are discussed from an availability perspective by performing a comparison using Markov-based availability models. Furthermore, the operation of APDNs as power buffers is explored and the application of APDNs enabling modular implementation of microgrids is also studied. APDNs enable the system expansion process—i.e. connecting new loads to the original system—to be performed without modifying the configuration of the original system. The analysis results show that a fault-tolerant microgrid with an open architecture can be realized in a modular manner with APDNs. APDNs also enable simplified selectivity planning for system protection.

The effect of modular operation on microgrids is also studied by using an inertia index. The index not only provides insights on how system performance is affected by modular operation of modular microgrids, but is also used to develop a simpler operation strategy to mitigate the effect of plug and play operations.

Table of Contents

List of Tables

List of Figures

Chapter 1. Introduction

1.1 MICROGRIDS

The development of power electronics and storage technology enabled the advent of microgrids with advanced functionalities compared to conventional power systems. Examples include systems that have both directly connected generators and inverter-interfaced sources [1], power networks for data centers [2], power systems with renewable energy sources [3], and electric ships [4]. To verify and enhance the performance of microgrids, various demonstration sites are also reported worldwide [5], [6].

According to [7], microgrids can be defined as the following.

"A microgrid is a group of interconnected loads and distributed energy resources within clearly defined electrical boundaries that acts as a single controllable entity with respect to the grid. A microgrid can connect and disconnect from the grid to enable it operate in both grid-connected or island-mode" [7].

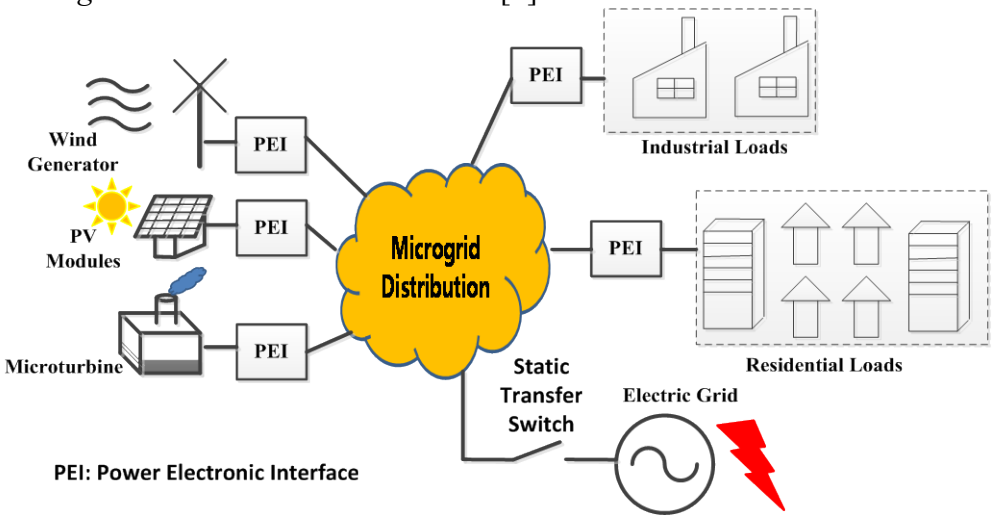

Fig. 1.1. Example of a general microgrid

As implied from the definition, examples of benefits by operating a microgrid compared to conventional centralized power systems include higher operational flexibility, and improved system availability. For instance, the local loads could be operated by the sources without being affected by the state of the main electric grid. Based on the flexibility, furthermore, it is possible to optimize the operation of the system through proper control.

However, there are several challenges with microgrid operation. The smaller system inertia value [8], and relatively small size of microgrids [9] are examples of such challenges. Microgrids are expected to have high participation of sources and loads equipped with power electronic interfaces (PEIs) [10], [11]. Although PEIs are effective for connecting different type of sources and loads to build a microgrid, these interfaces can also be a cause of stability issues in a power network. Stability issues can be attributed to the limited inertia of PEIs compared to synchronous generators [12]. In addition, the negative incremental input impedance behavior observed at the terminals of tightly regulated converters [13] is also a known factor that affects microgrid stability.

Microgrids can also be exposed to significant power imbalances between sources and loads [10]. For example, the power output of renewable sources can be affected by external conditions, such as passing clouds affecting photovoltaic arrays. Considering power system stability is highly linked to the power balance [14], this power imbalance can also cause stability problems. The relatively small size of microgrids may increase the difficulty of handling stability issues caused by this imbalance. This power imbalance can also be a major factor that can make the system expansion design process—e.g. connecting future loads to the microgrid as shown in Fig. 1.2—to be nontrivial, making difficult to realize microgrids with open architectures.

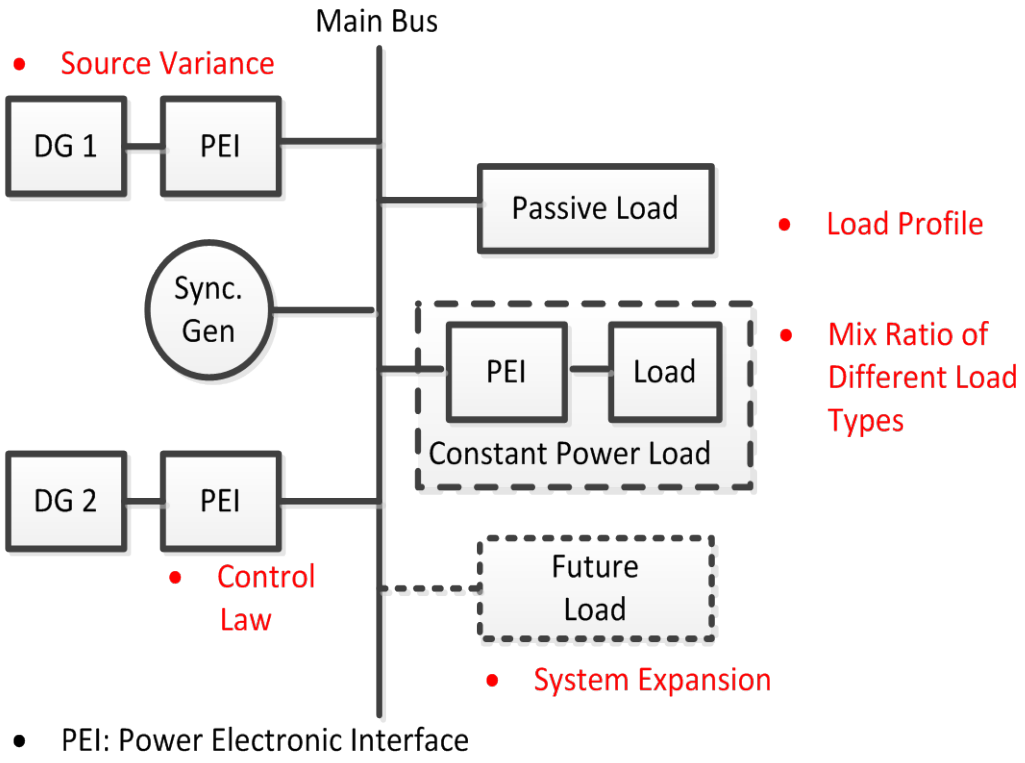

Fig. 1.2. Examples of factors affecting microgrid stability

1.2 Power Network Availability

Higher level of availability is one of the key benefits of microgrids. Highly available power supply is also essential for power systems of critical facilities such as hospitals [15], military bases [16], [17], and data centers [2]. Vehicles and aircrafts should also be designed so that the performance of safety critical functions is not affected by failures at the power distribution level [18], [19]. The interest for implementing a highly available power distribution grid has continuously increased after experiencing extensive black-outs during natural disasters [20]. These extensive and long outages often happen with relatively minor damage in power grids, suggesting an important fragility particularly in the distribution portion of the grids [21]. These power distribution issues

originate in the primarily centralized power generation architecture of power grids—few large power plants serve many more small loads—and the lack of power path redundancy in most sub-transmission and distribution-level circuits.

Traditional mitigation strategies to handle this issue include tree trimming programs, and use of underground infrastructure. Another approach is planning of aerial power distribution architectures with alternative power paths, such as ring or laddered configurations. However, circuit protection coordination and selectivity planning in these configurations is usually very complex, particularly as more distributed generation technologies are deployed at the distribution level of power grids. Moreover, series faults cannot be easily detected with only fuses or circuit breakers and it is difficult to achieve an effective current interruption using conventional circuit protection devices in dc power architectures. These issues are expected to be more prevalent as interest in using microgrids and dc power systems to achieve higher availability grow, supported by the increased use of power electronic interfaces [4], [22] as exemplified in Fig. 1.3.

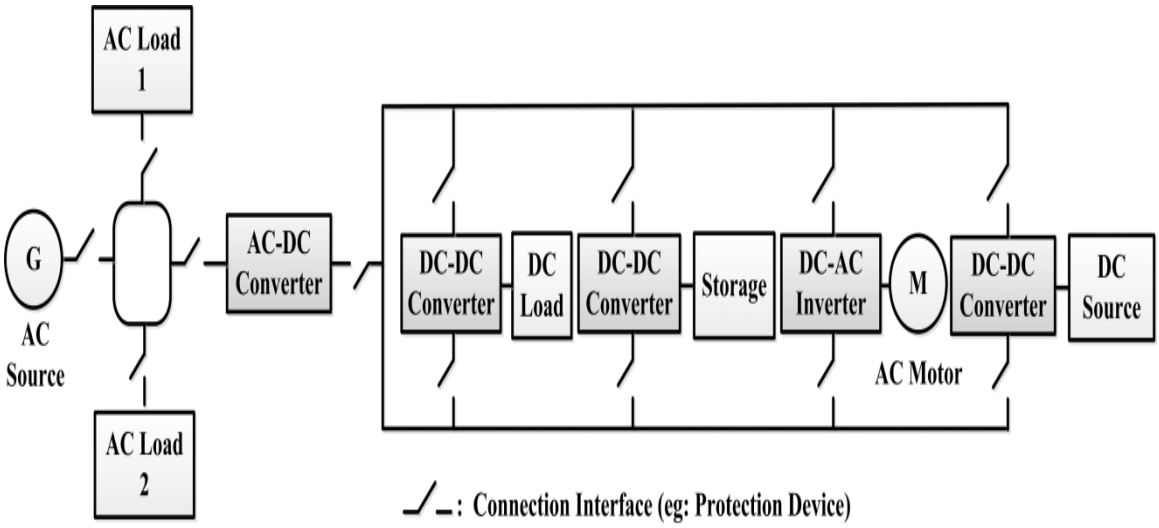

Fig. 1.3. Example of a Power Distribution Architecture

Therefore, it is evident that improving power distribution reliability and availability in a more cost effective way than burying infrastructure and with an increased deployment of power electronic interfaces will be the focus receiving increased attention in the future. Hence, it is expected that power electronic circuit performance is one of the key factors affecting power distribution availability in future power grids.

1.3 RESEARCH DIRECTION

To have higher operational flexibility, microgrids are likely to experience change in the configuration. Possible examples include connection of future loads or addition/removal of power sources. Because of the previously discussed challenges of microgrids, design and operation of microgrids to accommodate these configuration changes might be nontrival, making the realization of microgrids with open architectures a difficult problem. This can limit the operational flexibility of microgrids, which is one of the main characteristics and benefits of operating a microgrid. Therefore, it is necessary to seek approaches that enable modular design and operation of microgrids that can maximize operational flexibility—i.e. plug-and-play operation.

This study considers a storage integrated power electronic interface, named as Active Power Distribution Node (APDN), as a modular interface block for design and operation of modular microgrids. The conceptual diagram of an APDN is shown in Fig. 1.4. By having multiple interface ports that have bidirectional power flow capability and embedded energy storage, APDNs are able to increase both operational flexibility and availability of power networks. This dissertation studies the operation principle and characteristics of APDNs. The research, furthermore, proposes two hierarchical control strategies for APDN control and its application as an interface block for modular

microgrids. The advantages and design considerations of using APDN as a connection interface for microgrids are also explored.

This research also studies the effect of modular operation on the performance of microgrids. This dissertation studies an approach using an inertia index. The considered index provides insights on how the microgrid performance could be affected by source configuration changes in a modular microgrid.

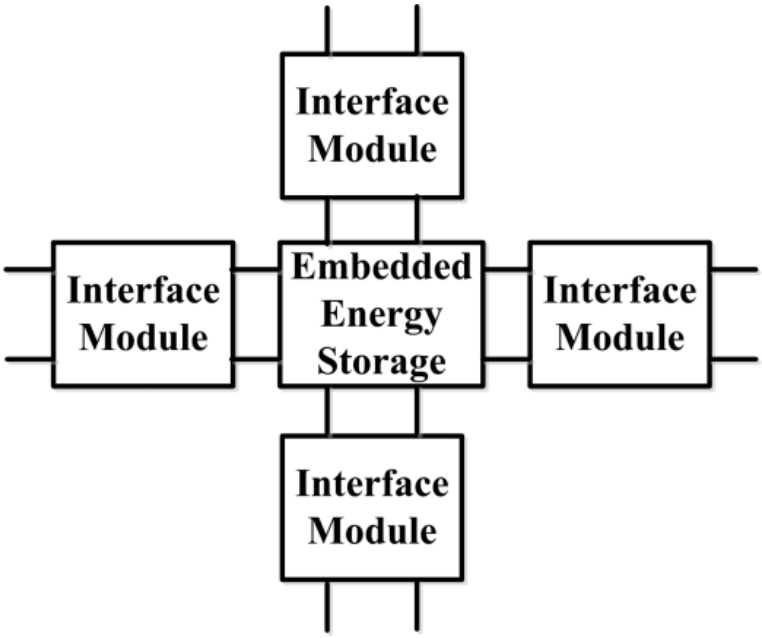

Fig. 1.4. Conceptual block diagram of an APDN

1.4 LITERATURE REVIEW AND CONTRIBUTIONS

This section reviews the literature on the topics relevant to the research conducted in this dissertation. The contributions and achievements of this study compared to previous work are also introduced.

1.4.1 Integrated Power Electronic Interface

Integrated power electronic interfaces can be realized by multi-port circuit topologies. Representative multi-port circuit topologies include parallel connected converters [23], interleaved converters [24], multiple input converters [25], multiple output converters [26], and multiple input-multiple output converters [27]. These topologies differ from each other depending on which component is shared among different interface ports and whether the interface ports can transfer power simultaneously or in a time-multiplexed manner. These multi-port circuit topologies could be used to implement a modular microgrid architecture. For example, Fig. 1.5 shows a microgrid implemented using a multiple input converter [25]. The modular configuration enables to accommodate the changes in the number of sources by simply adding or removing input cells as shown in Fig. 1.5.

While most of the previous studies on microgrids consider connecting sources and loads to the main bus through separate single-input single-output (SISO) converters, it is beneficial to consider implementing a microgrid using a power electronic interface integrated with multiple bidirectional ports. Such an integrated interface can show potential benefits such as higher operational flexibility, and system availability [27], [28], [29]. It can also enable realizing microgrids with an open modular architecture. In addition, the number of power conversion stages can be minimized so that efficiency can be improved.

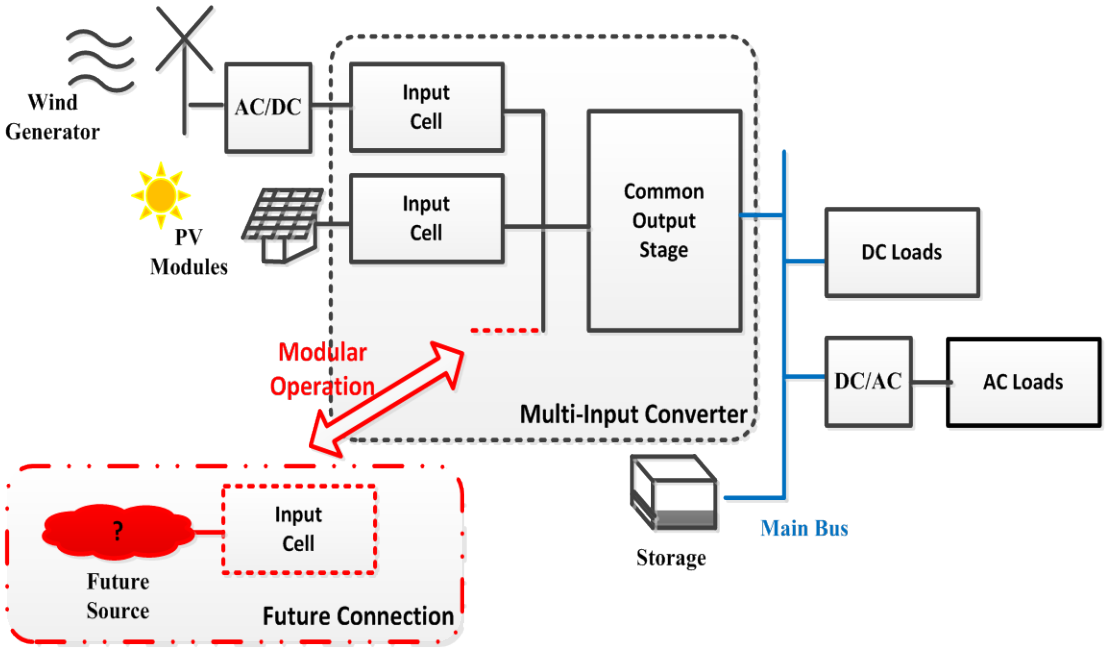

Fig. 1.5. Example of a Microgrid implemented with a Multi-Input Converter

Such an integrated interface can also perform a role as a power router [30], in the sense that the power flow of each input/output port can be actively controlled. Furthermore, a modular design approach for microgrids can be developed by using the integrated interface as a building block.

Several studies proposed a power electronic interface that can be used as a power router for microgrids. For example, [31] considers using a solid-state transformer (SST) as a power router. The microgrid design based on using a SST for connecting ac sources and dc loads are presented with simulation results [31]. A multiple-input multiple-output (MIMO) converter that has ports with bi-directional power flow capability using a SEPIC topology is introduced in [29]. The operation principle and its application for microgrids are also introduced [29]. Although [29] discusses application of the interface for building a highly available power network, the interface can also be used to perform power routing between the connected sources and loads based on the proposed time-

multiplexing switching scheme. Different type of integrated interfaces that can also be used as a power router of a microgrid can be found from the research results on converters with multiple interface ports [32], [33]. The study of [32] proposed a dc MIMO interface for dc transmission systems. Each interface port is connected to a common ac bus through a LCL filter. Reference [33] introduces a resonant MIMO power converter with a high frequency link. The power of each input leg is transferred to the output leg in a sequential manner through a pair of an inductor and a capacitor.

Compared to these previously mentioned interfaces, the interface studied in this research, APDNs, has the advantages of both energy storage in terms of resiliency and power electronics circuits in term of flexible control. APDNs not only perform power routing but also can work as a power buffer that can handle instantaneous power imbalance between sources and loads thanks to its embedded energy storage. In addition, the energy storage can be used as a secondary power source when the source is not available, thus, providing some limited failure ride through capabilities. Furthermore, APDNs enable open architecture designs because in case the microgrid hardware configuration needs to be modified—e.g. addition or removal of interface modules—such modifications could be easily addressed in a modular fashion.

1.4.2 Control of Multi-Port Power Electronic Interfaces

Controllers for multi-port topologies should consider additional objectives other than regulation performance, such as load sharing between different ports. Examples of control frameworks proposed for multi-port topologies include droop [34], master-slave [35], and average current [36] control. Among these approaches, droop control can perform both power sharing between different sources and voltage regulation by sensing

local variables only [37]. Droop control application examples are reported for both ac [1], [37] and dc systems [3], [38], [39]. The droop laws of both systems are shown in Fig. 1.6, 1.7, and 1.8. In case of dc systems (Fig. 1.6), the droop law can be designed so that the voltage reference value droops as the current increases. The droop law for ac systems (Fig. 1.7 (a)) can also be designed in a similar fashion as shown in Fig. 1.7(b). It is worth to note that the droop law for ac systems depends on the cable characteristics (i.e. R/X ratio). Instead of the *P-f*, *Q-V* droop law, in case the cable is highly resistive, the reverse droop law should be considered as shown in Fig. 1.8 [40]

Droop control is used to perform both voltage regulation and power sharing between different energy sources in a microgrid [39]. The power sharing ratio between sources is determined by the droop slope of each source. Although high droop gains can improve the accuracy of power sharing [41], the stability margin decreases as the droop gain increases [38], [41]. A supplementary loop for the linear droop law was developed to ensure system stability even with high gains in [41]. Alternative approaches for improving droop control load sharing performance include adaptive droop laws that depend on the load power level [42], or compensators that shapes the output impedance [43], [44].

Microgrids can be controlled by using a hierarchical control framework [37], [45], which includes decentralized control for distributed generation sources and voltage regulation. This framework has a control hierarchy in which the primary level establishes load sharing between different sources according to a droop law, and a higher level adjusts the voltage deviation caused by the droop law of the primary level controller or control the power flow between the microgrid and an utility gird tie. Instead of the voltage, studies that consider restoration of frequency or minimizing voltage unbalance are also reported using this control framework [45].

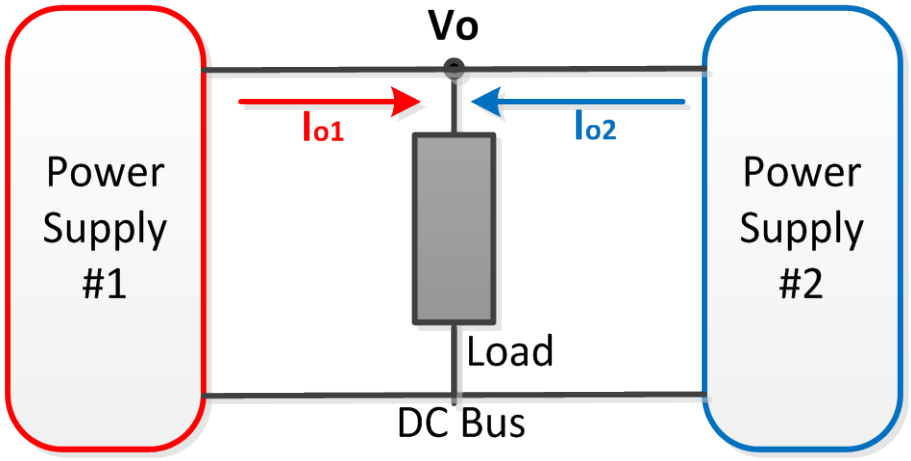

(a) System Configuration

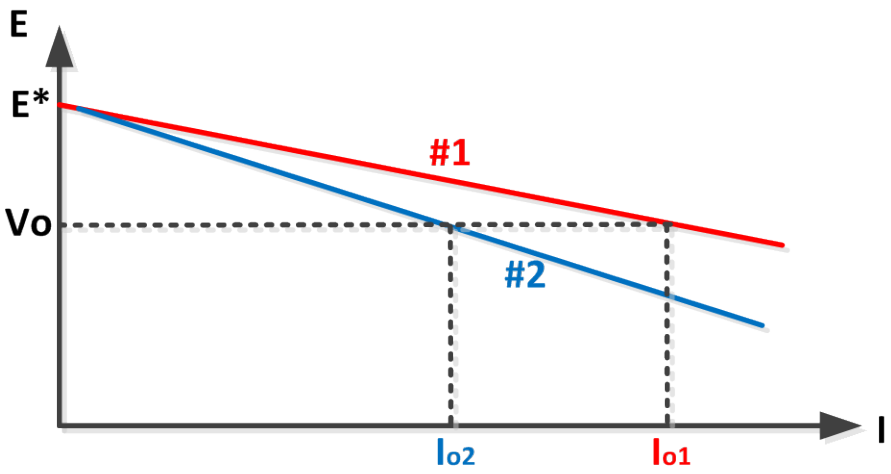

(b) Droop Curve (V-I)

Fig. 1.6. Droop Law for dc Microgrids

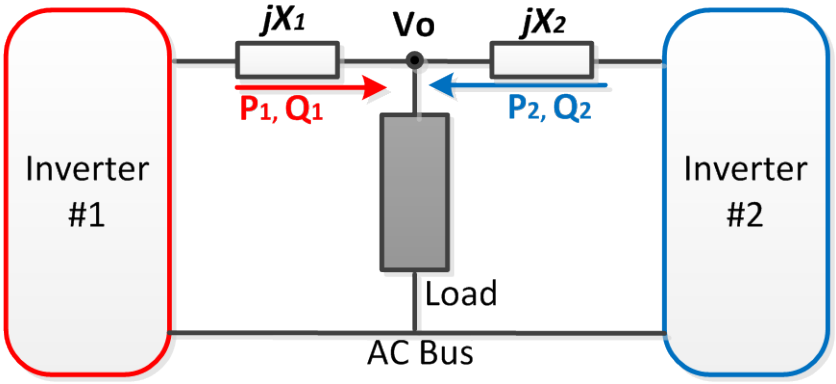

(a) System Configuration

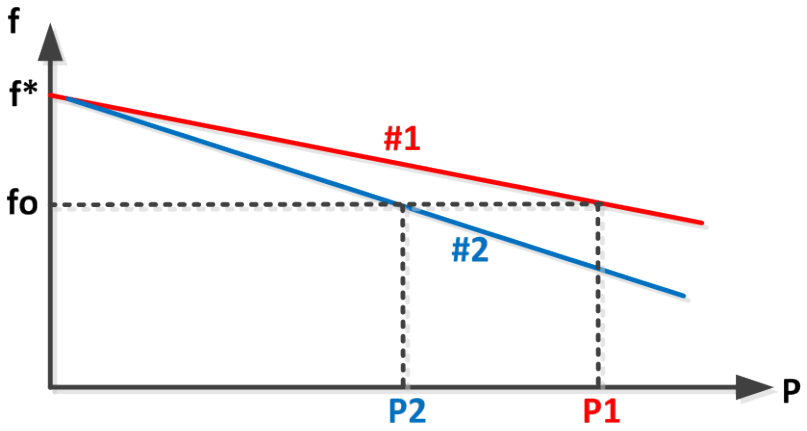

(b) Droop Curve (*P-f*)

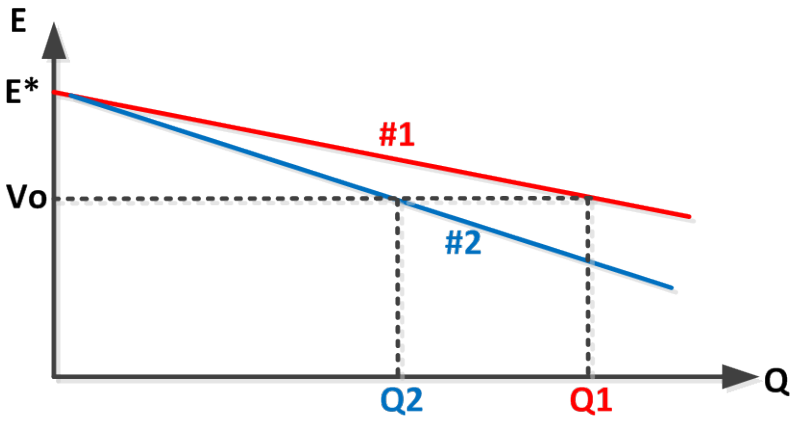

(c) Droop Curve (*Q-E*)

Fig. 1.7. Droop Law for ac microgrids (Inductive)

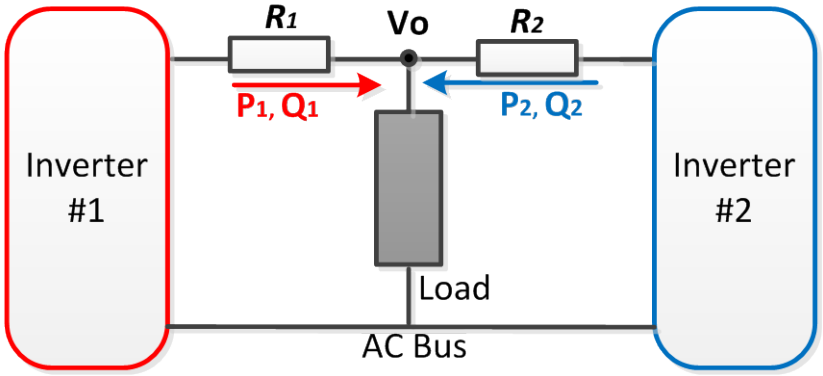

(a) System Configuration

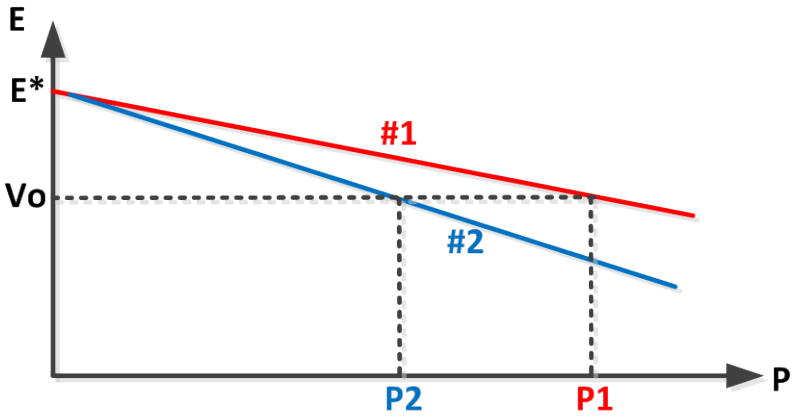

(b) Droop Curve (*P-E*)

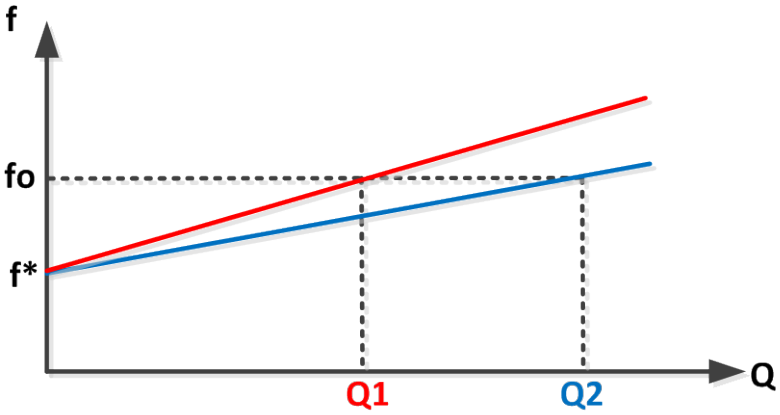

(c) Droop Curve (*Q-f*)

Fig. 1.8. Droop Law for ac microgrids (Resistive)

While a droop based decentralized control approach has been typically considered in the hierarchical control framework [37], studies that use distributed control approaches for microgrid control were also reported [46]-[52]. Satisfactory performance of both load sharing and voltage regulation could be achieved based on the communication of local information between different units—e.g. generation units or interface modules. Examples of the communicated information include the current [46], [47], and the output voltage [47]. The use of distributed cooperative control approaches were also reported for modular converters [48], [49] and microgrids [50]-[52]. For example, reference [50] studies the application of cooperative control for current sharing in parallel connected dc converters. A cooperative control framework for modular converters that could be applied with different communication link topologies between the individual modules is proposed in [49]. For dc microgrids, a control approach is developed so that each unit is equipped with a control law that uses data of neighboring units to perform both voltage and current regulation [50]. The application of distributed control was also reported for ac microgrids [51], [52].

Since APDNs could be viewed as an interface that is a composition of identical interface modules, this research studies a decentralized [53] hierarchical control approach for APDNs. Although droop control has been studied in the past in many applications [38], [39], [41]-[44], their use to control distribution-level power electronic circuits with embedded energy storage seem to not have been sufficiently explored in the past.

Compared to the full-state feedback approach [27], the proposed approach of this study is able to both control power flow and perform storage management in a decentralized manner through droop control. It should be noted that a centralized power management algorithm [54] is not required to perform storage management. Hence, the control approach increases modularity, and reduces communication burden between

interface modules. As a result, potential single point of failures for the entire system are avoided. The considered control approaches could also be effectively used for both operation modes of the interface module—i.e. input module and output module. The control approach provides a method to either enable autonomous load sharing between input modules or provide active damping to handle constant power loads that might be connected in series to an output module. The control framework of this study also performs management functions for the embedded energy storage that is directly connected to every interface module as shown in Fig. 1.4. Although studies on interfaces that have a battery directly connected to the power stage have been reported in the past, these studies have limitations such as not discussing regulation of battery voltage [55], [56], or considering only a single power source [57]. This research explores both battery current and voltage regulation which are commonly needed for batteries.

1.4.3 System Availability and Power Electronics Interface

A typical approach for quantifying reliability performance of a power electronic interface is by using the part count technique based on failure rate data from handbooks [58]-[60]. The failure rate of each component is calculated by considering various factors such as quality grade, device ratings, electrical stress, and environmental conditions [61]. To achieve a more realistic prediction of failure rates, approaches of using actual or simulated environment data for calculating the operation conditions were also reported [62], [63]. By using the calculated failure rate of each component (e.g., power switches, and capacitors), it is possible to evaluate the reliability performance of power converters for various applications, such as grid connected PV systems [64], hybrid electric vehicles [65], wind power systems [62], and aircraft systems [66].

However, component failure rates—i.e. reliability—provide limited information about system performance. Instead, availability should be considered as a metric for quantifying how systems perform [28]. This is based on the fact that a typical power system can be viewed as a repairable system consisting of multiple components. Availability includes the effect of not only failure rates, but also repair rates, which are affected by external factors such as maintenance policy, logistics, and system architecture [28]. This notion of availability can be explained with an extreme example in which if a perfect maintenance policy is applied—i.e. a system is repaired as soon as a fault is detected and a fault is detected as soon as a fault happens—it is possible to have a system with high availability using components with low reliability. Examples of calculating power system availability are reported for applications such as microgrids [28] and PV systems [67].

This dissertation discusses the advantages of using APDN, which is a storage integrated power electronic interface, as a connection interface inside a power network from an availability point of view in a quantitative manner by performing a comparison using Markov-based availability models. The advantages of both power electronic interface and embedded energy storage are demonstrated through availability analysis and cost analysis.

1.4.4 Stability of Microgrids

In order to ensure stable operation of microgrids, various studies have been performed on microgrid stability [68], [69]. Figure 1.9 shows examples of research topics of interest for each unit in the microgrid.

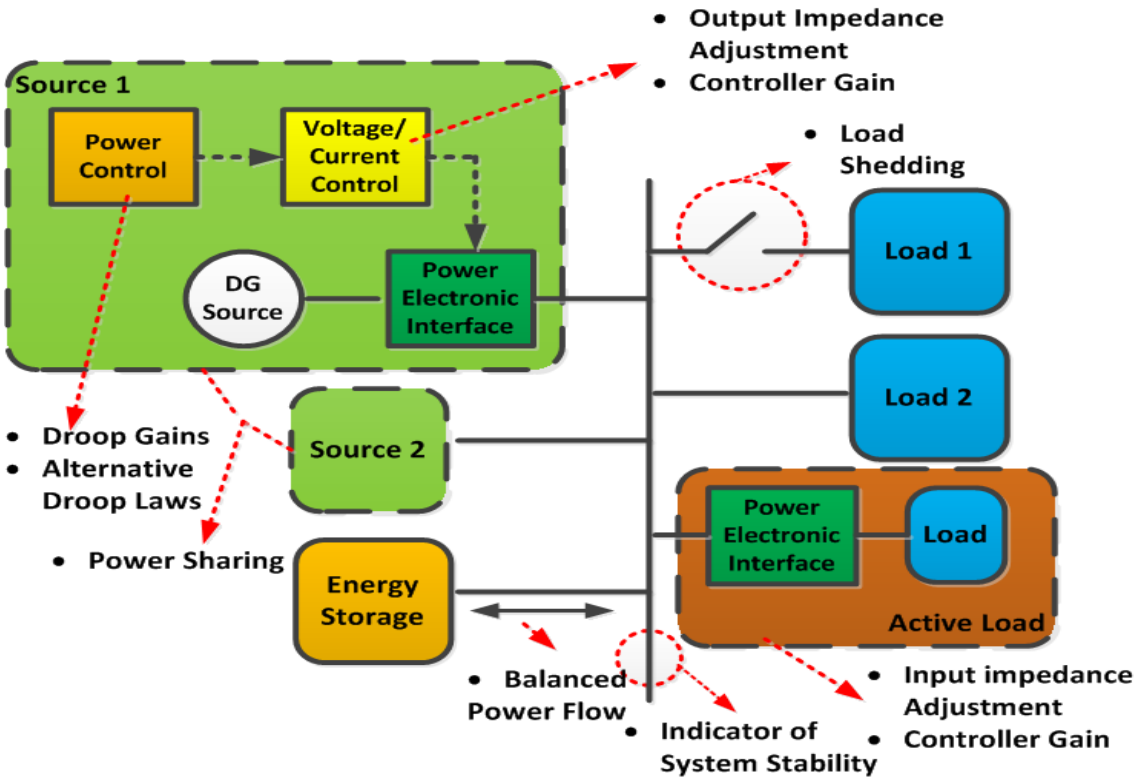

Fig. 1.9. Research Topics Related to Stability of Microgrids

Most of the studies focus on performing an analysis on how system parameters can affect system stability or developing a control law or an energy management policy to ensure system stability. Examples of parameters that affect microgrid stability include droop gains [1], [70], controller gains [71], and the resistance/inductance of connection cables [72]. Results of [70] show that the system becomes unstable as the frequency droop gain increases. Based on eigenvalue analysis, it was shown that system damping is affected by the controller gains of a constant power load [71].

To ensure stable operation of microgrids, control law development for power electronic interfaces has also been a major research topic [73]. Examples of proposed control approaches include droop laws using the derivative of power [42], adding supplementary control loops [41], and modifying the output impedance characteristics of

the power electronic interface [74]. While the linear droop law (e.g., *P-f*, *Q-V* for inductive grid and *P-V*, *Q-f* for resistive grid) is the most popular approach considered for droop control, the use of alternative droop laws could improve the transient response [12] or enable using higher droop gains [41] with an objective to enhance the load sharing performance. Based on the fact that the output impedance of a power electronic converter could be modified by the control law, approaches that change the output impedance characteristics to be either more resistive [75] or inductive [45] are considered so that droop laws could be more effectively used without being affected by the coupling between active power and reactive power. The output impedance is changed by introducing a virtual impedance term in the control loop as shown in Fig. 1.10. Instead of a fixed value, a time-variant virtual impedance could also be considered to ensure safe operation during mode transitions or start-up process [37].

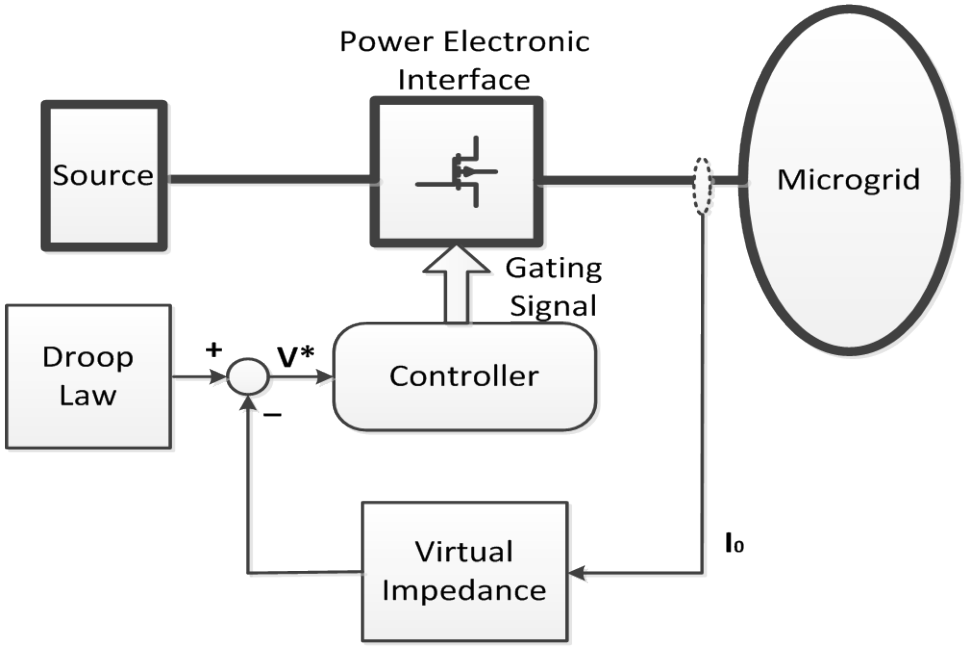

Fig. 1.10. Block diagram for virtual impedance implementation

From a system level perspective [76], [77], topics such as exploring stability indicators of microgrids, and development of energy management algorithms to reduce the power imbalance at the system level have also been reported. Based on the fact that bus voltage or system frequency provides information regarding system stability [9], [77], it is possible to switch the operation mode or manage the load based on the level of the voltage and frequency. For example, reference [78] uses the dc bus value to perform transitions between different operation modes to ensure power balance of a modular PV power system with energy storage. In order to minimize power imbalances between the sources and the loads, approaches of storage installation [76] and load shedding [79] have been reported.

1.5 ORGANIZATION OF DISSERTATION

This dissertation is organized as follows. Chapter 2 introduces the configuration and operation states of the APDN. A control strategy for power regulation and energy management is also proposed. Chapter 3 introduces a hierarchical control approach for an APDN with a hybrid embedded energy storage. Chapter 4 discusses aspects from a system point of view by considering APDNs as a system connection interface. The focus of discussion is on system availability and study of using APDN as an interface block that enables modular design of microgrids. Chapter 5 studies the effect of plug and play operation in modular microgrids. An inertia index is defined to predict the change in the microgrid performance. Finally, Chapter 6 concludes the dissertation by summarizing the contributions of this research, and suggesting directions of future work.

Chapter 2. Active Power Distribution Nodes (APDNs)

2.1 Configuration and Characteristics

As shown in Fig. 2.1, an APDN consists of a power electronic circuit with multiple bidirectional interface modules and an embedded energy storage. Each interface module has one of its ports connected to the embedded energy storage for back up and power buffering functions. The other port can be connected to various components, such as power sources, loads or energy storage. Each interface module operates either in buck or boost mode depending on the power flow direction [27].

The embedded energy storage can be of any type depending on application needs, such as high energy density and high power density [80]. In this study, a hybrid parallel connection of a battery and a capacitor is considered for embedded energy storage as shown in Fig. 2.1. This hybrid configuration is known to have advantages because the capacitor can balance transient power differences and reduce excessive cycling that affects battery life [30]. It is worth to note that the level of improvement in performance (e.g., providing higher peak power, lower level of power loss) by considering a hybrid energy embedded energy storage differs depending on how the energy storage is configured [81].

The embedded energy storage can be connected either directly or indirectly to the dc-link as shown in Fig. 2.2. For example, a flywheel storage system should be connected through a power electronic interface to the dc-link. Although indirect connection may increase control flexibility and protection capability of the storage device, it may also act as a single point of failure. In case of a sudden power imbalance, the direct connection may show faster response compared to the indirect connection. In addition, direct connection can save the costs for extra power electronics and controllers. A more detailed comparison between connection methods is introduced in [82].

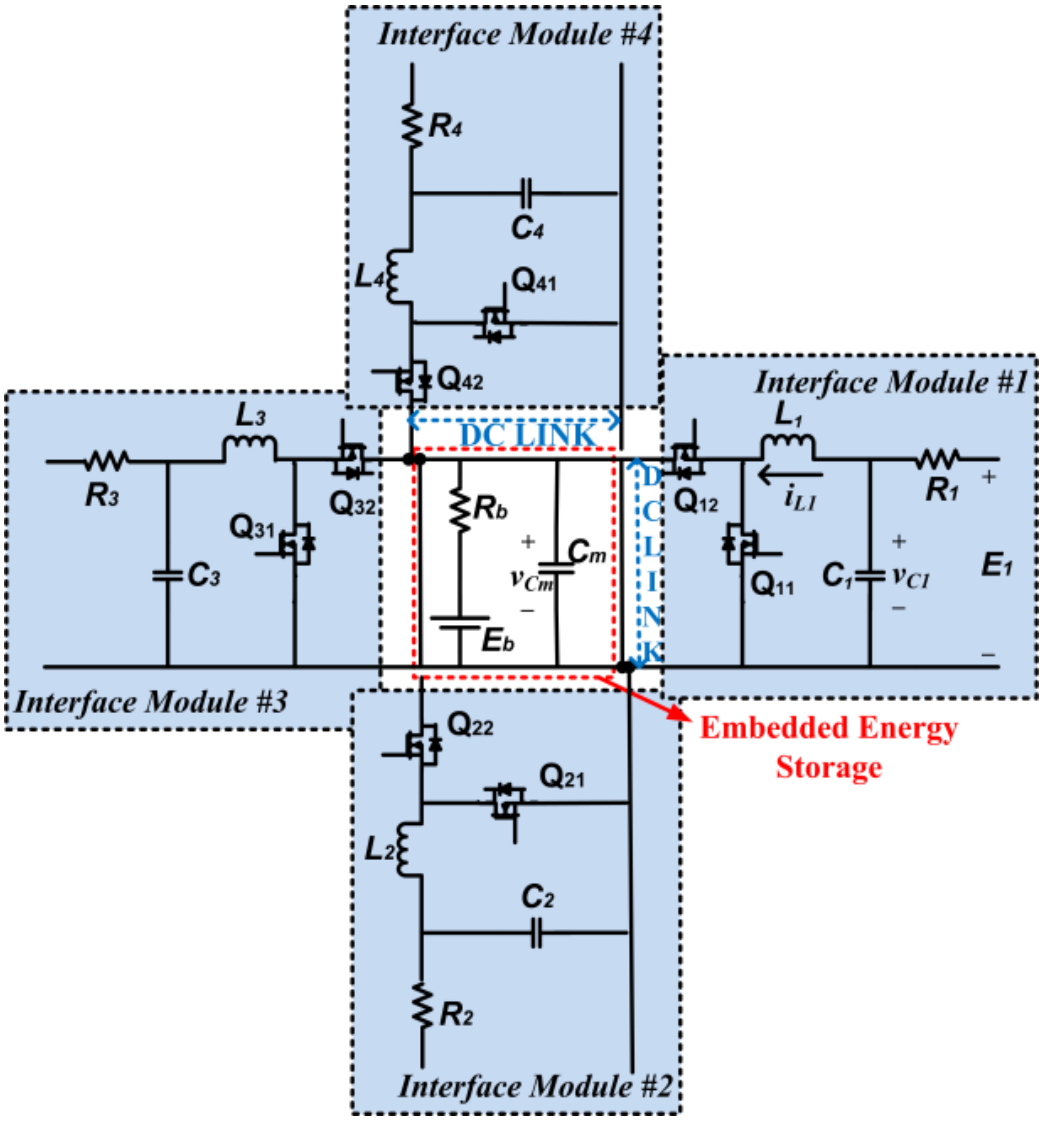

Fig. 2.1. Configuration of APDN

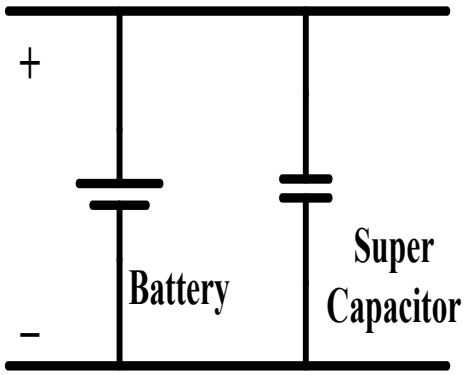

(a): Direct Connection

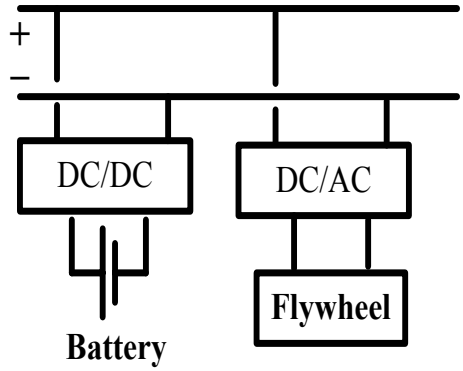

(b): Indirect Connection

Fig. 2.2. Options of Embedded Energy Storage Connection within APDN

Compared to other integrated power electronic interfaces, the embedded energy storage enables the APDN to work as a power buffer. Although the voltage/current of each interface module is tightly regulated and the interface modules are connected in series, with proper control the embedded energy storage works as a mechanism to prevent the dc-link stage voltage from experiencing oscillations caused by constant power loads [13]. The embedded energy storage can also address unbalances between sources and loads. For the configuration in Fig. 2.1, the power balance relationship between sources, loads, and energy storage can be written as

$$C \cdot V_{dc} \cdot \frac{dV_{dc}}{dt} + \frac{dE}{dt} = P_S - P_L = \Delta P \tag{2.1}$$

where V_{dc} is the voltage of the dc-link stage, E is the energy of the battery, Ps is the source power and P_L is the load power. Rewriting (2.1),

$$C \cdot V_{dc} \cdot \Delta V_{dc} + \Delta E = \Delta P \cdot \Delta t \tag{2.2}$$

$$\Delta V_{dc} = \frac{\Delta P \cdot \Delta t - \Delta E}{C \cdot V_{dc}} \tag{2.3}$$

Equation (2.3) shows that the direct connection of the battery to the dc-link stage ensures that if the source power is higher than the load power ($\Delta P>0$), the battery will absorb the energy ($\Delta E>0$). In case that $\Delta P<0$, the battery will handle the difference so that $\Delta E<0$. Thus, it can be seen from (2.3) that the variation of the dc-link voltage, which can be considered as an indicator of power balance of a system [9], is minimized. Hence, unbalancing issues can be addressed by installing an embedded energy storage that can handle long term power differences. Therefore, the energy storage devices in the APDN act as a distributed component analogous to rotors of large synchronous generators in conventional power grids and the relationship between frequency and power imbalances.

As shown in Fig. 2.3, APDNs acting as power buffers can perform a role analogous to that of Internet data routers by being placed in key nodes of a power distribution architecture. While data routers manage bit rate differences between the network and the user by using data storage, power buffers can handle power mismatch between sources and loads by utilizing energy storage [30]. As power buffers, APDN can

increase operational flexibility by decoupling the dynamics between sources and loads [4]. Such a decoupling also enables a modular approach for system planning and expansion [8]. Furthermore, selectivity planning in advanced power architectures for system protection can be performed in a simplified manner by using APDN compared to conventional approaches [4]. To perform roles of power routers, APDNs should be designed to have multiple interface paths and handle power flow differences among power distribution paths. For example, the power variation in renewable sources could cause power imbalance if connected to a fixed load.

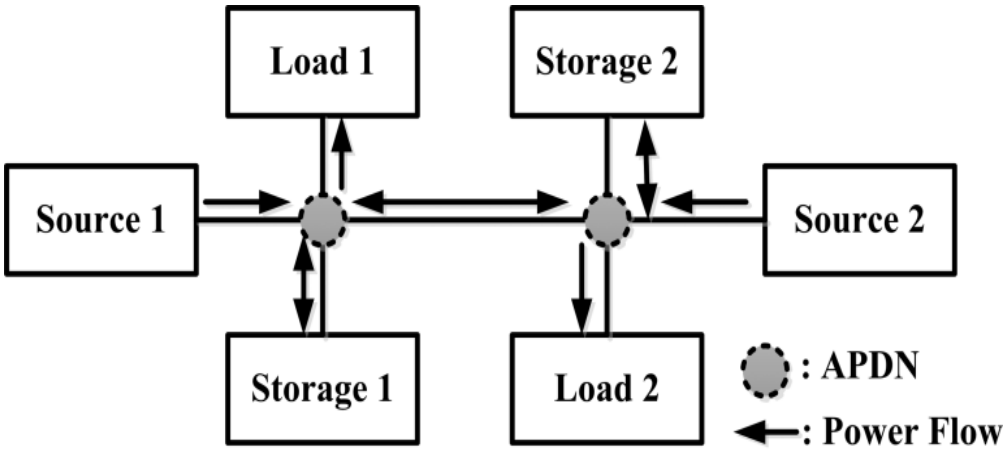

Fig. 2.3. Example of a microgrid with APDNs used as a power router

2.2 SYSTEM MODEL

Since an APDN is a parallel connection of multiple interface modules, it is beneficial to find the system model of a single interface module. Although the interface module can operate either in buck mode or boost mode, a modeling approach introduced in [83] can be used to derive a single unified model regardless of its operation mode. Consider interface module *#1* of Fig. 2.1 for modeling purposes. The control input is the switch connected in parallel with the capacitor of each interface module. In case of interface module *#1*, the control is applied by controlling the duty cycle of switch Q_{11}. Switching of Q_{12} is done in a complementary manner with respect to Q_{11}.

The state space model of interface module #1 is:

$$L_1 \frac{di_{L1}}{dt} = v_{C1} - (1-q)v_{Cm} \tag{2.4}$$

$$C_1 \frac{dv_{C1}}{dt} = \frac{E_1 - v_{C1}}{R_1} - i_{L1} \tag{2.5}$$

$$C_m \frac{dv_{Cm}}{dt} = \frac{E_b - v_{Cm}}{R_b} + (1-q)i_{L1} \tag{2.6}$$

where i_{L1} is the current through inductor L_1, v_{C1} and v_{Cm} is the voltage across capacitor C_1 and C_m, respectively, R_b is the internal resistance of the battery, E_b and E_1 are the open circuit voltage level of the battery and voltage level of the input source and q is the switching function of Q_{11}.

By applying state-space averaging to (2.4)-(2.6), and by defining the state variable vector as $\hat{\boldsymbol{x}} = [\hat{x}_1 \quad \hat{x}_2 \quad \hat{x}_3]^T = [\hat{\imath}_{L1} \quad \hat{v}_{C1} \quad \hat{v}_{Cm}]^T$, and the control input as $\hat{\boldsymbol{u}} = [\hat{d}_1]$, the small-signal model of an interface module can be expressed as

$$\dot{\hat{\boldsymbol{x}}} = \boldsymbol{A}\hat{\boldsymbol{x}} + \boldsymbol{B}\hat{\boldsymbol{u}} \tag{2.7}$$

$$\hat{\boldsymbol{y}} = \boldsymbol{C}\hat{\boldsymbol{x}} + \boldsymbol{D}\hat{\boldsymbol{u}} \tag{2.8}$$

where $= \begin{bmatrix} 0 & \frac{1}{L_1} & \frac{D_{eq}-1}{L_1} \\ -\frac{1}{C_1} & -\frac{1}{R_1 C_1} & 0 \\ \frac{1-D_{eq}}{C_m} & 0 & -\frac{1}{R_b C_m} \end{bmatrix}$, $\boldsymbol{B} = [V_{Cm}/L_1 \quad 0 \quad -I_{L1}/C_m]^T$, $\boldsymbol{C} = \mathbf{I}$ (the identity matrix), and $\boldsymbol{D} = [0 \quad 0 \quad 0]^T$, V_{Cm} and I_{L1} are the values of the voltage across C_m and current through L_1 at the equilibrium point. It should be noted that $\hat{d}_1$is the perturbed duty ratio of switch Q_{11} around D_{eq}, which is the duty ratio at the equilibrium point.

The transfer function matrix between the control input and three outputs can be found as

$$\mathbf{G}(\mathrm{s}) = \boldsymbol{C}[s\boldsymbol{I} - \boldsymbol{A}]^{-1}\boldsymbol{B} + \boldsymbol{D} = \begin{bmatrix} \frac{\hat{\mathrm{I}}_{\mathrm{L}}(\mathrm{s})}{\hat{\mathrm{D}}_1(\mathrm{s})} & \frac{\hat{\mathrm{V}}_{\mathrm{C1}}(\mathrm{s})}{\hat{\mathrm{D}}_1(\mathrm{s})} & \frac{\hat{\mathrm{V}}_{\mathrm{Cm}}(\mathrm{s})}{\hat{\mathrm{D}}_1(\mathrm{s})} \end{bmatrix}^T \tag{2.9}$$

where s is the Laplace transform operator, $\hat{\mathrm{I}}_{\mathrm{L}}(\mathrm{s})$, $\hat{\mathrm{V}}_{\mathrm{C1}}(\mathrm{s})$, $\hat{\mathrm{V}}_{\mathrm{Cm}}(\mathrm{s})$, and $\hat{\mathrm{D}}_1(\mathrm{s})$ are the small-signals of inductor current, outer capacitor voltage, embedded storage capacitor voltage, and duty cycle of Q_{11}, respectively.

2.3 SYSTEM ANALYSIS

The APDN is a multiple-input multiple-output (MIMO) system with a modular configuration. In order to take full advantage of this modular configuration, this study considers a decentralized control approach for such MIMO system. While the full-state feedback approach uses information of state variables of every interface module to generate a control signal for each interface module [27], the considered decentralized approach controls each interface module by using information of its own interface module. Prior to applying a decentralized control approach, it is necessary to verify whether the considered system can be controlled in such a manner [84]. In this research, applicability of the decentralized approach is checked by using the concept of "*Decentralized Integral Controllability (DIC)* [85]." A plant with *DIC* property can be controlled to be stable by a decentralized controller with integral action in each decentralized control loop [85]. A sufficient condition of a plant having a *DIC* property is [85]

$$\bar{\sigma}\left([\mathbf{G}(\mathbf{0}) - \mathbf{G_d}(\mathbf{0})]\mathbf{G_d^{-1}}(\mathbf{0})\right) < 1 \tag{2.10}$$

where $G(s)$ is the transfer function matrix of the system, $G_d(s)$ is a diagonal matrix whose diagonal elements consists of the diagonal elements of $G(s)$, and $\bar{\sigma}(\boldsymbol{A})$ is the maximum value of the singular value of a matrix $\boldsymbol{A}$.

Considering that the battery resistance varies depending on the battery state of charge [86], (2.10) was evaluated with different battery resistance values. Figure 2.4 shows that (2.10) is satisfied for different values of battery resistance values, where R_b is the resistance value and R_o is the measured nominal resistance value. This result shows

that it is possible to perform voltage or current regulation of an interface module by using a decentralized approach.

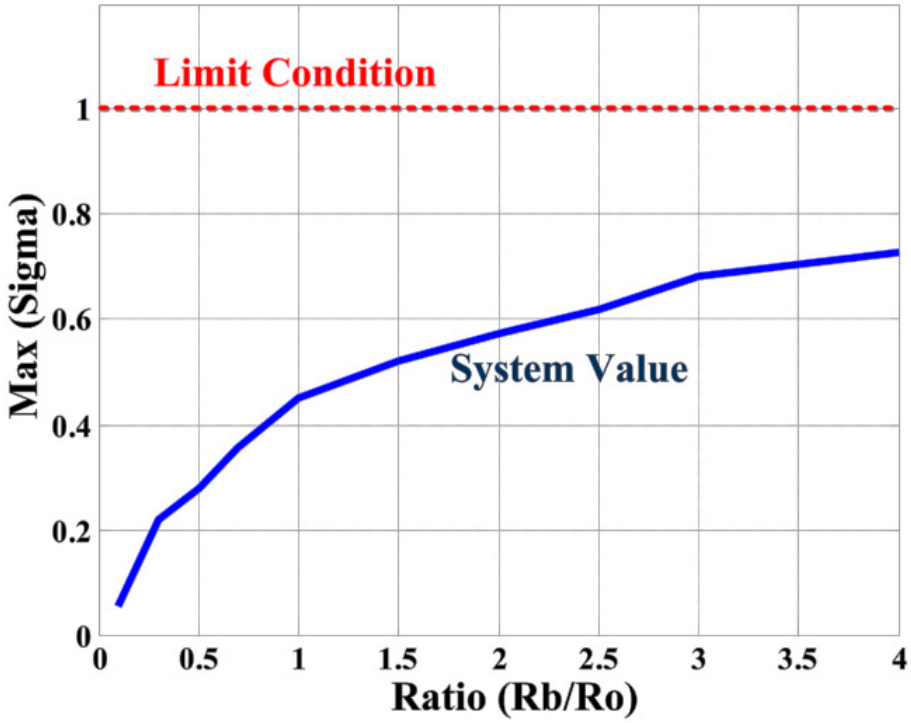

Fig. 2.4. Plot of maximum singular value for checking condition (2.10)

2.4 Operation State and Control

Evidently, the APDN should be operated so that connected loads are powered. Furthermore, the embedded energy storage should also be able to handle the power imbalance between sources and loads at all time scales. The stored energy can be used to handle power mismatches caused by loads with fast dynamics—e.g. pulsed power loads—or sources with slow dynamics—e.g. fuel cells. The energy storage device can also power the load when the source is not available. When there is a power imbalance between sources and loads, either the energy of the embedded storage is discharged to the load or the embedded energy storage is charged with the surplus energy. Hence, the state of charge of the embedded energy storage is critical for operating the APDN as a power buffer. In case the energy storage is fully charged—e.g. a battery is floated—the battery voltage is regulated so the sum of the source power matches the sum of the load power.

Advantages of the APDN can be fully realized by considering not only voltage or current regulation performance of each interface module, but also energy management. Therefore, this research proposes a control approach to perform both variable regulation and energy management of APDNs. The controller has a hierarchical structure with two levels: interface module (lower) level and APDN system (higher) level. While the lower level controller performs variable regulation, the higher level controller generates reference commands for the lower level controller with an objective to ensure that the load is powered and the charge level of the embedded energy storage remains as high as possible. The operation principles of the APDN and details of the considered control approach follows.

2.4.1 Operation States of APDN

The system operation states of an APDN are defined depending on the state-of-charge (SOC) of the embedded energy storage and the difference between available power and required power. As Fig. 2.5 shows, four operations states—e.g. *Charging* state, *Balanced* state, *Discharging* state, and *Degraded* state—are defined. If the input power is higher than the output power and the SOC is lower than its maximum limit, the APDN is in the *Charging* state. At this state, the input interface modules are controlled to power loads and charge the embedded energy storage. The system controller generates the required command value for the interface module controller. The input power flow can be controlled by regulating the current of the input interface module as

$$i_j^* = \frac{(p_{load} + p_{SOC})}{N \cdot V_{in}} \tag{2.11}$$

where p_{SOC} is the output of the battery current controller, p_{load} is the load power, N is the number of interface ports acting as input, and V_{in} is the input voltage of the input interface module. Calculation method for both p_{load} and p_{SOC} is indicated in the next section. In case the input voltage of the interface modules are different, or to designate a different power value for each interface module, the current reference for the j^{th} input interface module can be generated as

$$i_j^* = \frac{K_j(p_{load} + p_{SOC})}{v_j} \tag{2.12}$$

where v_j is the input voltage of the j^{th} input module, and K_j is the power sharing ratio used to distribute the power between different input modules.

Once the embedded energy storage is fully charged—e.g. a battery is floated—the input ports regulate the voltage at the embedded energy storage so the APDN naturally enters the *Balanced* state in which the sum of input power equals the sum of output power. For the APDN of Fig. 2.1, the battery voltage should be regulated at the float voltage to keep the battery fully charged. Therefore, the system controller forces the interface module controller to voltage control mode and regulates the battery voltage at float voltage as

$$v_{bat}^{*} = V_{float} \tag{2.13}$$

where V_{float} is the float voltage of a battery (e.g. 2.25V/cell for valve-regulated lead-acid batteries).

In case the input power cannot supply enough power to the load, the APDN operates either in *Discharging* state or in *Degraded* state. If the SOC level of the embedded energy storage is higher than the pre-defined minimum level (SOC_{min} of Fig. 2.5), the APDN is in *Discharging* state and allows the stored energy to be discharged so that all the load can still be powered. In order to avoid early loss of life for batteries due to cycling and deep discharges, the SOC_{min} value should be higher than the minimum SOC limit value, SOC_{lim}, specified by manufacturers [87]. It should be noted that selection of the SOC_{min} value and the SOC_{lim} value is different. While the SOC_{lim} value is linked to the life-cycle of batteries, the SOC_{min} value is related to system availability. If the SOC level of the embedded energy storage falls below the SOC_{min} value, the system transits to the *Degraded* state. At this state, only critical loads are powered, while the other loads are cut off. Possible examples of critical loads vary depending on the application. For example, in an electric vehicle, the criticality level of electrical devices

for braking and steering functions are higher than that of devices performing functions that simply increase the convenience of passengers [18]. Other examples of load criticality classifications are also reported for naval ships [88]. The *Degraded* state continues until input power exceeds output power and the embedded energy storage transits into the *Charging* state or until the SOC reaches SOC_{lim} when even critical loads are disconnected. Although the necessity of considering the *Degraded* state might vary depending on system requirements (e.g., cost, size, and regulations), this study defined this state as various power systems consider priority based load shedding to ensure that interruptions of loads essential to safety or mission accomplishment are minimized [88].

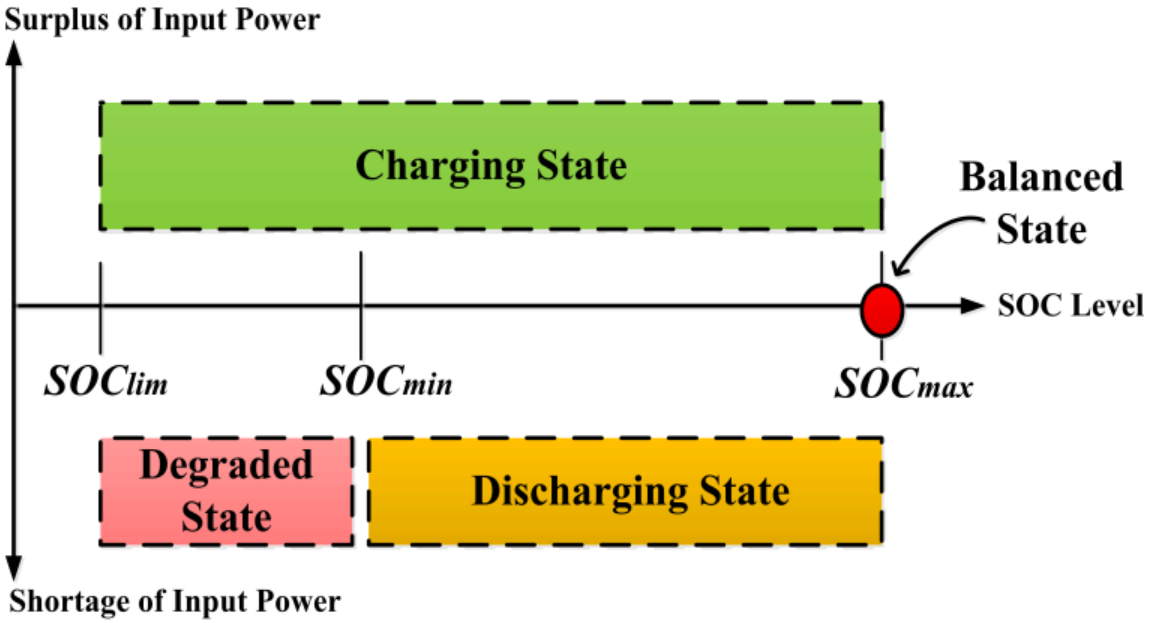

Fig. 2.5. APDN system Operation States

2.4.2 Interface Module Control

As seen in the previous section, the interface modules are required to control either current or voltage depending on the operation state of APDN and the role of each interface module. Figure 2.6 shows a schematic for an interface module controller. The controller switches between voltage mode and current mode depending on the regulation objective of each interface module. The difference between the two modes is how the reference of the current controller is generated. Similar to the approach in [89], the output of the controller is reset whenever a mode transition is made so that a smooth transition between different modes is performed. Details and alternative approaches that ensure a smooth transition between different operation modes are introduced in [57], [89], [90]. Based on the system analysis result of Section 2.3, each interface module is controlled by its own controller using a PI controller as

$$\frac{d\varphi_{1k}}{dt} = i_k^* - i_k \tag{2.14}$$

$$d_k = K_{cp} \cdot (i_k^* - i_k) + K_{ci} \cdot \varphi_{1k} \tag{2.15}$$

$$\frac{d\varphi_{2k}}{dt} = v_k^* - v_k \tag{2.16}$$

$$i_k^* = K_{vp} \cdot (v_k^* - v_k) + K_{vi} \cdot \varphi_{2k} \tag{2.17}$$

where i_k^* is the current reference, i_k is the measured current, d_k is the duty ratio of the interface module k, φ_{1k} is the state of the current controller, v_k^* is the voltage reference, v_k is the measured voltage, φ_{2k} is the state of the voltage controller, and K_{cp}, K_{ci}, K_{vp}, and K_{vi} are the controller gains of the current controller and the voltage controller.

In this study, the controller gains are selected so that the bandwidth of the current loop is set as $1/10^{th}$ of the switching frequency. To ensure that the outer voltage loop and the inner current loop are decoupled from each other, the bandwidth of the voltage loop is set as $1/5^{th}$ of the current control loop. The bandwidths are selected so that different loops are not affected by other control loops and the switching process. The controller gains of each loop are selected so that each control loop is stable by ensuring the specified bandwidth is met, and the loop gains of each control loop have a sufficient phase margin—i.e. larger than 45°. Specific details of calculating the required controller gains that ensure stability for given specification are discussed in [91]-[93]. It should be noted that the proposed control framework can be applied with different controller gains depending on system parameter values and operational needs, such as robustness against system parameter uncertainty.

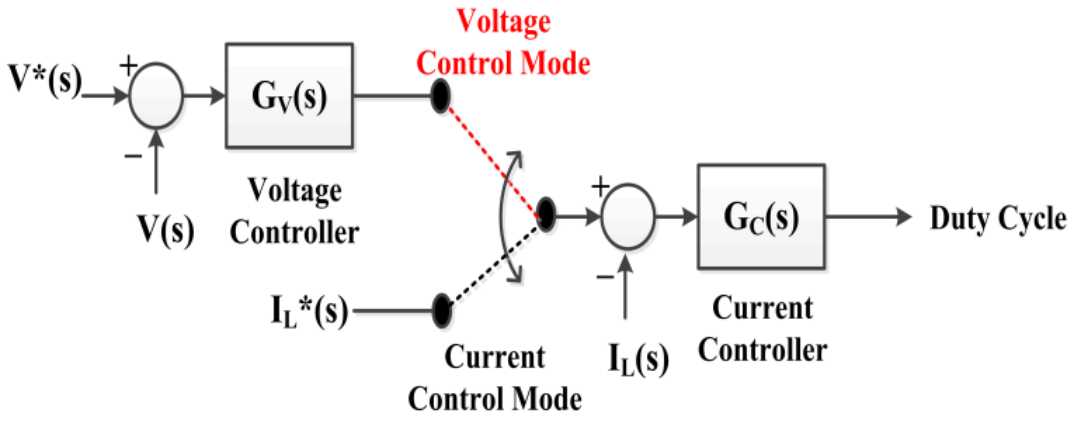

Fig. 2.6. Interface Module Control Diagram

2.4.3 System Level Controller

The overall diagram of the proposed approach structure is shown in Fig. 2.7.

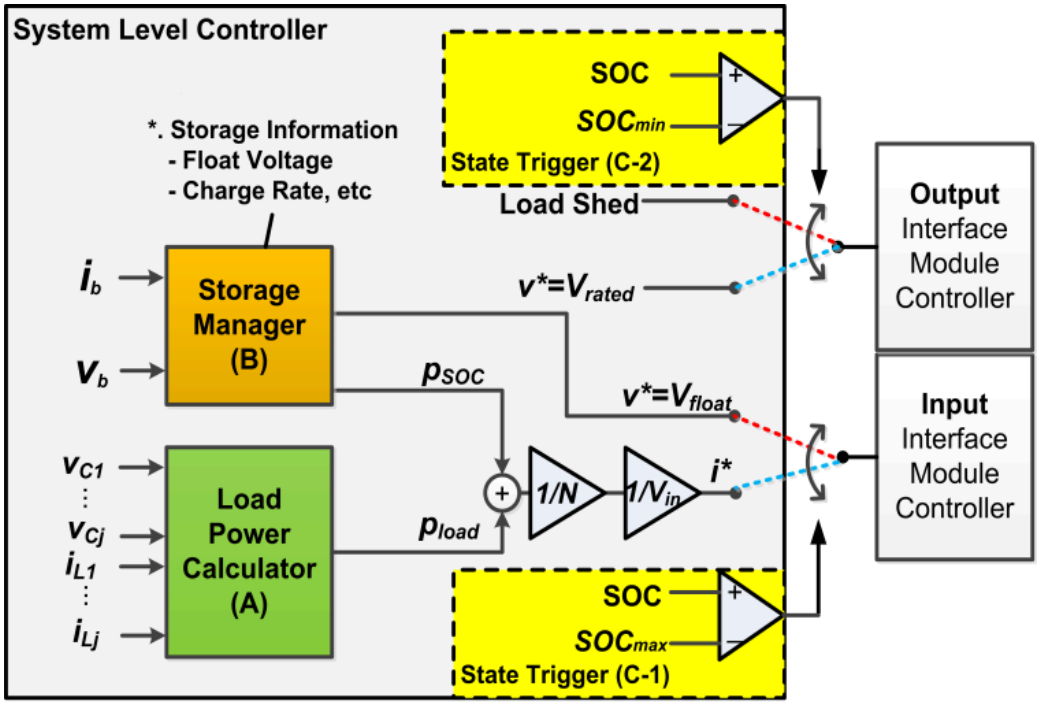

Fig. 2.7. Overall Control Diagram of APDN

The system level controller supervises the interface module controller by generating reference values and ensures the embedded energy storage is charged by monitoring the SOC level. The system level controller consists of the load power calculator, the storage manager and the state trigger. The interface module controllers operate according to the command received from the system level controller. In case a different control approach is considered for state variable regulation of the interface modules, the output of the system controller can be used as a command for such interface module controller. For example, the control law of [27] can be considered to achieve robust regulation performance against input voltage disturbance and parameter uncertainties, such as load resistance value. Explanation on the components of the system level controller follows.

The load power calculator, (A) in Fig. 2.7, calculates the load power by adding the load power (or output power) of each interface module as

$$p_{load} = \sum_{j=1}^{M} p_j = \sum_{j=1}^{M} v_{Cj} \cdot i_{Lj} \tag{2.18}$$

where M is the number of interface ports acting as output, p_j, v_{Cj} and i_{Lj} are the output power, capacitor voltage and inductor current of the j^{th} output interface module.

Similar to power measurement schemes that are commonly used for ac microgrids [94], a first order low pass filter could be applied to (2.18) in order to minimize the effect of ripples in the measured current and voltage as

$$\tau \frac{dp_f}{dt} = -p_f + p_{load} \tag{2.19}$$

where τ is the time constant of the low pass filter, p_{load} is the measured load power value, (2.18), and p_f is the filtered load power value. In case the approach of direct measurement of load power is not desirable, the load power command generated from the power system operator can be used, depending on the availability of load power information of the central power network controller.

The storage manager, (B) in Fig. 2.7, is a battery current controller that regulates the battery current so that the battery is charged according to the pre-defined charge rate specified by the manufacturer. As shown in Fig. 2.8, the output of the storage manager is

$$p_{SOC} = V_b \cdot \left[K_{sp}(I_b^* - i_b) + K_{si} \int \left(I_b^* - i_b(\tau) \right) d\tau \right] \tag{2.20}$$

where K_{sp} and K_{si} are the controller gains of the battery current controller, I_b^* is the battery current reference, i_b is the battery current, and V_b is the terminal voltage of the battery. A limiter is placed at the output of the storage manager to limit abrupt changes during system state transition.

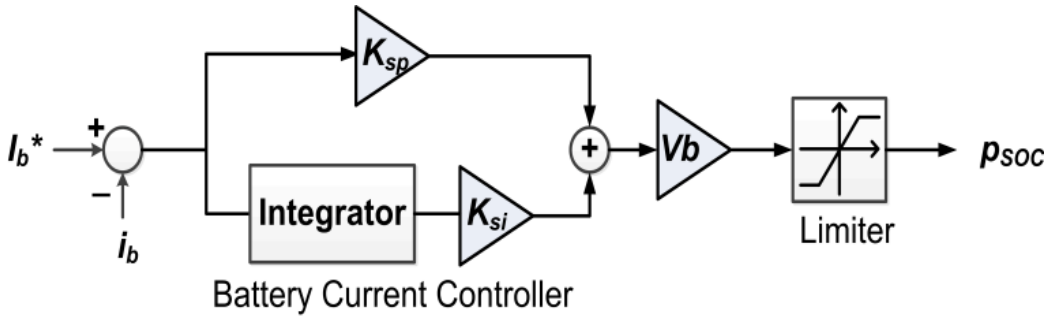

Fig. 2.8. Block Diagram of Storage Manager

The state trigger, (C-1) and (C-2) of Fig. 2.7, generates a signal either to transit the input interface module to voltage mode if the SOC level is SOC_{max} or a load shedding command to cut off non-critical loads if the SOC level is SOC_{min}. For practical issues, a hysteresis band is set around the SOC_{max} and SOC_{min} values to prevent chattering between system states as the SOC level becomes close to SOC_{min} and SOC_{max} [95].

To reduce the complexity caused by implementing a SOC estimation method and since the focus of this study is not on algorithms to determine SOC, this research estimates the SOC level by using a simple approach previously reported in [96] and represented by

$$Q = Q_0 + \frac{1}{C}\int_{t_0}^{t} i_b(\sigma)d\sigma \tag{2.21}$$

where Q is the SOC level, Q_0 is the SOC level at $t=t_0$, ΔQ is the change of SOC level during time period $[t_o, t]$, C is battery capacity, and i_b is the battery current.

The method of (2.21), which is also known as *Ah counting* [97], can be easily implemented in a digital controller by adding the battery current of the present sampling period to the sum of the previous sampling period.

2.4.4 Design Considerations

This section provides a discussion on practical considerations regarding the considered control approach. Based on the fact that the embedded energy storage is directly connected to the interface modules, it is still possible to generate a power reference command for the input modules without the load power information. Since the battery current implicitly depends on the difference between the source power and the load power, the power flow of the APDN can still be managed without acquiring the explicit load power information. Nevertheless, since the acquisition of load power information is independent to the dynamics of the energy storage and the storage manager, the robustness of the APDN performance against load variation can be improved by adding the load power information in the source power command calculation process. Hence, this study uses the load power information as shown in (2.11) and (2.12) so that the performance of the storage management functions—e.g., regulation of battery current—is affected less by sudden load changes compared to the approach that does not utilize the load power information.

Furthermore, the proposed control approach ensures that the charge level of the battery is not affected by losses present in practical circuits. When the battery current is regulated, the input modules are controlled to receive sufficient power from external

power sources to power both the load (including losses) and charge the battery. A change in the power loss would be reflected in the actual battery current level, and the output of the storage manager would show a variation as a response to such change. When the battery voltage is regulated (e.g. when floating the battery), the regulation performed by the input interface modules ensure that the external power sources handle the power loss. This operation characteristic is essential to prevent excessive cycling of the battery, which is used as embedded energy storage in this study.

Considering that the SOC level of a battery determines the operation state of the APDN, acquisition of the SOC level information is essential. Different SOC estimation methods have been proposed by previous studies [97], [98], such as using battery resistance information, measurement of acid density, or implementing a state-estimator. The SOC estimation method used in this study (i.e., *Ah counting*) was chosen because of its simplicity. Although the *Ah counting* method is commonly used [97], the accuracy of the SOC estimation value can be affected by errors in battery current measurement. The measurement error, furthermore, can worsen the estimation performance with a longer integration period as the error accumulates during the integration process. Hence, this study also uses the battery voltage information to reduce the effect that could be caused by using only the battery current based estimation. In case the battery voltage level reaches the float voltage level or the minimum voltage level specified by the manufacturer [57], the state trigger performs the required state transition identical as if the SOC level reached the specified limit values. This ensures that the battery is properly managed even when the estimation based on battery current is not correct. By using the battery voltage information, both overcharging and undercharging the battery could be prevented regardless of the accuracy level of SOC estimation. In case the battery voltage reaches its lower operational limit value, for instance, the battery can be disconnected

based on the measured battery voltage level by using standard equipment, such as a low voltage battery disconnect (LVBD). As the battery voltage level reaches its upper limit value as a result of continuous charging, the battery voltage is regulated at a float level so that the battery is not being damaged by overcharging. Hence, the approach considered in this study avoids potential issues with SOC estimation inaccuracy on the performance of APDN.

2.5 SIMULATION RESULTS

The performance of the interface module controller and the system controller was verified with simulations based on a model implemented using parameters of Table 2.1.

System Parameter	Value (Units)
Input Source	10 V
Capacitance (C_1-C_4)	470 uF
Inductance (L_1-L_4)	320 uH
Embedded Energy Storage	Lead-Acid Battery: 28 V, 5 Ah Capacitor: 1 mF
Battery Resistance	0.33 Ω
Switching Frequency	20 kHz

Table 2.1. System Parameter Values

2.5.1 Interface Module Control

Figure 2.9 shows the simulated regulation performance of the interface module controller. It can be seen that voltage and current responses track both step-up and step-down commands. To verify that the coupling effect between different interface modules can be handled with the proposed interface module control approach, only one of the interface modules is subject to a command change with a 20 ms interval. It can be seen that a change in one interface module does not affect the behavior of other interface modules. This supports the system analysis result showing that the voltage and current of each interface module can be regulated without information from other interface modules.

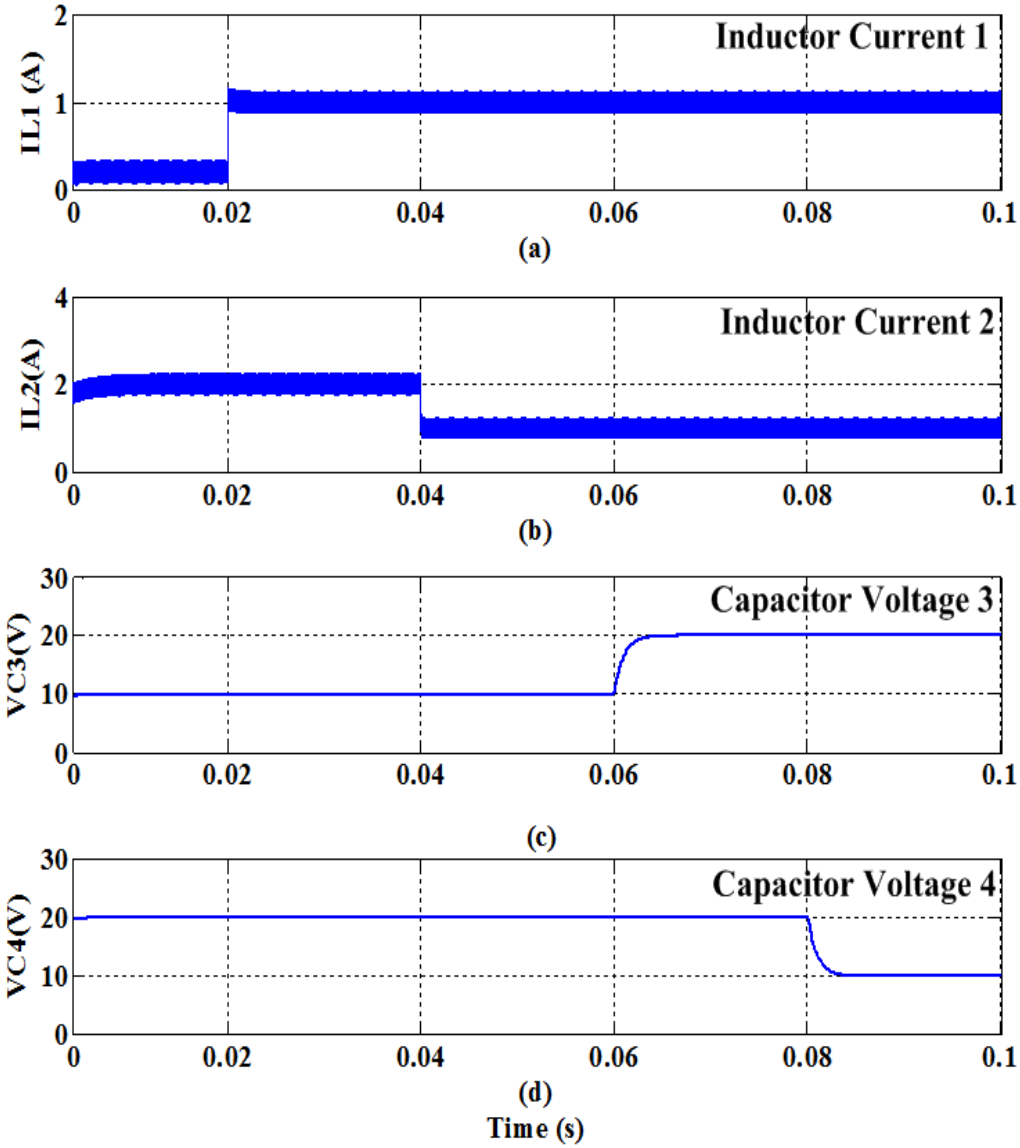

Fig. 2.9. Performance of Interface Module Controller (Simulation)

2.5.2. System Level Control

Figure 2.10 shows the simulation results of the overall system controller. Until *t=0.5 s*, both load and battery receive enough power for loads powering and battery charging. The battery current reference value is set as 3 A. At *t=0.5 s*, both a load power increase and a limit to the source power is applied. As the input power cannot meet the demand, the system transits to *Discharging* state to keep the load powered. This discharge continues until the SOC level decreases to the SOC_{min} value, which is set as 74% as an example in this study. Once the SOC level decreases to this value, part of the load is cut off to maintain the SOC level. As soon as part of the load is shed, the system re-enters *Charging* state. The limit applied to the source power leads to a limited battery charging rate. For example, it can be seen that the battery current during this period is maintained at 1.3A, which is lower than the specified charging current, 3A. Once the limit on the source power is removed at *t=2 s*, the battery is charged at full rate, and the system still operates in *Charging* state. Although the load shedding was activated at 74%, the shed load is recovered back at *t=2.25 s*, which is the instant that the SOC increases back to 76%. It should be noted that the hysteresis band placed around the SOC_{min} value is 2%. Although the load power is increased at *t=3 s*, the charging current is maintained at 3 A by increasing the input power. Figure 2.10 (c) shows the corresponding rise in the SOC level.

Load shedding can also be performed based on operational needs. For example, Fig. 2.11 shows the simulation results of the system controller, and performing load shedding at the instant of *t=0.5s*. While in Fig. 2.10 the load shedding was performed based on the requirements of the battery requirements, in Fig. 2.11 load shedding is performed at *t=0.5 s* due to operational needs. Compared to the waveforms of Fig. 2.10, it can be seen that the battery does not experience discharging, and SOC value continues

to increase. It can be seen that from *t=0.5s* to *t=1.25s*, the input power is lower than the load power in Fig. 2.10, whereas the input power is higher than the load power in Fig. 2.11. This difference results in different operation states of the APDN—i.e. *Discharging* state in Fig. 2.10 and *Charging* state in Fig. 2.11.

It should be noted there is a possibility of transient peaks to be observed in the battery current when a state transition is made from the *Discharging* state to the *Charging* state. Such peak is caused by the output of the storage manager, Fig. 2.8. While the APDN operates in *Discharging* state, the storage manager continuously receives an error signal between the battery current reference and the actual battery current. Once the APDN transits to *Charging* state, the accumulated error during the discharging period is added to the reference. In this study, the peak was mitigated by resetting the output of the storage manager when the system is required to make a state transition. Alternatively, the peaking can be handled by choosing a relatively small limit value for the limiter placed at the output of the storage manager. Still, such current peaks are relatively commonly observed in this same situation—i.e. at the time when the battery starts to charge—in systems using lead-acid batteries.

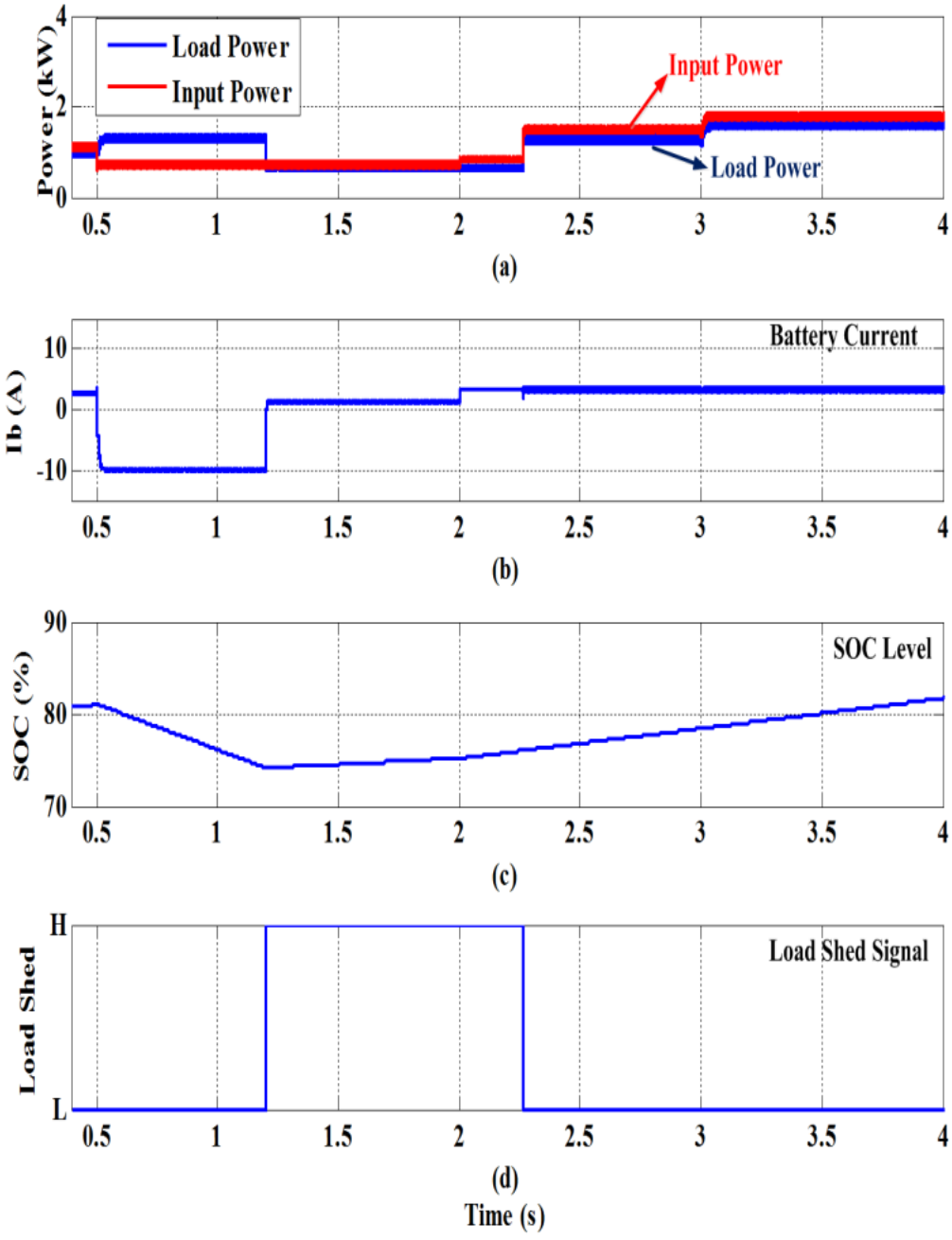

Fig. 2.10. System Controller Simulation: Load shedding based on battery requirements

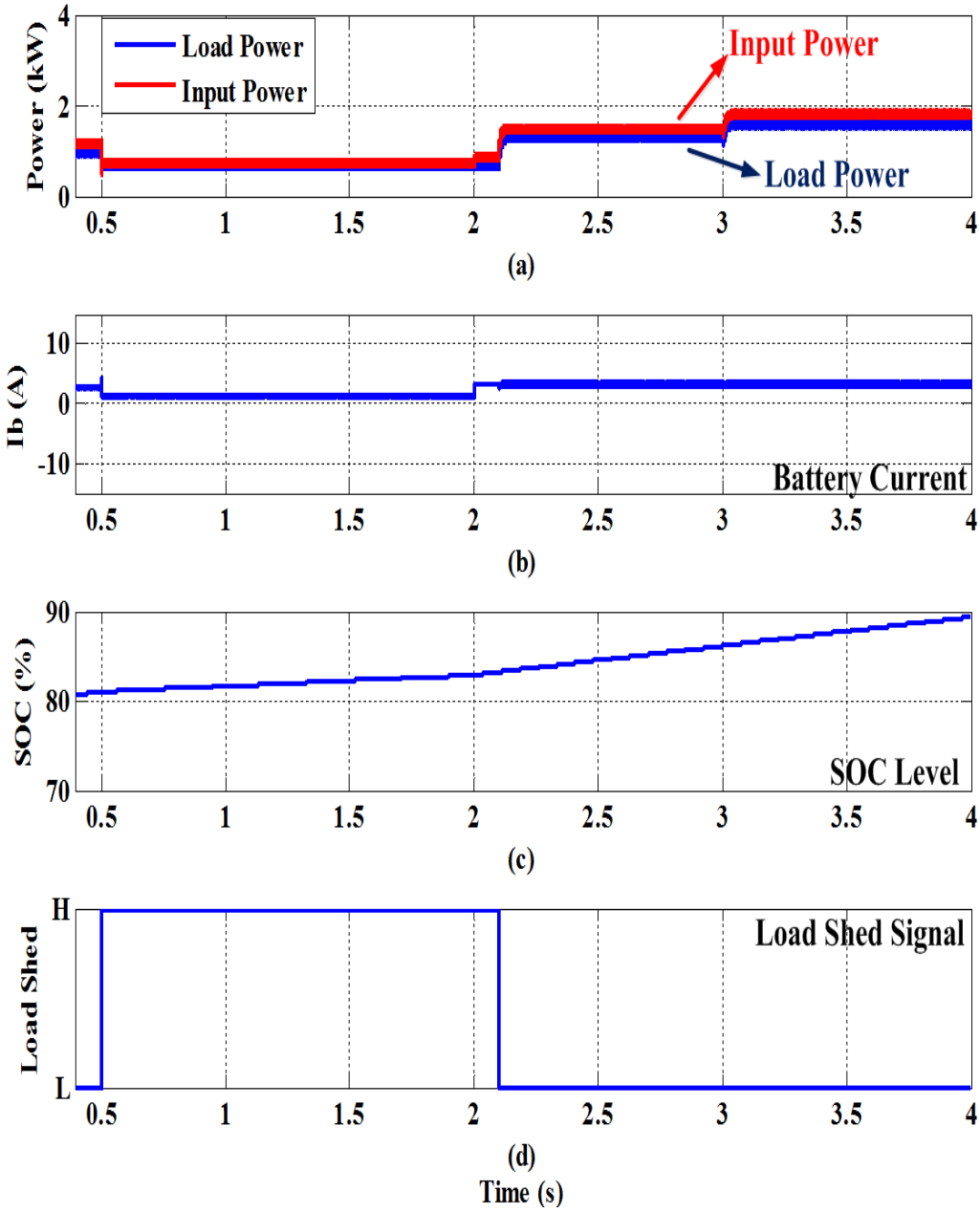

Fig. 2.11. System Controller Simulation: Load shedding based on operational requirements

2.6 Experiment Results

To verify the performance experimentally, a prototype was implemented in hardware. The block diagram of the experiment setup is shown in Fig. 2.12, and the system parameters of Table 2.1 were used. Both system control and interface module control were programmed in a floating point digital controller, TMS320F28335 of Texas Instruments. The interface module controller, the load power calculator, and the storage manager were implemented in a 20 μs interrupt system, while the mode trigger logic operates as a background task for SOC level comparison. The digital controller calculates the reference command for each interface module within the interrupt period by using the feedback information of each interface module—i.e. capacitor voltage and the inductor current.

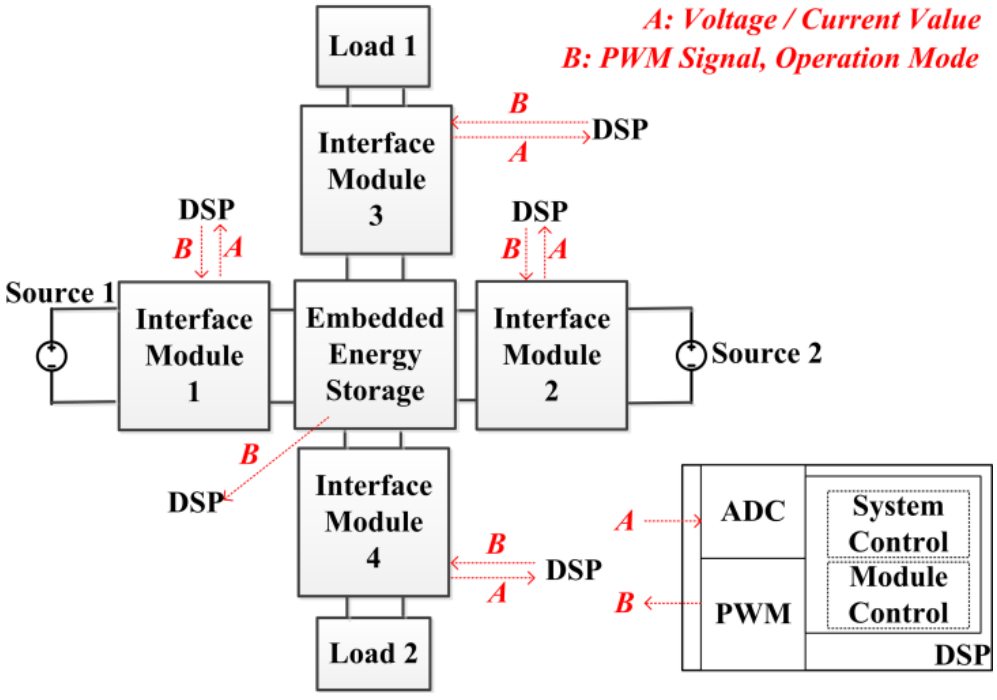

Fig. 2.12. Block Diagram of Experimental Setup

Figure 2.13 shows the regulation performance of the interface module regulator. The input current of the input interface modules responded to a 1 A step command within 1 ms with a slight overshoot. It can also be seen that the output interface module voltage is not affected by the control action of the input controller. This response waveform shows that the state variables of an interface module can be controlled without being affected by the operation of a different interface module. Based on the *DIC* property, which was verified in Section 2.3, the integral controller of each interface module controller enables this response characteristic.

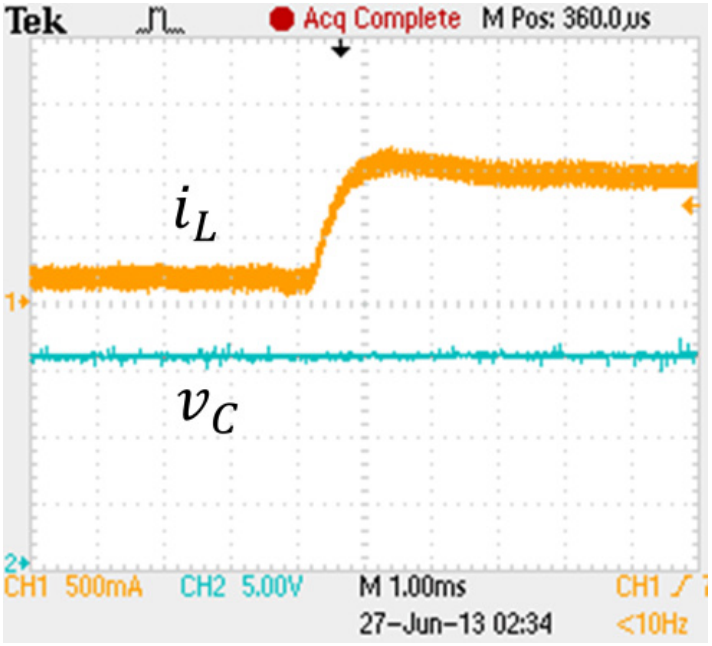

Fig. 2.13. Experimental Waveforms of Interface Module Control

Scope traces in Fig. 2.14 show how the system controller responds to an increase of load power. The system controller forces the APDN to stay in *Charging* state so that battery can still be charged and also power the load. It can be seen that not only the

voltage and current of the interface modules are regulated, but the battery current is also being regulated so that the charging process is not disturbed by the load power variation. Although the battery goes through a short transient discharge, the system controller performs energy management so that sufficient input power is supplied to the APDN. The system controller increased the current reference of the input interface module, from 1 A to 1.5 A, so that the system can handle the load power increase. Although the response characteristics—e.g. overshoot, response time—of the waveform can differ depending on the controller gain values, it can be seen that the proposed control framework can perform both power flow regulation of interface module and battery management.

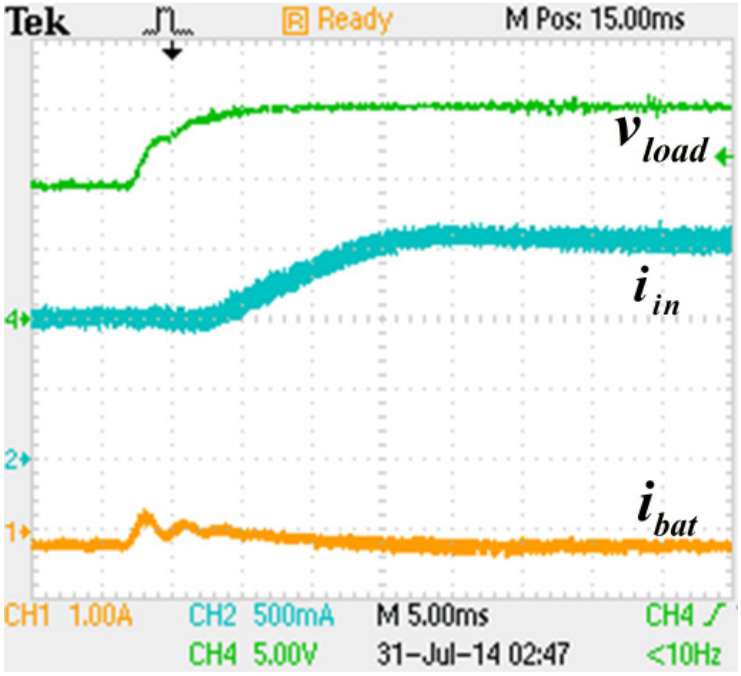

Fig. 2.14. Response Waveforms to a load increase

The experimental waveforms during state transition from the *Discharging* state to the *Charging* state are shown in Fig. 2.15. A limit is applied to the input current reference value to emulate a situation where the load power is larger than the available input power. Although the output of the storage manager keeps increasing to supply power for both load powering and battery charging, the actual inductor current of the input module does not increase but is regulated at a constant value set by the applied limiter. Hence, the APDN is in the *Discharging* state, which causes the SOC value of the battery to continuously decrease. To prevent the SOC value being lower than SOC_{min}, part of the load is shed. In this study, a load shedding logic is implemented so that switches of the output module are forced to turn off. As a result, the output voltage connected to the load decreases to zero as shown in the load voltage waveform of Fig. 2.15. Once the load power is decreased as the result of load shedding, it can be seen that the battery current changes its polarity from positive (discharging) to negative (charging) so that the SOC value can increase.

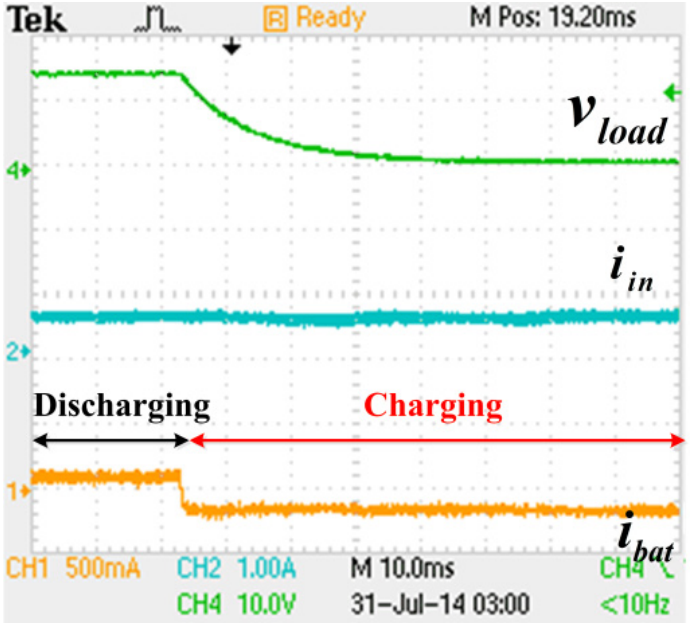

Fig. 2.15. Waveforms during state transition as a response to load shedding

2.7 CONCLUSION

This chapter introduced the configuration, characteristics, and operation states of the APDN. By having bidirectional power flow capability and embedded energy storage, APDNs are able to increase both operational flexibility and availability of power networks. The embedded energy storage can minimize potential power interruptions experienced by the load. To verify the operational use of the embedded energy storage, a two-level hierarchical hybrid controller, lower level for voltage/current regulation and higher level for energy management, was designed to ensure that the loads are powered and also the embedded energy storage charge level is maintained at the highest available level. The considered control approach maximizes the advantages of inherent hardware modularity which contributes to improve availability by reducing the mean downtime when a failure occurs. The details of the considered control approach and related practical design considerations are also discussed. Control performance and energy management capability was verified by both simulations and experiments.

Chapter 3. Decentralized Hierarchical Control of APDNs

3.1 Control and Analysis of a Generalized APDN

3.1.1 Control Requirements

An APDN control should consider both power flow control between interface modules and embedded energy storage management. Although it is possible to implement a centralized control scheme for power flow control, a decentralized control framework that uses only local variables of each interface module eliminate single points of failure and can achieve a more modular system design. Figure 3.1 shows that an APDN will typically be realized with a modular approach, which is preferable for maintenance purposes. In addition, the APDN should also perform management functions for embedded energy storage. For example, most storage should not be exposed to either over-charged or under-charged conditions. The required management functions vary depending on the storage technology. For instance, batteries require charge rate control and a float state for long term storage [96].

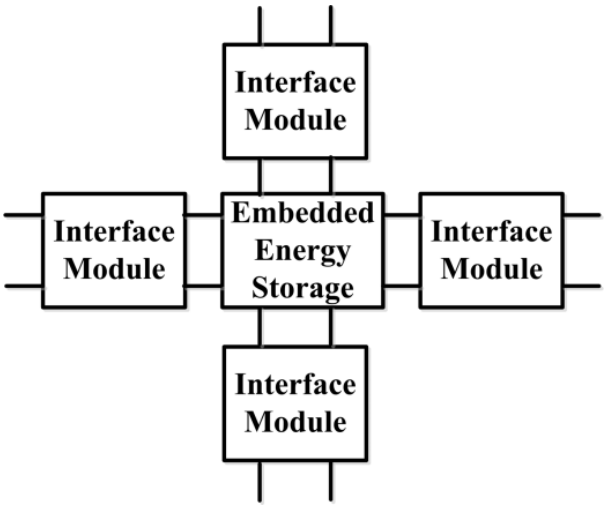

Fig. 3.1. Conceptual block diagram of an APDN

3.1.2 Hierarchical Control Approach

As shown in Fig. 3.2, the main components of the proposed control structure are the primary control loop and the secondary controller [37]. The primary control loop performs power sharing between different input interface modules. Once power sharing is established, an additional control loop is introduced by the secondary controller to regulate either voltage or current of the embedded energy storage. In other words, the secondary controller is mainly dedicated to storage management. Details of each control level are as the following.

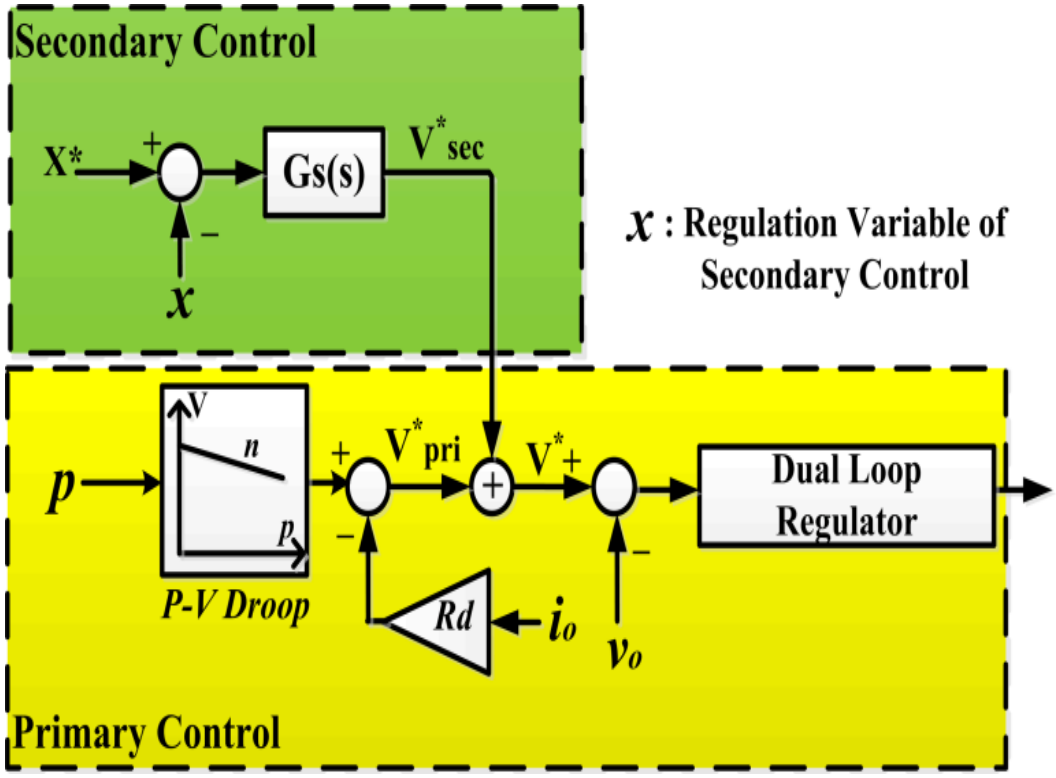

Fig. 3.2. General Block Diagram of Hierarchical control

1) Primary Control

The primary control consists of two components: the droop control law and the dual loop regulator [37]. Droop control, which is a common approach for paralleling multiple power sources [34], is used to perform static load sharing between different interface modules without communication between modules. This control is implemented by making the voltage reference to decrease as the power output increases. In addition to this action, an additional droop could also be added by using a virtual impedance. One reason for the addition of a virtual (resistive) impedance is to achieve stable operation in the presence of constant power loads [13], [99], [100]. It is noting that there is a strong link between power and voltage for resistive networks as it is the likely case of microgrids [9]. This link is analogous to the one observed between power and frequency in conventional, mostly inductive, ac power grids. Hence, such virtual impedance could also increase the effective resistance value so that the considered linear *P-V* droop law could be applied more effectively. A virtual droop resistance can be implemented by subtracting a quantity that is proportional to the output current from the original voltage command. The command value, v_{pri}^{*}, generated from the considered primary control approach is

$$v_{pri}^{*}(t) = E^{*} - n \cdot (p(t) - P^{*}) - R_d i_o(t) \tag{3.1}$$

where E^{*} is the reference voltage, p is the measured power output of the interface module, P^{*} is the reference power, n is the droop gain, R_d is the virtual droop resistance, and i_o is output current of the interface module.

While the droop law generates a voltage reference, the dual loop regulator regulates the power flow according to the voltage reference. The regulator consists of a fast inner current control loop and outer voltage control loop [37].

2) Secondary Control

The secondary control is used to regulate a variable of interest. The regulation variable, *x*, could be selected depending on specific needs. Possible candidates for the regulation variable for the secondary controller are the voltage of the embedded energy storage or the power flow of interface modules. The output of the secondary controller, v_{sec}^{*} , can be written as

$$v_{sec}^{*}(t) = K_{P2}\left(X^{*} - x(t)\right) + K_{I2}\int_{0}^{t}\left(X^{*} - x(\tau)\right)d\tau \tag{3.2}$$

where K_{P2} and K_{I2} are the controller gains of the secondary controller, *x* is the regulation variable of the secondary controller, and X^{*} is the reference of *x*.

3) Overall Control Structure

As shown in Fig. 3.2, the output of the secondary controller is added as a reference value of the primary controller. Therefore, the overall control command that the dual loop regulator receives is the sum of control commands from the primary control and the secondary control.

3.1.3 Performance Analysis using a Generalized Configuration

This section performs performance analysis of the proposed hierarchical control framework for a generally configured APDN. For an initial analytic description of APDN operation, it will be assumed that there are two input modules and one output module. In addition, the dual loop regulator is assumed to be designed fast enough so that the output voltage of each interface module tracks the voltage command perfectly, $V_o=V^*$. For the considered APDN configuration, the feedback signal used for the dual loop regulator (v_o in Fig. 3.2) would be the common dc-link voltage (V_{dc} in Fig. 3.3).

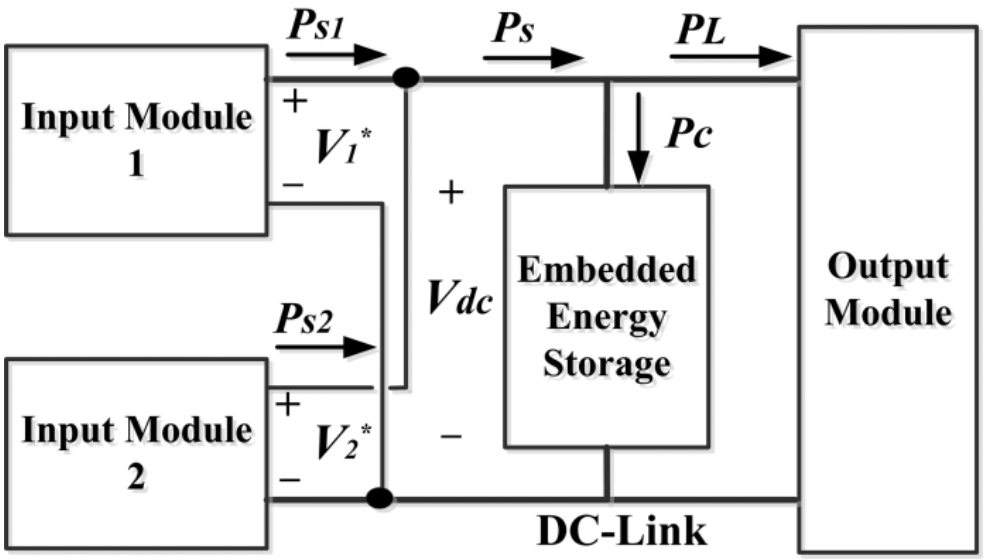

Fig. 3.3. Configuration of a generalized APDN for analysis purposes

If only primary control is applied to both input modules, and using the assumption of a fast dual loop regulator, the configuration represented in Fig. 3.3 leads to

$$V_{dc} = V_1^* = E^* - n_1(P_1 - P_1^*) - R_{d1}I_{o1} \tag{3.3}$$

$$V_{dc} = V_2^* = E^* - n_2(P_2 - P_2^*) - R_{d2}I_{o2} \tag{3.4}$$

where V_{dc} is the dc link voltage, V_1^* and V_2^* are the output of each interface module.

From (3.3) and (3.4), the dc-link voltage can be written as

$$V_{dc} = E^* - \frac{1}{2}\{n_1\Delta P_1 + n_2\Delta P_2 + R_{d1}I_{o1} + R_{d2}I_{o2}\} = E^* - \Delta_{V1} \tag{3.5}$$

where $\Delta P_1 = P_1 - P_1^*$ and $\Delta P_2 = P_2 - P_2^*$ are the differences between the actual and reference power value of each input module.

As shown in (3.5), the common dc-link voltage deviates from the original reference value E^* by an amount of Δ_{V1}. It could be seen that the deviation depends on the virtual droop resistance, and the interface module output power. The secondary controller could be used to remove this deviation by setting the dc-link voltage as the regulation variable of the secondary controller. This secondary controller is written as

$$V_{sec}^*(s) = G_{sec}(s) \cdot \left(E^*(s) - V_{dc}(s)\right) \tag{3.6}$$

where $G_{sec}(s)$ is the transfer function of the secondary controller.

The reference value of each interface module with the secondary controller becomes

$$V_j^*(s) = E^*(s) - n_j P_j(s) + n_j P_j^*(s) - R_{dj}I_{oj}(s) + V_{sec}^*(s) \tag{3.7}$$

where the subscript j represents input module j (j=1,2).

Similar to the process for deriving (3.5), the dc link voltage with secondary control could be represented by

$$V_{dc}(s) = E^*(s) - \Delta_{V2}(s) \tag{3.8}$$

$$\Delta_{V2}(s) = \frac{0.5}{1 + G_{sec}(s)}\{n_1\Delta P_1 + n_2\Delta P_2 + R_{d1}I_{o1} + R_{d2}I_{o2}\} \tag{3.9}$$

It can be seen that the voltage deviation $\Delta_{V2}(s)$ can be minimized by designing the secondary controller to satisfy $|G_{sec}(s)| \gg 1$. This secondary controller restores the dc-link voltage to the reference, E^*. The well-known PI controller in (3.2) could satisfy such objective. Based on this principle, control approaches that use a secondary controller to improve load sharing performance [46] or employ multiple secondary controllers with different regulation variables to enhance both load sharing performance and voltage regulation [47] were proposed for micro-grids.

In this study, the secondary controller is used to regulate current or voltage of the embedded energy storage. It is worth noting, however, that the secondary control might cause energy imbalances issues depending on the configuration of the embedded energy storage and the secondary controller. To illustrate this point, consider a case in which all power input and output of an APDN are regulated with a secondary controller to follow a power reference value, P_j^*, dispatched from a central controller [40]. By setting the interface module power, P_{sj}, as the regulation variable of one of the regulated input/output modules, the secondary controller for this case could be written as

$$v_j^*(t) = K_{Pj}\big(P^* - p_s(t)\big) + K_{Ij}\int_0^t (P^* - p_s(\tau))d\tau \tag{3.10}$$

where v^*_j is the command of the secondary controller, K_{Pj} and K_{Ij} are the controller gains of the secondary controller, P^* is the power reference value, and p_s is the power of an interface module.

Similar to the process of deriving (3.5) and (3.8), the dc-link voltage could be written as

$$V_{dc}(s) = E^*(s) - \Delta_{V3}(s) \tag{3.11}$$

where $G_{sec}\ (s)$ is the transfer function of power controller (9), and
$\Delta_{V3}(s) = \frac{1}{2}\big\{\big(n_1 + G_{sec}(s)\big)\Delta P_1(s) + \big(n_2 + G_{sec}(s)\big)\Delta P_2(s) + R_{d1}I_{o1}(s) + R_{d2}I_{o2}(s)\big\}$.

However, in practice, the dc-link voltage of (3.11) will not reach a steady-state value. This issue can be explained in the following way. According to Fig. 3.3, ideally the total input power should equal the sum of embedded energy storage power and the load power as

$$p_{s1}(t) + p_{s2}(t) = p_C(t) + p_L(t) \tag{3.12}$$

where p_{S1} and p_{S2} are the power output of interface module #1 and #2, p_c is the embedded energy storage power, and p_L is the load power.

In real applications, losses, measurement tolerances and other factors will always make (3.12) to not be verified. As a result, the embedded storage power is either positive or negative. In both cases, the dc-link voltage is not steady [101]. In steady state, this

issue is solved by having the power reference of each module P^* in (3.1) acting as a parametric input to the droop law in Fig. 3.4. As a result, the droop controller will act sharing the differences between the algebraic sum of the total desired dispatched powers P^* and the actual algebraic sum of input or output power of the APDN modules. Still, power imbalances will exist during transients or when the power in all modules is intentionally regulated (e.g. based on (3.10)) so that there is a difference between total power input and power output in the APDN. Such problems originating from power imbalance are addressed by using an embedded energy storage which is capable to handle both short and long-term power differences. Since it is desired to handle long-term power differences and short-term (e.g. transients) power imbalances, in this research, a parallel connection of a battery and an ultra-capacitor is used for embedded energy storage as shown in Fig. 3.4 (a).

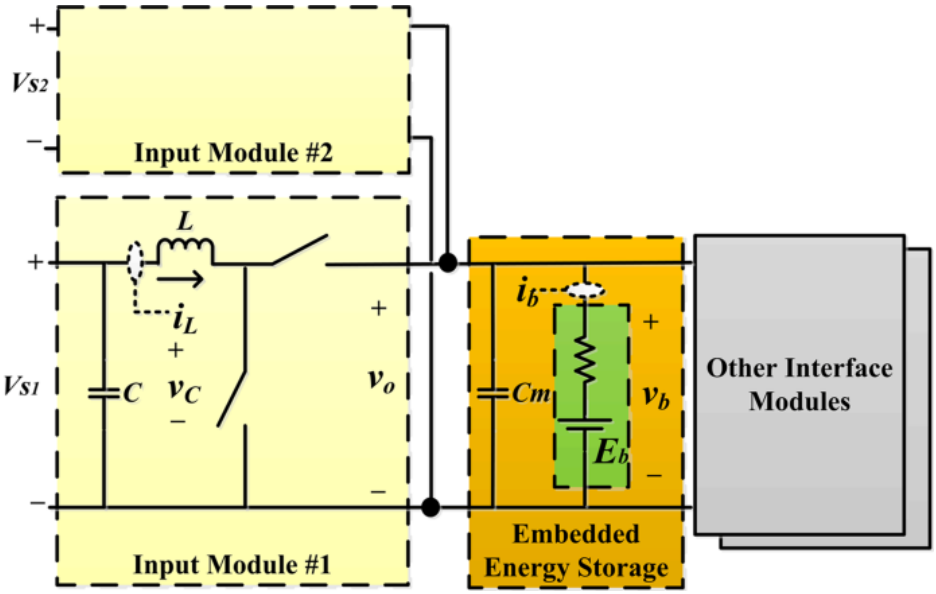

(a) APDN Configuration

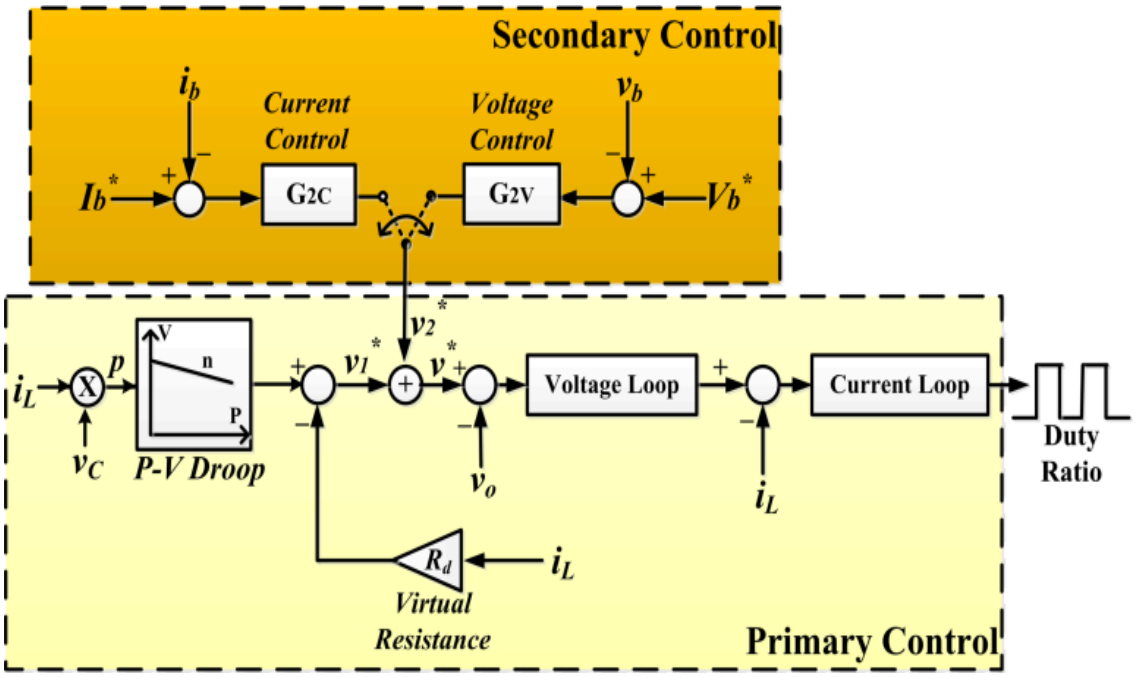

(b) Proposed Control Approach

Fig. 3.4. Proposed configuration and control design for APDN

3.2 PROPOSED HIERARCHICAL CONTROL OF APDN

Based on the previous analysis, this section introduces a hierarchical approach for controlling APDN to satisfy two major objectives: power sharing and energy storage management. In this study, the APDN with a configuration shown in Fig. 3.4 (a) is considered. This APDN uses a bi-directional buck-boost converter for the interface module. This converter operates in boost mode when the interface module operates as an input, and in buck mode as an output. As mentioned in the previous section, the embedded energy storage is a parallel connection of an ultra-capacitor and a battery. This type of hybrid storage is able to handle power balancing without significantly affecting battery life-cycle [102]. In some applications of APDNs, flywheels could be used instead of ultracapacitors. The dc-link voltage is given by the battery voltage value because batteries are directly connected across the dc-link. To perform decentralized power flow control and embedded storage management, this study proposes the hierarchical control approach shown in Fig. 3.4 (b). While the structure of the control law is identical for all interface modules, parameters such as the virtual droop resistance and the droop gain could be set differently. This difference affects the power sharing ratio between the interface modules [34], [47]. The primary control performs load sharing between input interface modules using the droop law in (3.1). In this study, the most inner loop of the dual loop regulator is designed to control the inductor current. The virtual droop resistance is implemented by subtracting a quantity proportional to the inductor current from the original voltage reference value [99]. As the interface module has bi-directional power flow capability, it is possible that an interface module could operate as an output module connected to a constant power load. In such case, the additional droop implemented by the virtual droop resistance could be effectively used to deal with the adverse dynamics of constant power loads [100]. Hence, the virtual droop resistance term

could be commonly used for both input and output modules. In addition to power sharing, the battery current or battery voltage should also be controlled for management purposes [96]. Hence, in this research, a hybrid controller that switches between two different configurations is considered for the secondary controller. The two control laws could be expressed in the form of (3.2) with different regulation variables: either the battery voltage or the battery current. As a result, the proposed overall control law can be written as

$$v^*(t) = v_1^*(t) + v_2^*(t) \tag{3.13}$$

$$v_1^*(t) = E^* - n(p(t) - P^*) - R_d i_L(t) \tag{3.14}$$

$$v_2^*(t) = \begin{cases} K_{P2C}\left(I_b^* - i_b(t)\right) + K_{I2C}\int_0^t \left(I_b^* - i_b(\tau)\right)d\tau \ : Current\ Control \\ K_{P2V}\left(V_b^* - v_b(t)\right) + K_{I2V}\int_0^t \left(V_b^* - v_b(\tau)\right)d\tau \ : Voltage\ Control \end{cases} \tag{3.15}$$

where v^* is the overall control command, v_1^* is the output of primary controller, v_2^* is the output of the secondary controller, K_{P2C} and K_{I2C} are the controller gains of the secondary battery current controller, K_{P2V} and K_{I2V} are the controller gains of the secondary battery voltage controller, i_b and I_b^* are the battery current and its reference, and v_b and V_b^* are the battery voltage and its reference.

3.3 STABILITY ANALYSIS

Similar to dc systems with constant power loads [13], [99], [100], tightly regulated interface modules might affect the stability of the APDN depending on embedded energy storage configuration, control parameter settings, and operation conditions. In this section, system stability is verified by performing a stability analysis to a system with worst case conditions. The considered conditions are:

1) Considering that the negative dynamic impedance of constant power loads is a well known cause for instability of interconnected power electronic systems [13], [99], [100], the output interface modules are assumed to act as constant power loads.
2) As the battery of the proposed embedded energy storage would contribute to mitigate constant-power loads instabilities in the dc-link stage [13], only capacitors are used as the embedded energy storage.
3) It is assumed that only one interface module operates as an input module, while the remaining modules operate as an output module. This condition is based on the fact that the overall input impedance of the output modules seen from the common dc-link stage decreases as the number of output modules increases [103].

The equivalent small-signal circuit of the APDN with the above assumptions is shown in Fig. 3.5. As each output interface module is assumed to act as an instantaneous constant power load, each output interface module is represented as a parallel connection of a resistor and current source. The value of this resistor and current source is known to be a function of the load power [13].

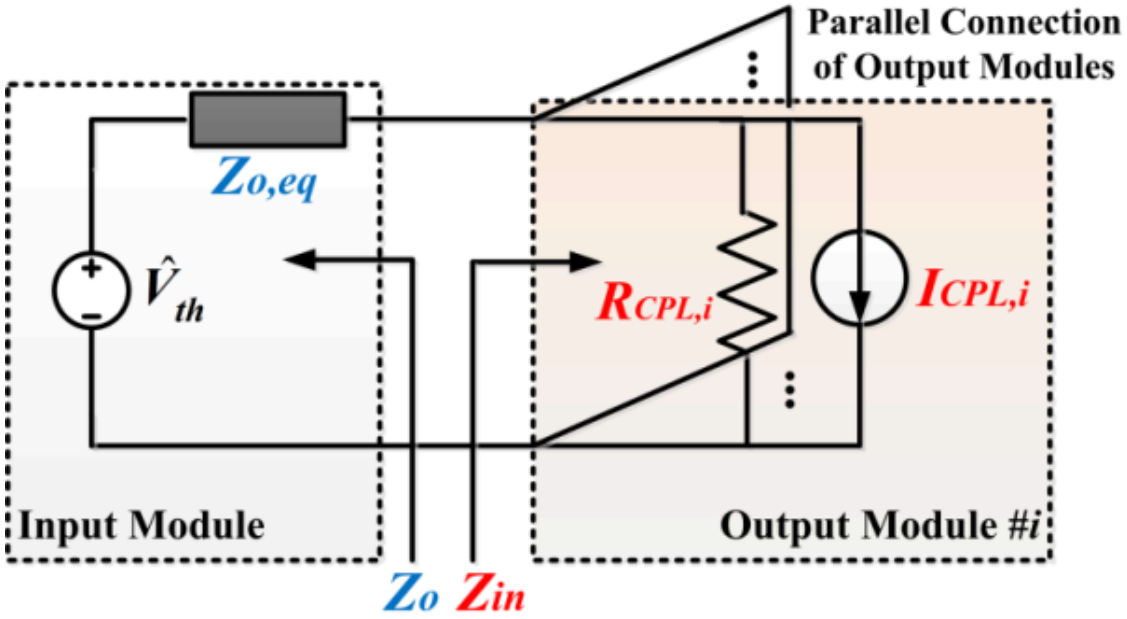

(a) With a Detailed Model of an Output Module

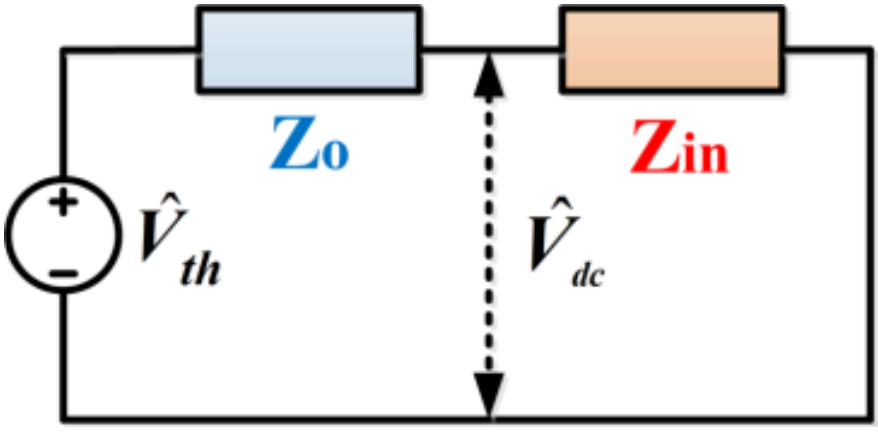

(b) Overall APDN

Fig. 3.5. Equivalent small-signal model of APDN

From Fig. 3.5 (b), the transfer function from $\widehat{V_{th}}(s)$ to $\widehat{V_{dc}}(s)$ can be expressed as

$$\frac{\widehat{V_{dc}}(s)}{\widehat{V_{th}}(s)} = \frac{Z_{in}(s)}{Z_o(s) + Z_{in}(s)} = \frac{1}{1 + [Z_o(s)/Z_{in}(s)]} \tag{3.16}$$

where $Z_o(s)$ is the output impedance of input modules seen from the dc-link, and $Z_{in}(s)$ is the input impedance of output modules seen from the dc-link. As $Z_o(s)/Z_{in}(s)$ is the loop gain of (3.16), (3.16) is stable if $|Z_o(s)| \ll |Z_{in}(s)|$ is satisfied. This condition ensures that the critical point (-1, 0) is not encircled in the Nyquist diagram of the loop gain [104].

The overall input impedance seen from the common dc-link, $Z_{in}(s)$, is a parallel connection of each output interface module as

$$Z_{in}(s) = Z_{in,eq,1}(s)//Z_{in,eq,2}(s)//Z_{in,eq,3}(s) \tag{3.17}$$

$$Z_{in,eq,i}(s) = R_{CPL,i} = -\frac{V_{dc}^2}{P_{CPL,i}} \tag{3.18}$$

where $Z_{in,eq,i}(s)$, $R_{CPL,i}$, and $P_{CPL,i}$ are the input impedance, small-signal resistance, and load power of output interface #*i*, respectively. As there is only one input interface module, the overall output impedance, $Z_o(s)$, is identical to the output impedance of the input interface module, $Z_{o,eq}(s)$.

By assuming that the inner control loop dynamics of the dual loop regulator is sufficiently faster than the outer control loop dynamics of the dual loop regulator—e.g.

the current tracks the reference perfectly—the output impedance of the input module when applying both primary and secondary control can be expressed as

$$Z_{o2}(s) = \frac{1 + R_d G_P(s)}{sC_m\big(1 + R_d G_P(s)\big) + \bar{D} G_P(s) + \bar{D} G_P(s) G_s(s)} \tag{3.19}$$

where R_d is the virtual droop resistance, $G_P(s)$ is the transfer function of the primary level voltage controller, $G_S(s)$ is the transfer function of the secondary controller, C_m is the capacitance value of the embedded energy storage, and $\bar{D} = 1 - D$ with D being the duty cycle at the equilibrium point. Figure 3.6 shows the bode plot of the minimum value of $Z_{in}(s)$ and $Z_o(s)$, using the parameters in Table 3.1. As Fig. 3.6 shows, $|Z_o(s)|$ is smaller than the minimum value of $|Z_{in}(s)|$. Hence, stability of the considered worst case situation is verified.

The output impedance of the input module with only primary control is also shown in Fig. 3.6. If a PI controller is used for the voltage control loop of the dual loop regulator, the output impedance of the input interface module with the primary control only is expressed as

$$Z_{o1}(s) = \frac{\big(R_d k_p + 1\big)s + R_d k_i}{\big(C_m + C_m R_d k_p\big)s^2 + \big(C_m R_d k_i + \bar{D} k_p\big)s + \bar{D} k_i} \tag{3.20}$$

where R_d is the droop resistance, k_p is the gain of the proportional controller, k_i is the gain of the integral controller, and C_m is the capacitor value of the embedded energy storage.

Figure 3.6 shows that the output impedance in the frequency range of interest is resistive only when the primary controller is applied; thus, showing the contribution of the virtual droop resistance in order to damp the effect of the constant-power load.

However, a higher virtual droop resistance results in shifting the output impedance closer to the input impedance. Therefore, the virtual droop resistance value should satisfy the condition

$$R_d < \overline{D} \cdot \left(Z_{in,min} - \delta\right) \tag{3.21}$$

where $Z_{in,min}$ is the minimum value of $Z_{in}(s)$, and δ, which determines the stability margin [104], is a design parameter that should be selected to ensure that $Z_o(s)$ is sufficiently lower than $Z_{in,min}$. Factors that can affect the value of δ include the dc-link capacitance value, and controller gains of the dual loop regulator [103].

As shown in Fig. 3.6, the output impedance effectively decreases when the secondary controller is active. This decrease in output impedance shows that the dc-link voltage response is affected less by the load current changes compared to the case when only primary control is applied.

In this study, the impedance based analysis is performed to address modular operation (i.e., plug-and-play) of interface modules in an effective and simpler manner [105]. Observations on large signal stability characteristics of APDN could be found from previous studies on stability characteristics of microgrids with constant power loads [13], [106]. Such characteristics include existence of different operation regions (i.e., collapse, and limit cycle oscillations), effect of system parameter values, and conditions for stable operation in dc systems [13] and ac systems [106].

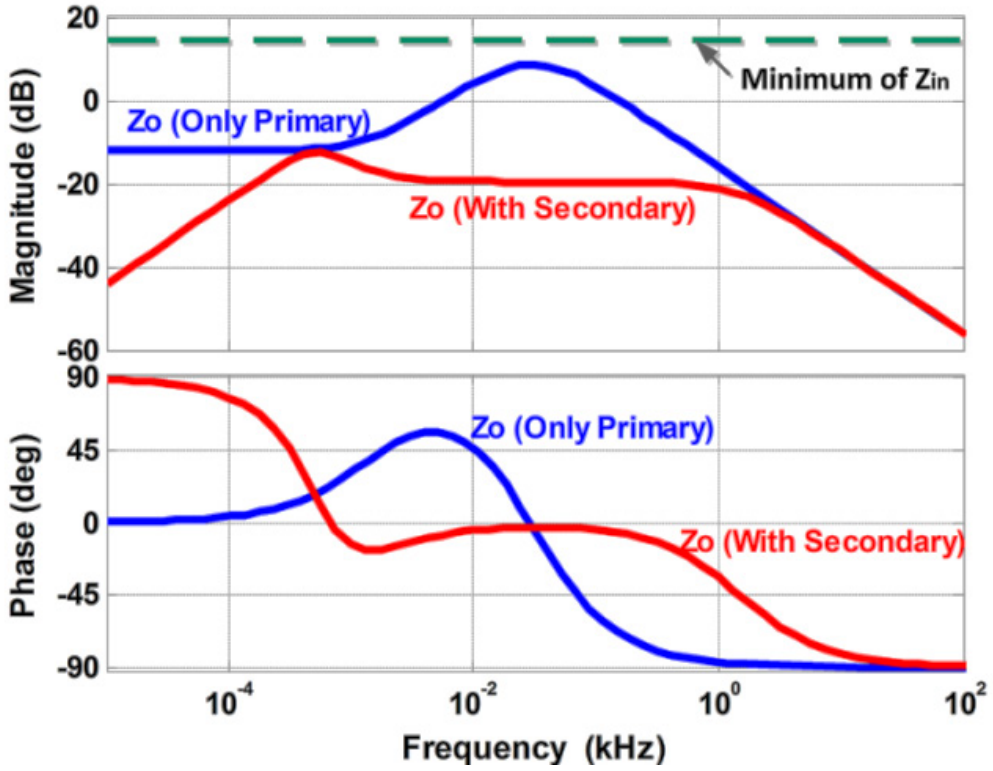

*. Dashed line: Minimum Value of Input Impedance of Output Module

Fig. 3.6. Bode plot of Output impedance of Input interface module

3.4 SIMULATION RESULTS

To verify the operation and performance of the proposed control approach, a simulation was performed using the parameters in Table 3.1. The simulation results are shown in Fig. 3.7. In this simulation, it is assumed that there are two input interface modules.

The APDN should be controlled so that both the load is powered and the battery current is regulated at a constant value, which is assumed to be 0.4 A. Until *t=1s*, only the interface module #1 supplies the power to both power the load and charge the battery. During this period, the battery is regulated to its reference value, 0.4A. As soon as interface module #2 becomes active at *t=1s*, the two interface modules share the power required for both the load and battery charging according to the preset ratio given by the virtual droop resistances. The current of source #1 is 0.6 A, and the current of source #2 is 0.3 A. As in the previous period, the battery current is regulated to the reference value. When the load is increased at *t=2s*, the current of both input modules increased as a response to this load change. It is worth noting that the current sharing ratio between the two interface modules is the same as in the previous period according to the droop law settings. In addition, the battery current is regulated at 0.4 A as in the previous condition. Once the load is reduced back at *t=3s*, the current of both interface modules decrease accordingly. Although one of the power sources—i.e. module #1—is disconnected from the APDN at *t=4s*, the proposed control approach ensures that the remaining input interface module—i.e. module #2—provides enough power for both operating the load and charging the battery at the specified charging rate. Although undershoots and overshoots are observed in the battery current waveforms during the transients, it can be seen that in steady state the battery current is regulated to its reference value, 0.4 A, and that load sharing is performed based on the settings given by the droop law.

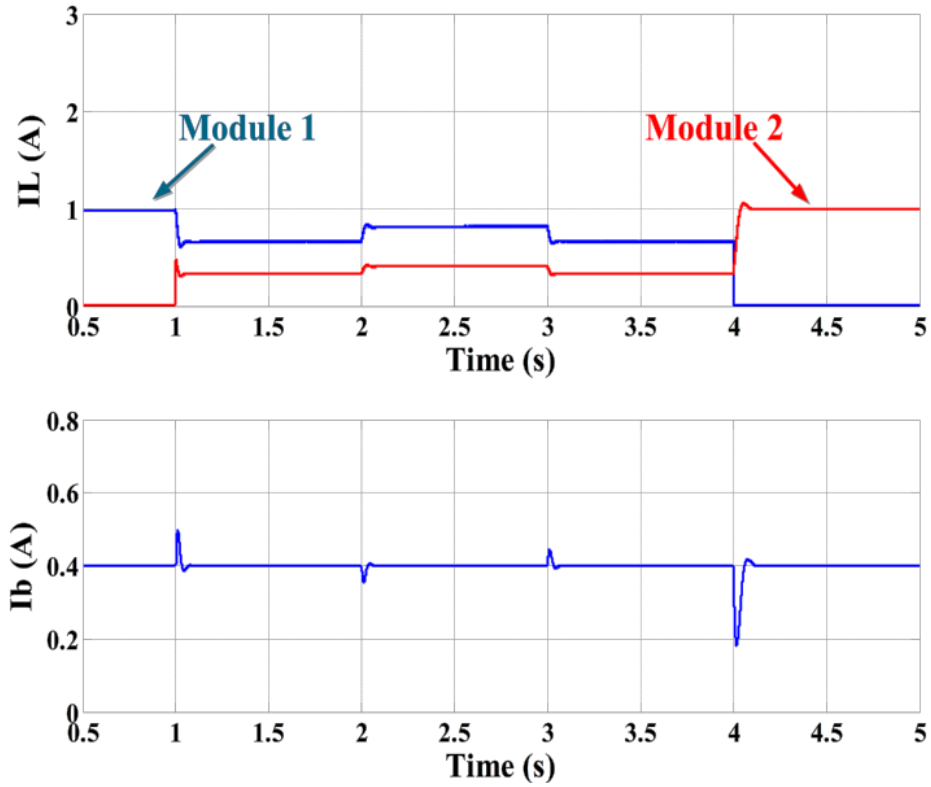

Fig. 3.7. Simulation Waveforms of Inductor Current of Interface Modules (Top) and Battery Current (Bottom)

System Parameter	Value (Units)
Input Source	20 V
Capacitance (C_1-C_4)	470 uF
Inductance (L_1-L_4)	320 uH
Embedded Energy Storage	Lead-Acid Battery: 25 V, 5 Ah Capacitor: 1 mF
Switching Frequency	20 kHz
Virtual Droop Resistance	R_{d1}=0.1 Ω / R_{d2}=0.2 Ω
Droop Gain	n=0.01

Table 3.1. System Parameter Values

3.5 EXPERIMENT RESULTS

The performance of the proposed control approach is verified by an experiment using a hardware prototype. Figure 3.8 shows the block diagram of the experiment setup. In addition to the proposed APDN configuration, two sources and two resistors are connected to a single APDN. SW #1 and SW #2 are used to emulate loss of a power source, while SW #3 is used to introduce load power variation. The control algorithm is implemented on a digital signal processor, TMS320F28335 of Texas Instruments. The system parameters are listed in Table 3.1. A PI controller was used for both primary control and secondary control. Waveforms of the input interface module input currents and the battery current during the experiment process are shown in Fig. 3.9. To verify that the proposed control framework performs both power control and storage management in a decentralized manner, a sequence of various events was performed. Details of the events and operation of the proposed controller can be explained as follows.

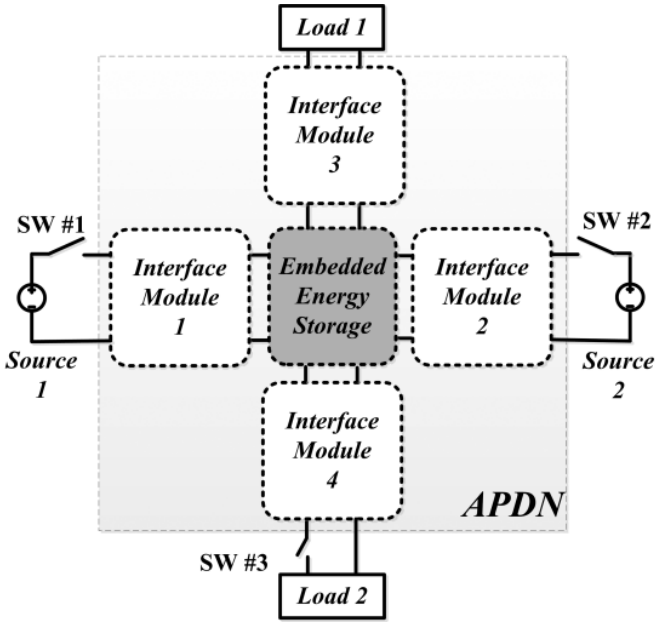

Fig. 3.8. Block Diagram of the experiment setup

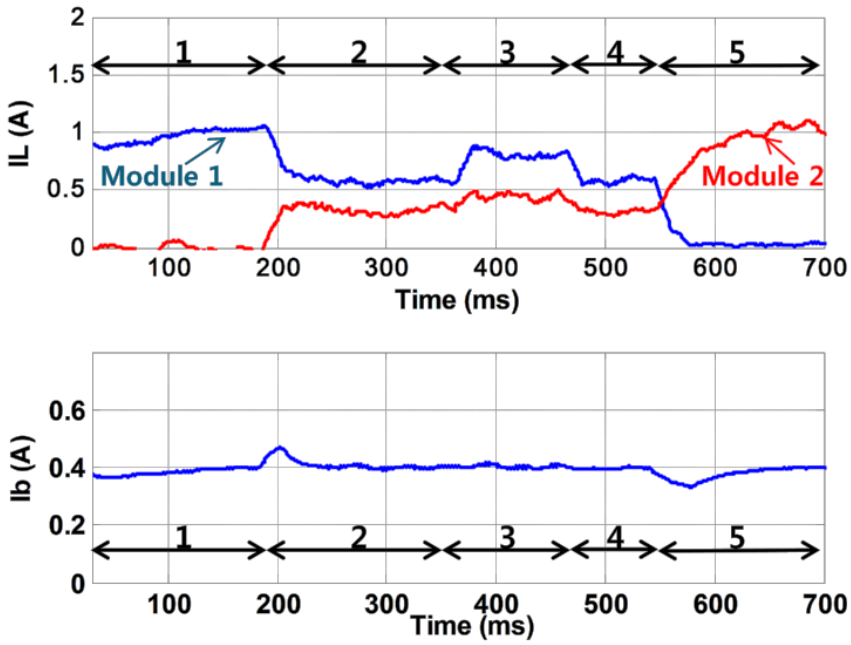

Fig. 3.9. Waveforms of Inductor current (Top) and Battery current (Bottom)

1) Period #1: Initially, only power source #1 and load #1 are connected to the APDN. During this period, the APDN is required to power the load and charge the embedded energy storage at a constant rate. It can be seen that the battery current is regulated to a reference value of 0.4 A. This regulation is performed by the secondary controller of interface module #1.

2) Period #2: At *t=190 ms*, power source #2 is also connected to the APDN by closing SW #2. The current of each interface module is 600 mA and 350 mA. Hence, both sources are supplying power into the dc link. The power sharing ratio between the two sources (1.71:1) approximates the ratio of the virtual resistance values between the input modules listed in Table 3.1, which is 2:1. The mismatch between the two ratios could be explained by losses in a practical circuit [47]. Such issues could be addressed by increasing the slope

of the droop law [46]. In addition, the power sharing ratio depends not only on the virtual resistance value but also on other values, such as the droop gain and power level. It is also worth to note that the output of the secondary controller could also affect the power sharing performance. Similar to [51], placing a limiter at the output of the secondary controller not only could minimize the effect of the secondary controller to the power sharing performance, but also ensures that the output of the interface module or the connected power source does not exceed its maximum ratings. Although, the battery current shows an overshoot during the power-on transient of power source #2, the battery current recovers back to the reference value within 30 ms.

3) Period #3: At *t=370 ms*, the load power is increased by closing SW #3. As a response to this load increase, the current of both input interface modules simultaneously increases to 800 mA and 450 mA. The power sharing ratio between the two sources is 1.77:1. The current increase of both interface modules ensures that the increased load is powered, and also the battery current is regulated to its reference value by the secondary controller.

4) Period #4: At *t=470 ms*, the load power is reduced back to the original value of period #2, by opening SW #3. It can be seen that the inductor current of both input modules decreases back to 600 mA and 350 mA, which is same as in period #2. Although the source power is decreased, the battery current is regulated to its reference value. The secondary controller ensures that battery current regulation is not interrupted by the load power change.

5) Period #5: At *t=550 ms*, power source #1 is disconnected from the APDN by opening SW #1. While the current of interface module #1 decreased to zero, the current of interface module #2 increased to 1 A so that the load is not interrupted and the battery is still being charged with a constant battery current. Although there is a slight undershoot during the turn-off transient, the battery current recovers to its reference value within 70 ms.

The waveforms of each period confirm that the proposed control framework can supply power and perform energy storage management for both single source and multiple source connections. When multiple power sources are available, the power is shared between different sources according to the pre-set droop parameters as shown in period #2, #3, and #4. The waveforms during period #1 and #5 show that the proposed control can both power the load and charge the storage from a single power source.

The interface module current waveforms during the transition from period #4 to #5 show that the proposed control approach can handle sudden loss of power source. Although the power of interface module #1 decreased to zero, the increased power of interface module #2 ensures that the loads are powered and the battery charging process is not interrupted by the sudden power loss of source #1. In addition, the current increase in interface module #2 and the current decrease in interface module #1 during the transition from period #1 to #2, shows that the APDN can perform load sharing between multiple sources as soon as an additional source is connected.

The performance of the storage management capabilities can be verified with Figs. 3.9 and 3.10. The waveforms from period #2 through period #4 of Fig. 3.9 show that the secondary controller regulates the battery current without being interrupted by

load changes. Although the current level of interface modules change depending on the load power level, the battery current is regulated to its reference value during transients.

An additional experiment was performed to verify the performance of battery voltage regulation. Figure 3.10 shows the waveform of the battery voltage and current during the transition of the secondary controller from battery current control mode to battery voltage control mode. The battery voltage is used as the transition condition [57], [96]. It can be observed that the battery voltage is being regulated at 27 V, once the battery voltage based secondary controller is activated at *t=80 ms*. The gradual decrease of battery current confirms the transition to this mode. This control is performed by the secondary controller voltage regulation.

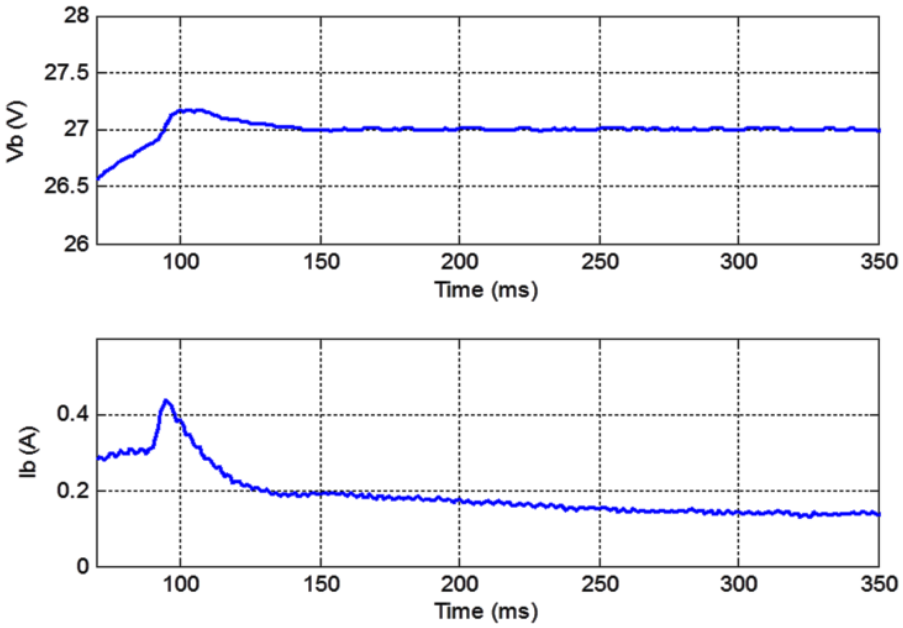

Fig. 3.10. Experimental waveforms of Battery voltage (Top) and Battery current (Bottom)

3.6 CONCLUSIONS

This chapter explored control strategies for APDNs using a decentralized hierarchical control approach. Considering the role of APDNs as a power router inside a microgrid, the control approach has a two-level hierarchy such that the primary level performs load sharing using droop control, and the secondary level performs embedded energy storage management. The effect of considering different regulation variables for the secondary level and embedded energy storage configurations is also studied. Stability is studied by imposing challenging operation conditions on the APDN, and the proposed design is verified by both simulation and an experimental set-up. The key highlights of the control approach are 1) performing both load sharing and embedded energy storage management in a decentralized manner, 2) similar control approach could be considered regardless of the operation mode of the interface module (i.e. input, output), 3) implementing both battery voltage and battery current regulation, and 4) possible to address configuration changes by simple plug-and-play action.

Chapter 4. APDN and System Design

4.1 Features of APDNs as a Connection Interface

The attractive features of using APDN can be discussed by comparing a conventional power system to an APDN-based system as shown in Fig. 4.1. From an availability point of view, APDNs realize more fault tolerant power architectures [4]. While the load of Fig. 4.1 (a) can be powered by the source only through path #1, the same load can be powered by using either *path A* or *B* in Fig. 4.1 (b). It is also possible to use both paths with a controllable power flow in each path. As the power flow can be shared between different paths, the stress that an individual device may experience can be lower compared to single path operation. Furthermore, the load can be powered as long as at least one path is operational. In other words, a fault of one of the paths does not lead to a system failure in an APDN-based system. Active power distribution nodes allow for a simple detection of series faults and for interrupting dc currents because currents are inherently limited. Moreover, circuit protection coordination and selectivity can be easily planned and adjusted in real time. In addition, the embedded energy storage can operate as a back-up source by discharging the energy to the load, which is shown as *Path C* of Fig. 4.1 (b). Since considerable amount of power system failures are caused at the distribution level of power network, APDNs could be placed at major distribution nodes so that the embedded energy storage could reduce the effect of distribution level faults [4], particularly during natural disasters when distribution level faults are the most common source of long power outages. The APDN has a modular configuration, which is favorable for maintenance [28], thus, improving availability by reducing the mean down time. Because of this modular approach, a rectifier/inverter can be easily added in case an ac power distribution circuit is desired. These properties make APDN a possible

candidate as a building block for implementing meshed type power networks, which can have higher availability compared to other system architectures [4].

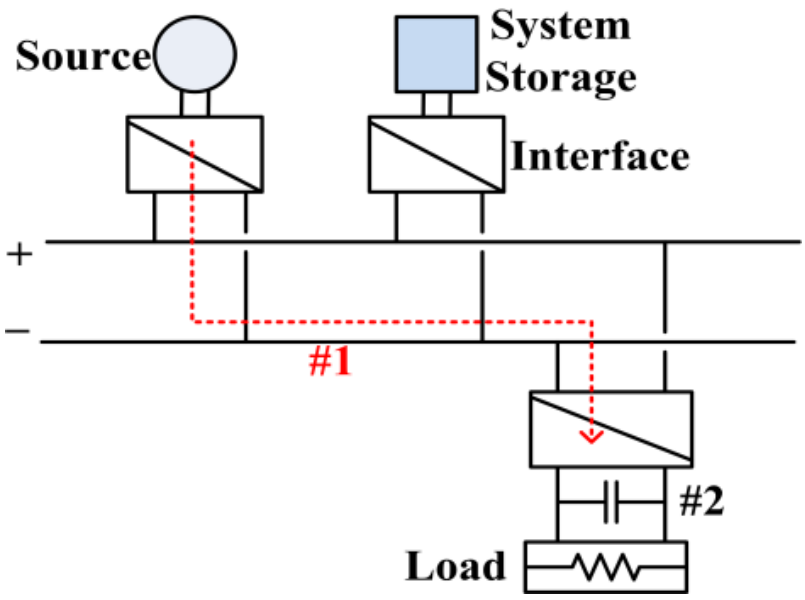

(a): Conventional

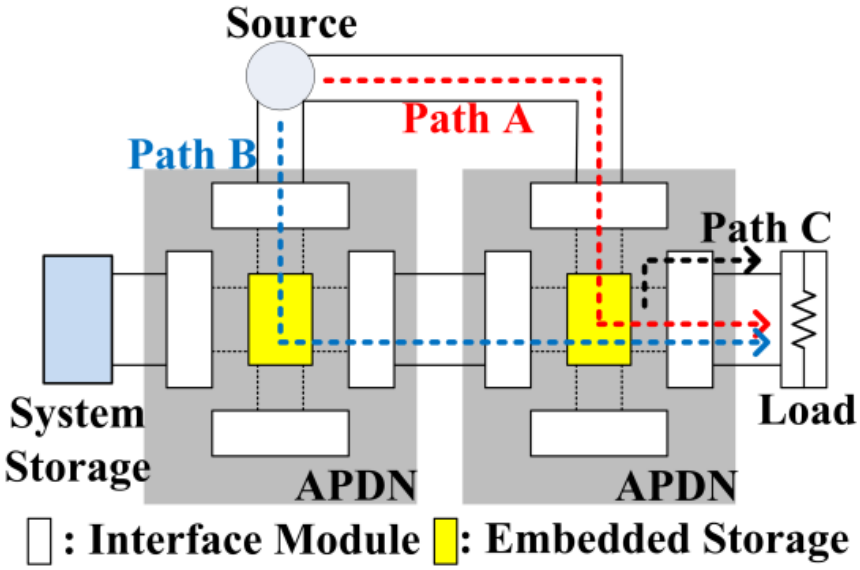

(b) : APDN based

Fig. 4.1. Diagram of a microgrid

From a control perspective, the battery of the embedded energy storage alleviates the burden of operating tightly regulated converter loads—e.g. instantaneous constant power loads. This feature was introduced in [13], which shows that connecting energy storage directly to system buses can be a possible solution for stability issues caused by instantaneous constant power loads. The embedded energy storage can also decouple different dynamic responses among sources and loads, as the embedded energy storage works as a power buffer that handles the power mismatches. System expansion planning can be performed using a modular approach, as the APDN can decouple the dynamics of the original system and the expanded system [8]. Instead of re-designing the power network configuration or developing a new system energy management strategy to ensure overall power balance, the expanded system can be connected to the original system by using APDNs. This feature is favorable for mobile platforms—e.g. aircrafts and ships—as such systems are in need for power network expansion either to replace mechanical systems with electrical systems [18], [107] or to install state-of-art equipment for higher performance, such as radars and display systems [108]. Furthermore, the embedded energy storage ensures that source power and load power is matched even during extreme cases, such as complete loss of external source power. As system stability is closely linked to power balance of the power network, the embedded energy storage of APDNs improve the robustness of the power network against power imbalances by increasing system "inertia" of the network in a distributed manner [8].

4.2 System Availability and Connection Interface

Consider a constrained power system, such as a microgrid. Although for simplicity the discussion mostly focuses on a dc power distribution architecture, the analysis and conclusions can still be applied to ac systems by considering an inverting interface in ac ports. For the purpose of the analysis in this study, the proposed power system is said to be in failed state if the load cannot be powered [28]. Nevertheless, if there are several loads, then the analysis can be applied to each particular load or group of loads connected to the same circuit. Various factors such as system architecture [20], configuration [28], and operation profile of sources and loads [109] could affect the probability that a system is in failed state. In addition, connection and protection devices in the power distribution network can also affect system availability. Representative examples of such connection and protection devices are circuit breakers and fuses. Their function is to minimize the effect of system faults by isolating the fault from rest of the system [110]. It should be noted that, however, system failures can also be caused by these devices. For example, accidental tripping can result in an unnecessary power outage, which affects system availability. Likewise, a circuit breaker or fuse that fails to act during a short circuit may lead to undesirable low voltages that may make loads to fail. Consider also that power electronic interfaces can perform active power flow control and also may be used for implementing system protection [14], [111].

This research considers three types of connection and protection devices, and compares the availability of each approach. As shown in Fig. 4.2, the considered approaches are circuit breakers, power electronic interfaces, and an energy storage integrated power electronic interface. The availability model for each connection interface and the availability comparison results follows.

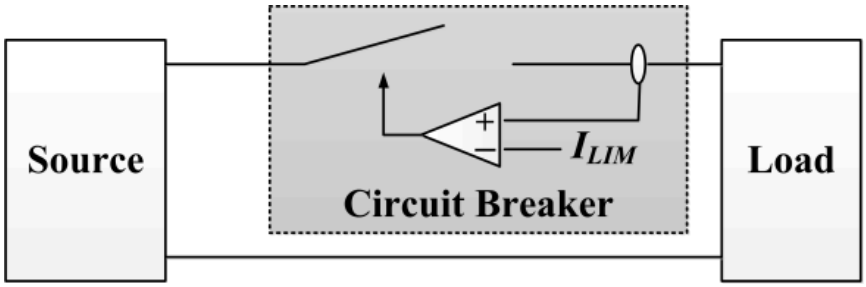

(a) Circuit Breaker

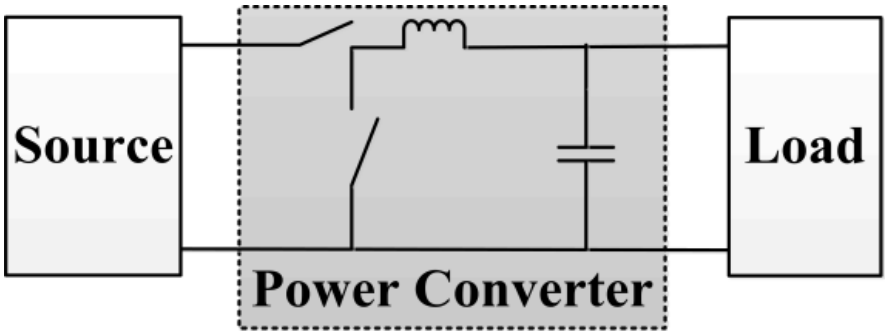

(b)Power Electronic Interface

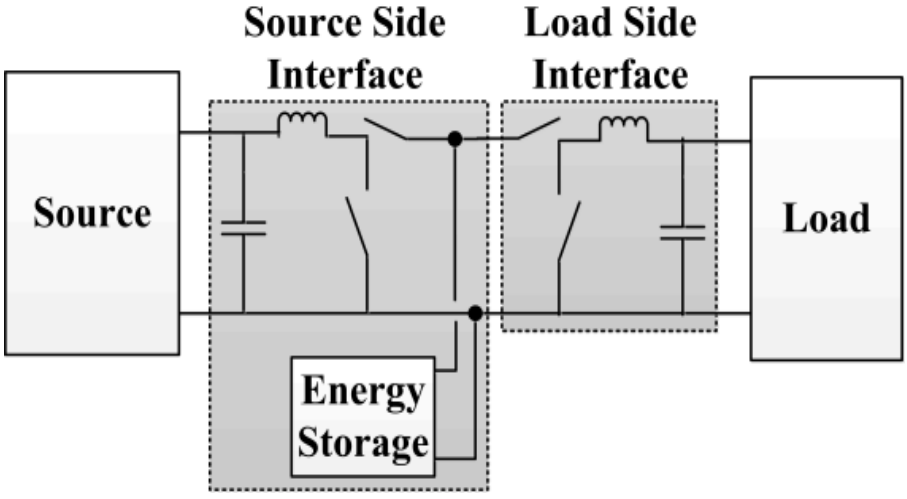

(c) Storage Integrated Power Electronic Interface

Fig. 4.2. Considered connection interface options.

4.2.1 Circuit Breakers

In this study, the circuit breaker is modeled as a series connection of a breaker and a conductor. Therefore, both components should be healthy for the circuit breaker to be in operational state. The breaker represents the internal breaking device or contact that intentionally interrupts the current flow, and the conductor represents the connection mean between the breaking device and the rest of the circuit, which includes an internal connection and any conductor that the circuit breaker is expected to protect. The inclusion of the conductor in this model allows to represent the failure mode in which the circuit breaker fails to open when a fault occurs in the conductor—that is, although the breaking device and a conductor are modeled from an electric perspective as two separate devices connected in series, from an availability modeling perspective, they both form a single integrated system.

A Markov-based availability model for the circuit breaker is shown in Fig. 4.3 (a), originally developed by Krishnamurthy and Kwasinski in [112]. As shown in Fig. 4.3 (a), the circuit breaker model has four states S_{CB}={00,01,10,11}. Each state is represented as a two bit binary number, where each bit corresponds to either operating state (0), or failed state (1). The most significant bit (MSB) represents the state of the conductor connected and protected by the circuit breaker. As both the breaker and the conductor should not be in fail state, only state “00” is the operational state of the circuit breaker. The transitions between these states are governed by the failure and repair rates of the breaker and the conductor. The failure modes that can be explained from Fig. 4.3 (a) are as the following. The transition from state ‘00’ to ‘11’ represents the event when the conductor fails, and also the circuit breaker fails to open. The transition from state ‘00’to ‘10’ represents the event when the conductor fails and the breaker succeeds to open—i.e., this is the typical case of a circuit breaker acting due to a short circuit in the cable it is protecting. Although

the breaker is operational, the overall system made of the circuit breaker and conductor is considered to be in fail state because the load cannot be powered. The transition from '10' to '11' explains the evolved failure mode such that the breaker eventually fails before the fault that led to cable failure is repaired. A transition from '01' to '11' represents, for example, a case when the cable fails after the circuit breaker fails—e.g. a technician damaging the cable after the circuit breaker failed. The availability of the circuit breaker is the probability that the Markov process in Fig. 4.3 (a) is in the state '00.' Hence, the unavailability of the circuit breaker can be calculated as [28]

$$U_{CB} = 1 - A_{CB} = 1 - \pi_{00} \tag{4.1}$$

where A_{CB} is the system availability, and π_{00} is the steady state probability that the system is in the state '00'.

In order to find the steady state probability distribution $\boldsymbol{\pi}$ over the state space S_{CB}, the following system of equations needs to be solved [113]

$$\frac{d\boldsymbol{\pi}^{\boldsymbol{T}}}{dt} = \boldsymbol{\pi}^{\boldsymbol{T}}\boldsymbol{Q} = \mathbf{0} \tag{4.2}$$

where $\boldsymbol{\pi}^{\boldsymbol{T}}$=[π_{00} π_{01} π_{10} π_{11}] is the steady state probability that the system is in a certain state, and $\boldsymbol{Q}$ is the transition probability matrix constructed by using the state transition rates of Fig. 4.3 (a) as

$$\boldsymbol{Q} = \begin{bmatrix} -\lambda_C & 0 & (1-\rho)\lambda_C & \rho\lambda_C \\ \mu_B & -\mu_B-\lambda_C & 0 & \lambda_C \\ \mu_C & 0 & -\mu_C-\lambda_B & \lambda_B \\ 0 & \mu_C & \mu_B & -\mu_C-\mu_B \end{bmatrix} \tag{4.3}$$

where λ_C is the failure rate of the conductor, ρ is the circuit breaker failure to open probability, μ_C is the repair rate of the conductor, λ_B is the failure rate of the breaker, and μ_B is the repair rate of the breaker.

While most of the factors in (4.3) are represented by the failure rate and repair rate of either the breaker or the conductor, the circuit breaker failure to open probability, ρ, is used in order to reflect the fact that circuit breakers may also fail to isolate faults by not opening.

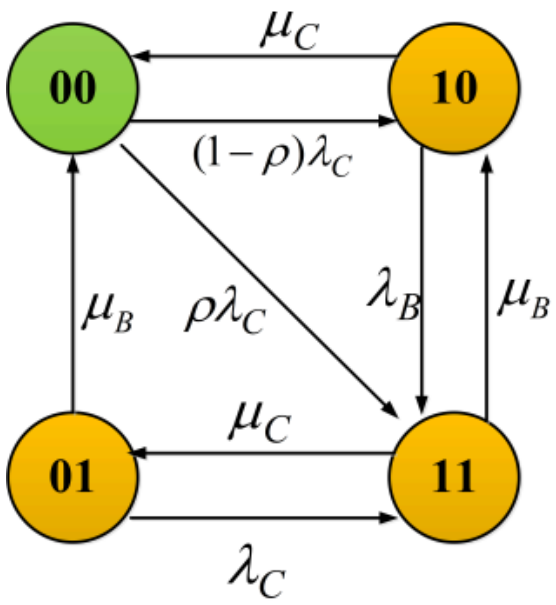

(a) Circuit Breaker

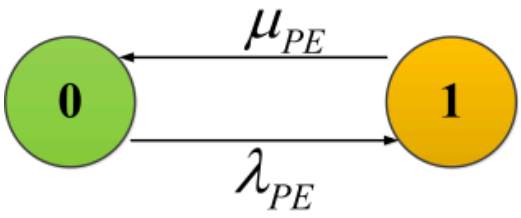

(b) Power Electronic Interface

Fig. 4.3. State transition diagram of connection interfaces

4.2.2 Power Electronic Interface

Considering the increased penetration of power electronic interfaces [4], [22], it is worth considering the use of power converters as a connection interface and for circuit protection. A power electronic interface can provide more flexibility for connecting different types of sources and loads. The state transition diagram for a power electronic interface is shown in Fig. 4.3 (b). In this study, a two state model is considered for a given power electronic interface—i.e. a circuit module. It is assumed that the system is in operational state only if all components of the power electronic interface are healthy. Therefore, the failure rate of the system can be found based on the "parts count" technique by adding the failure rate of each component as

$$\lambda_{PE} = \sum_{i} \lambda_i \tag{4.4}$$

where λ_{PE} is the failure rate of the power electronic interface, and λ_i is the failure rate of the i^{th} component of the power electronic interface.

Similar to the circuit breaker case, unavailability of the configuration in Fig. 4.3 (b) can be calculated as

$$U_{PE,\bar{B}} = 1 - A_{PE,\bar{B}} = 1 - \pi_0 \tag{4.5}$$

where $A_{PE,\bar{B}}$ is the system availability in the absence of a battery—i.e., the ratio between the mean up time and the mean time between failures—and π_0 is the probability that the system is in the operational state '0'. For the considered two state model, the unavailability can be calculated as

$$U_{PE,\bar{B}} = \frac{\lambda_{PE}}{\lambda_{PE} + \mu_{PE}} \tag{4.6}$$

where μ_{PE} and λ_{PE} are the repair rate and failure rate of the system.

4.2.3 Storage Integrated Power Electronic Interface

Energy storage can also be considered for improving availability [20], [28]. As seen in Fig. 4.2 (c), energy storage delays load interruption by discharging the stored energy to the load even when the power transfer path through the power electronic interface on the source side is not available. Although this approach may be considered similar to approaches of installing hold-up capacitors [28], system availability can be improved by considering storage with higher energy density and longer autonomy, such as batteries. The availability of this configuration can be calculated by using the system unavailability of the original system without energy storage, repair rate of the original system, and storage discharge time as [20]

$$A_{PS} = A_{LI}A_{SI} = A_{LI}\left(1 - U_{PE,\bar{B}}e^{-\mu_{PE}T_B}\right) \tag{4.7}$$

where A_{PS} is the availability of the overall system, A_{LI} is the availability of the load side interface, A_{SI} is the availability of the source side interface, $U_{PE,\bar{B}}$ is the unavailability of the source side interface without energy storage, μ_{PE} is the repair rate of the power electronic interface, and T_B is the battery backup time or the storage discharge time, which depends on the source and load profile. In case the battery is directly connected to the load, A_{LI} needs to be made equal to 1 in (4.7). Further details of availability

calculation for a system connected with energy storage, such as the source side interface of Fig. 4.2 (c), are described in [20].

4.2.4 Availability Comparison

The unavailabilities of the considered interface options of Fig. 4.2 (Configuration details shown in Table 4.1) are plotted in Fig. 4.4 using typical failure rate parameters detailed in Table 4.2, and a very conservative mean down time of 166 hours was assumed [63].

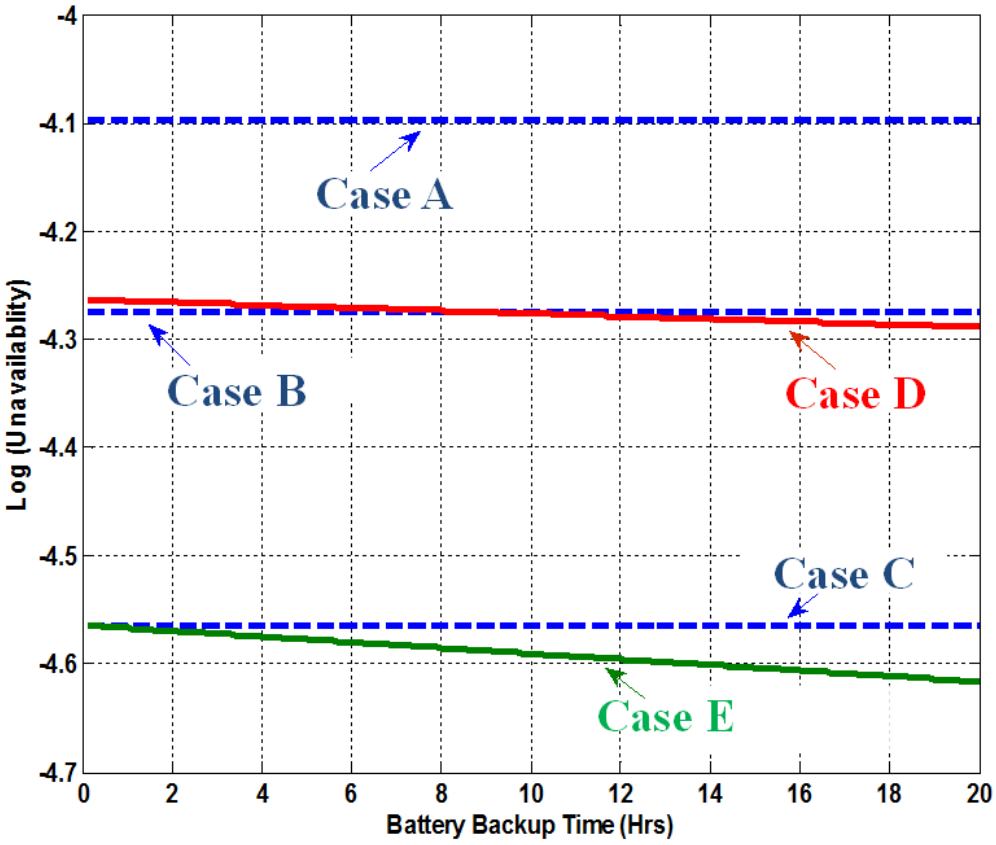

Fig. 4.4. Availability Comparison between different connection interface

Case	Configuration Details	Remarks
A	Circuit Breaker with $\rho=1$	Fig. 4.2(a)
B	Circuit Breaker with $\rho=0$	Fig. 4.2(a)
C	Power Converter	Fig. 4.2(b)
D	Storage Integrated Power Converter	Fig. 4.2(c)
E	Storage Integrated Power Converter with direct load connection	Fig. 4.2(c) without load side interface

Table 4.1. Considered Interface Configurations

Configuration	Component	Failure Rate ($10^{-7}h^{-1}$)	Reference
Circuit Breaker	Breaker and Conductor	3.19	[58]
Power Converter	MOSFET	0.79	[28] based on [58]
	Diode	0.27	
	Capacitor	0.60	
	Inductor	1.13×10^{-3}	[63] based on [58]

Table 4.2. Failure Rate Data

By comparing the results between case A, B and C, unavailability of the power electronic interface is lower than that of the circuit breaker case. Even with the assumption that the circuit breaker never fails to open—i.e. $\rho=0$—Fig. 4.4 shows that in general a power electronic interface has lower unavailability compared to circuit breakers. Evidently, more or less complex circuit topologies may affect this evaluation—e.g. addition of an ac inverting interface may slightly increase the total failure rate—but, similarly, different operational conditions may also affect circuit breaker reliability. For example, it is expected that circuit breakers in dc systems would have a relatively high failure to open probability and circuit breakers may not be able to detect "per-se" series (high-impedance) faults both in ac and dc systems. The plot of the solid lines—i.e. system availability with energy storage—shows that higher availability can be achieved by using a battery with higher backup time. This is evident by comparing the results of case C and case E. Although the same power electronic interface is used for both cases, the energy of the storage device can be used to power the load so system availability can be increased. The effect of the energy storage device on system availability can also be understood by comparing the results between case B and case D. It can be seen that the availability of case D increases as the battery backup time becomes longer, and even becomes higher than that of case B representing an ideal circuit breaker. Hence, lower availability of power electronic interfaces with respect to the presented base line cases—e.g. caused by a higher part count—can be overcome by installing energy storage with longer autonomy whereas lower availability in circuit breakers originated in alternative operational conditions cannot be offset with any simple approach. Motivated by these observations, it is worth considering a storage-integrated power electronic interface as a connection interface to improve availability of a power network.

4.2.5 Cost Analysis

Because cost can be a major decision factor for a trade-off study during the system design process, a simplified cost analysis is also performed for the considered configurations. This analysis is performed by comparing the sum, C_i, of the material cost, $C_{M,i}$, and the downtime cost, $C_{DT,i}$, of the i^{th} configuration of Table 4.1 as

$$C_i = C_{M,i} + C_{DT,i} \tag{4.8}$$

$$C_{M,i} = \begin{cases} \alpha & i = \text{cases A and B} \\ \alpha X & i = \text{Case C} \\ 2\alpha X + \beta & i = \text{Case D} \\ \alpha X + \beta & i = \text{CaseE} \end{cases} \tag{4.9}$$

$$C_{DT,i} = MDT_i \cdot Y \tag{4.10}$$

where α is the circuit breaker cost, X is the ratio of the power electronic cost to the circuit breaker cost, β is the storage cost, Y (\$/hrs) is the unit downtime cost, and MDT is the mean down time. Although a more comprehensive cost analysis can be performed by including additional costs, such as replacement cost, maintenance cost, storage cost and depreciation cost, a simplified cost function (4.8) is used to gain preliminary insights on the benefit of using storage integrated power electronic interfaces as a connection interface for applications that require high level of availability—i.e. applications with high downtime cost.

Figure 4.5 shows the total cost with different configurations. For the case with a low downtime cost (Fig. 4.5 (a)), it is obvious that the system cost of a storage integrated power electronic interface (D) is higher than other cases. This can be explained by the cost of the additional power electronic circuits and the energy storage. This trend,

however, becomes reversed as the downtime cost becomes higher, as shown in Fig. 4.5 (b). It can be seen that the system cost of configuration B becomes comparable to configuration D, and even exceeds the cost of configuration D when a higher downtime cost is considered. This comparison result shows the benefits of installing energy storage as a distributed source for critical loads that are sensitive to availability issues. It should be noted that configuration B represents an ideal circuit breaker (ρ=0), and the cost will be closer to configuration A by considering practical cases. Although the actual value of downtime cost is application dependent, a recent study shows that the average value for a data center is about 474,480 $/hrs [114], which validates the range of downtime cost considered in this study. It should be noted that the results of Fig. 4.5 can differ depending on various factors, such as storage type, manufacturing quantity, and maintenance policy. However, the analysis results show that the burden of higher initial cost of storage integrated power electronic interfaces could be compensated by reducing the downtime costs in applications that require high availability.

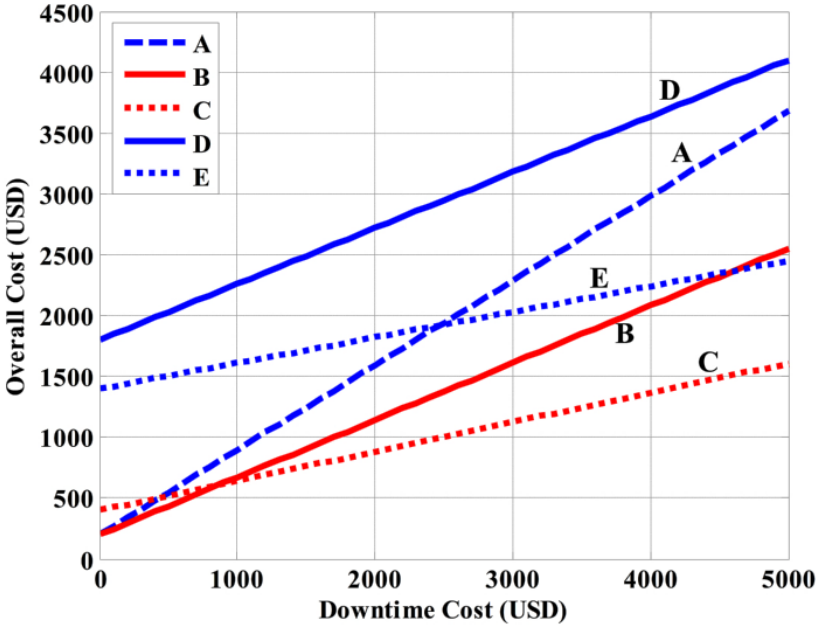

(a) Lower Downtime Costs

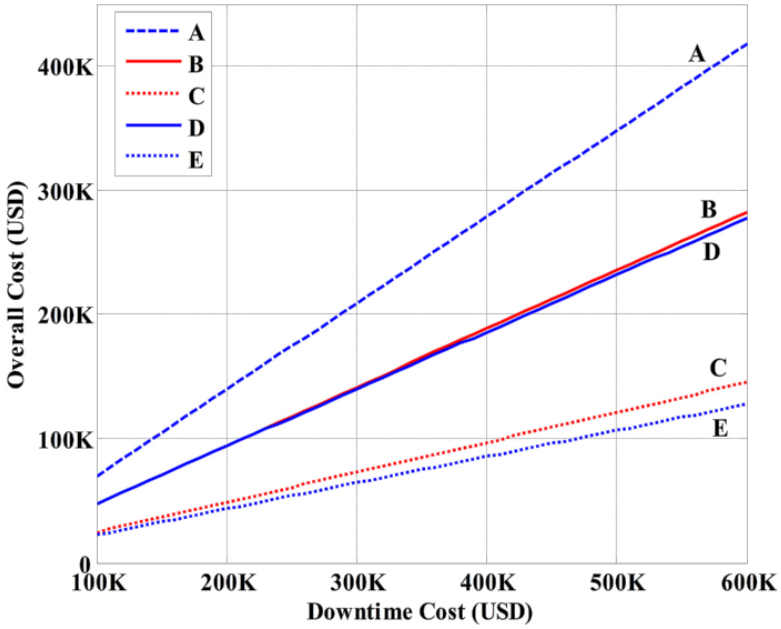

(b) Higher Downtime Costs

Fig. 4.5. Cost Analysis with different downtime costs (α=200, X=2, β=1,000)

4.3 APDN Operation as a Power Buffer

Maintaining power balance between sources and loads is critical to power system stability [9], [14]. Compared to conventional power systems, which have relatively high inertia constants established by directly connected synchronous generators with large rotors, the effect of power imbalance can be more challenging for microgrids. Moreover, loads in power grids are many and relatively very small compared to the generators whereas in microgrids loads are few and with a power that could be comparable to those of the generators. Moreover, considering that sources with different dynamics can be connected to microgrids, it is possible that the source output cannot meet the instantaneous load demand. For example, the output of a renewable generation source can be limited by the weather conditions. A dynamic load profile—e.g. pulsed loads—can also be a cause of power imbalances.

The embedded energy storage of the APDN can act as a power buffer to handle power imbalances [30], [115]. The energy of the APDN can be rapidly discharged to the load so that the performance of the load is not affected by the source dynamics. Since the embedded energy storage device can provide energy to the load, conversely, the source output does not have to be instantly adjusted to handle fast load dynamics. Hence, the energy of the embedded energy storage can be used to mitigate power imbalances issues. Therefore, APDNs can be used to decouple the different dynamics of sources and the loads. Different dynamic responses between loads and sources may be an important issue when adding a load with a behavior that was not considered at the time of designing the microgrid and installing the local power generators. Thus, this research also focuses on using the APDN as a power buffer to perform microgrid design in a modular approach with an open architecture.

4.3.1 Energy Flow Analysis as a Power Buffer

Consider a case wherein the power demand of the load in a microgrid of Fig. 4.6(a) has increased.

It is also assumed that the source has a first order dynamic response, as shown in Fig. 4.7 (a), to a step increase power command as [116]

$$G_s(s) = \frac{P_s(s)}{P_s^*(s)} = \frac{K}{1 + s\tau_s} \tag{4.11}$$

where P_s is the output power of the source, P_s^* is the power reference, and τ_s is the time constant of the source.

If the source is commanded to match the increase of the load power, the energy generated from the source can be written as

$$E_s(t) = P_s(t) \cdot T = P^* \cdot K \cdot \left(1 - e^{-\frac{T}{\tau_s}}\right) \cdot T \tag{4.12}$$

where T is the period length between T_S and T_F, which is the instant the source power matches the load power. Thus, the energy difference during the transient period—i.e., the shaded area in Fig. 4.7 (a)—is

$$E = P^* \cdot T \cdot \left\{(1 - K) - K \cdot e^{-\frac{T}{\tau_s}}\right\} \tag{4.13}$$

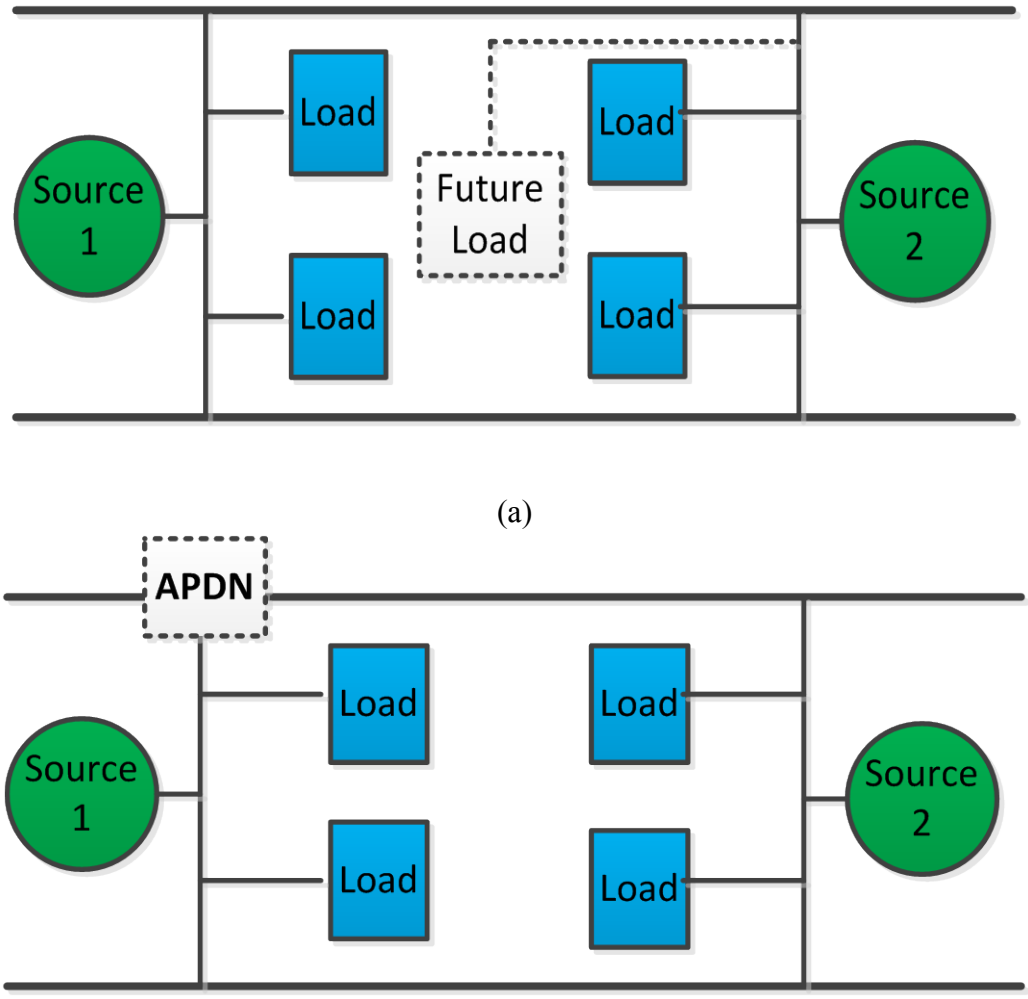

Fig. 4.6. Two possible examples of a microgrid architecture

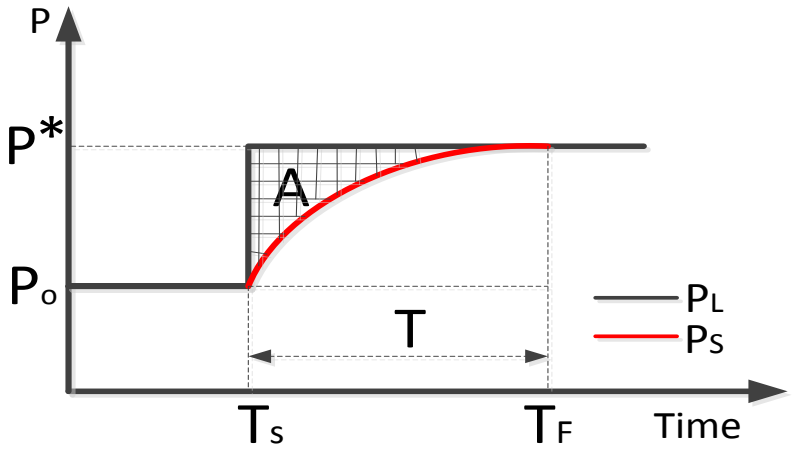

(a)

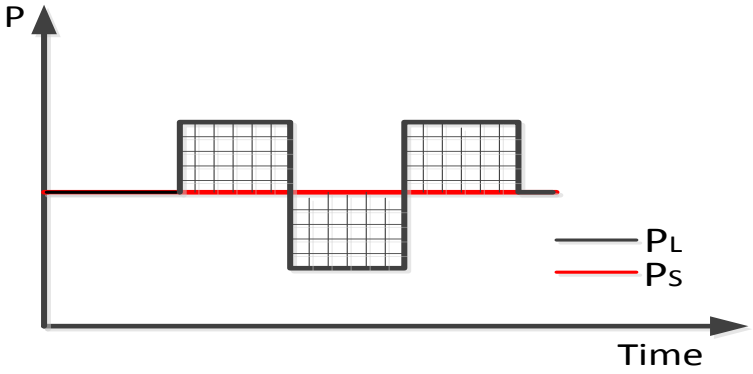

(b)

Fig. 4.7. Example of Source and Load Pattern

In addition to dynamic response mismatches, other possible factors that can affect the amount of power difference between source and load include communication latency [51], and the control bandwidth of power source controllers. Active power distribution nodes can be installed at connection nodes of the power system as shown Fig. 4.6 (b) so

that the local power difference can be handled without the need for rapidly adjusting the output of the sources. The APDN can handle the power imbalance by discharging the energy of (4.13) from the embedded energy storage. Hence, the power imbalance can be handled locally by the APDN. A similar observation can also be made by considering a case when a dynamic load is connected to a power system. For example, the load can have a pulsed pattern as shown in Fig. 4.7 (b). Instead of adjusting the source to meet the rapidly changing load profile, the APDN can be used to handle these dynamics so that the power balance can be ensured while the source operates in an average output profile.

It should be noted that the sizing of the embedded energy storage plays a critical role for enabling this decoupling between sources and loads. Fig. 4.8 shows a plot of required energy that the APDN should supply for different time constants of the source, τ_s, and amplitudes of the step power command, P^*. The APDN can operate as a power buffer as long as the embedded energy storage has the capability to discharge energy to match the power difference. With a first order approximation approach in which discharge rates are considered not to affect a linear relationship between stored energy and discharge time, the period that the storage can work as a power buffer can be calculated as

$$T_s = \frac{E}{P_s - P_L} \tag{4.14}$$

where E is the energy of the embedded energy storage, P_s is the source power, and P_L is the load power.

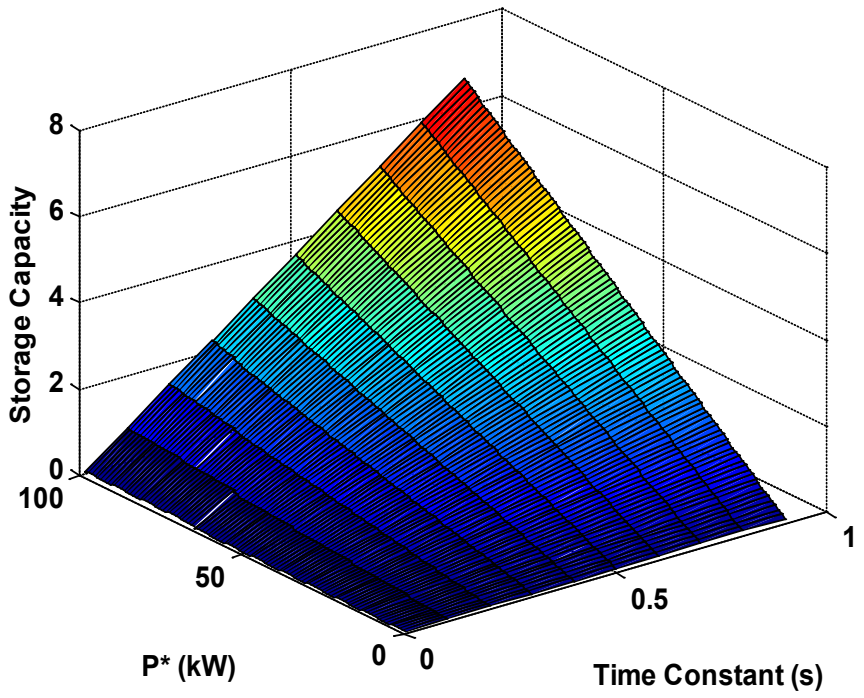

Fig. 4.8. Required Storage Capacity (Assuming K=1, T=4τ)

4.3.2 Backup Power Source

The discussion on operation of the APDN as a power buffer can also be extended for extreme cases, such as complete loss of the source. In this case, the energy of the embedded energy storage is discharged so that the load operation is not affected by the source. The embedded energy storage of the APDN works as a secondary power source that can provide backup power for critical loads.

4.4 System Design Approaches using APDN

This section introduces two cases of using APDNs for microgrid system design. In the first case, the APDN acts as an interface block for performing expansion of microgrids. The second case places the APDN near to critical loads to use the stored energy as a backup power source.

4.4.1 System Expansion

Although a microgrid is initially designed to minimize the effect of different dynamic response among sources and loads, it is not possible to ensure that such imbalance could always be easily addressed, particularly when the microgrid is expanded by adding new loads. As the APDN can work as a power buffer, APDNs allow to effectively handle power imbalance when the microgrid is expanded. For example, if an additional load should be connected to the original microgrid in Fig. 4.6 (a), the additional load can be connected to the microgrid through the APDN, as shown in Fig. 4.9 (a). As will be shown later, the behavior of the new load could affect the stability properties of the original system. However, the conventional approach of having the load directly connected to the existing system bus may be more challenging if the additional load is a constant power load. By using the approaches introduced in past studies—e.g. [13], [41], [42], [74]—it is possible to handle stability problems caused by performing direct connection of future load to the existing microgrid as shown in Fig. 4.6 (a). However, installing additional loads through APDNs with appropriate controls do not require such modifications to the original system. Therefore, the microgrid can be expanded with a modular approach by using the APDN as a building block, and the system can support plug and play operation through the APDN-enabled open architecture.

4.4.2 System Availability Improvement

As introduced in [30], APDNs can be used as an interface block for implementing a meshed network to achieve higher availability compared to conventional radial networks. Single point of failure can be prevented by controlling the power flow of the APDN interface modules [115]. A cost effective approach for increasing availability of critical loads can also be implemented as shown in Fig. 4.9 (b). By placing an APDN next to the critical loads, the operation of such loads may not be interrupted when sources fail because once the external power source is lost, the critical loads can still be powered by the embedded energy storage being discharged. Although this design approach may seem to be similar to simply installing a system level energy storage device, APDNs offer other advantages, such as fault protection by utilizing the current limiting capability of the power electronic interface [4]. In addition, the power flow can be actively controlled, which allows for optimized power flow management.

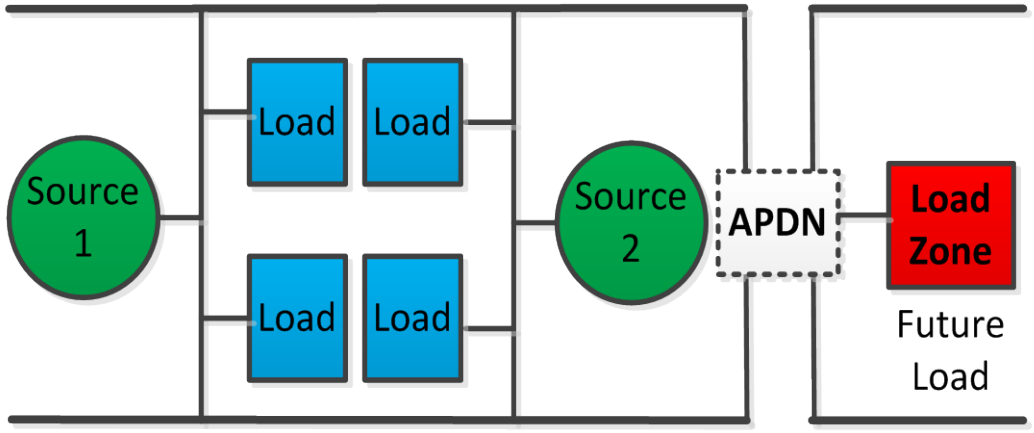

(a). System Expansion

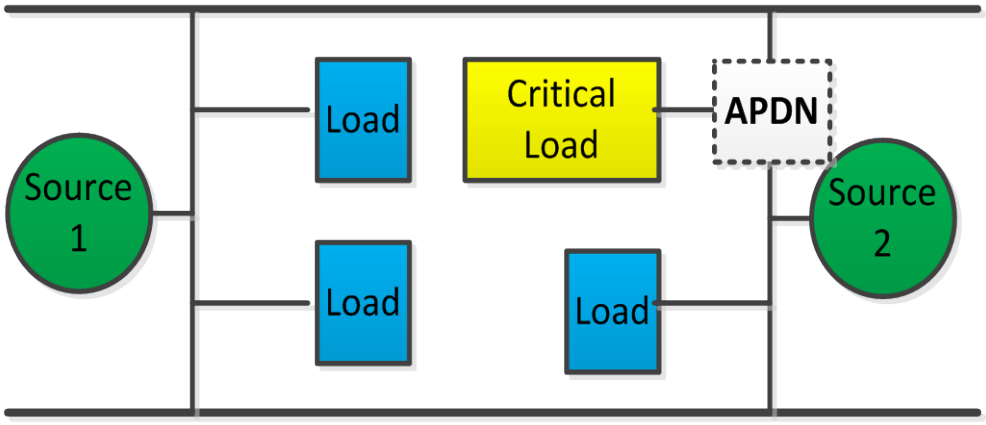

(b). Preventing Loss of Critical Loads

Fig. 4.9. System Design approaches using APDN

4.5 VERIFICATION RESULTS

To verify the performance of the APDN and demonstrate its effectiveness as a power buffer, both simulation and experiments were performed. For simulations, PSIM software was used, and the experiments were performed using an experimental prototype. The control law and feedback of signals were implemented using a digital signal processor, TMS320F28335 of Texas Instruments. FQA44N30 MOSFETs of Fairchild are used for power switches, and the embedded energy storage of the APDN was built by using two lead-acid batteries and a 1 mF capacitor.

4.5.1 Response to Power Imbalance

Figure 4.10 shows the experimental waveform during a discharge process of the embedded energy storage as a response to a sudden source power loss. As soon as the source is lost and the input current drops to 0 A (Fig. 4.10), the battery current shows a polarity reversal showing that the battery starts to discharge. Because of this discharge process, the operation of the load is not interrupted by the loss of the source.

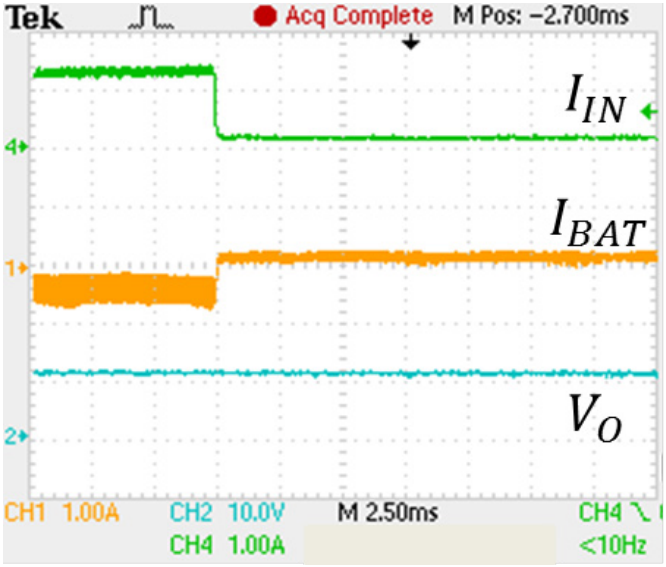

Fig. 4.10. Response to a Sudden Power Loss

4.5.2 Effectiveness of APDN for System Expansion

To verify the effectiveness of using APDNs for enabling modular expansion of microgrids, a simulation was performed assuming a hypothetical expansion of a microgrid. It was assumed to connect a constant power load with an operation profile represented in Fig. 4.12 (a) to a pre-operating microgrid that has a configuration given in Fig. 4.6 (a). The information of the microgrid is provided in Table 4.3. To demonstrate the effectiveness of using APDNs for system expansion, two approaches for connecting a new load to the existing microgrid is considered: 1) connecting the new load directly to the original system (Fig. 4.6 (a)), and 2) connecting the load through the APDN (Fig. 4.9 (a)). The simulated waveforms of the system bus voltage after connecting the new load are shown in Fig. 4.11.

With the first approach—i.e. direct connection to the system bus—the bus voltage experiences oscillations caused by the new load as shown in Fig. 4.11 (a). Furthermore, the oscillations increase as the power of the constant power load increases. The peak-to-peak amplitude of the oscillation is approximately 15 V for a 250 V bus system. If the load is connected through the APDN, it can be seen that the bus voltage does not show such characteristic, as shown in Fig. 4.11 (b). Compared to Fig. 4.11 (a), the system bus voltage is not affected by the increased power level of the new load.

It should be noted that even with the approach of Fig. 4.6 (a), it is still possible to handle the connection of future loads by approaches introduced in [13]. For example, the waveform of the bus voltage after modifying the original system is shown in Fig. 4.12 (b). It can be seen that the oscillations are well damped compared to the original waveform of Fig. 4.11 (a). For this improvement, the virtual resistance value of the source converter controller was increased by 0.2 Ω, and the output capacitance value of the source converter was increased from 1 mF to 3 mF. It is also worth noting that

identification of these remedial strategies may not be straightforward or easily implementable for microgrids with a complex structure or if the number of dynamic loads increases. Compared to experiencing possible difficulties by expanding a microgrid through direct connection, the APDN enables a simplified approach for system expansion and, thus, enables an open architecture.

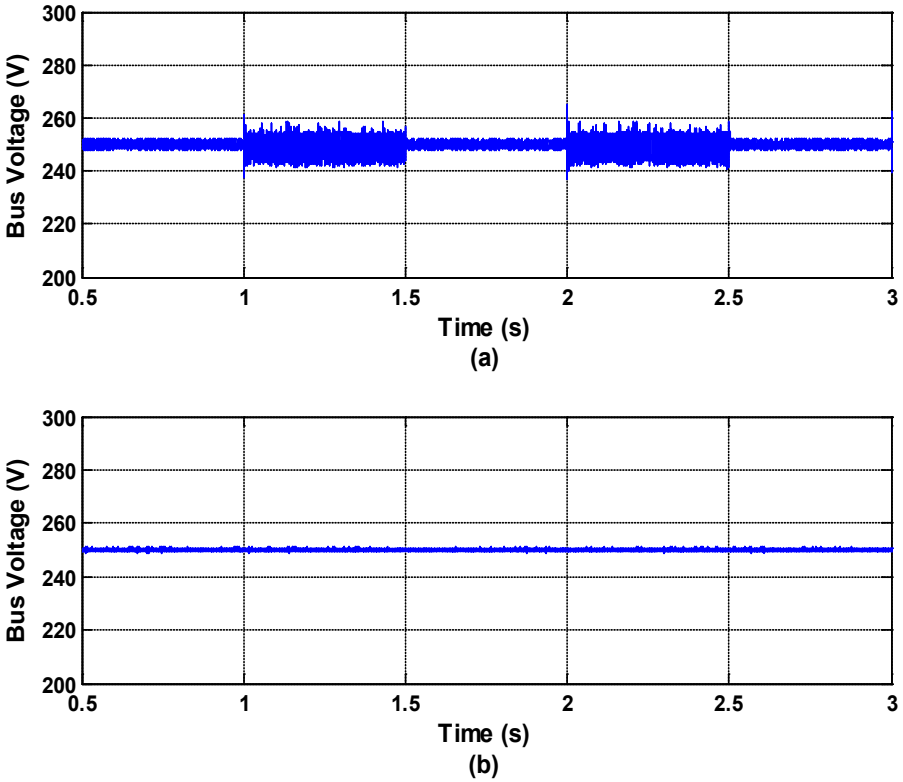

Fig. 4.11. Bus Voltage after system expansion – (a): Direct connection to the main bus (Fig. 4.6 (a)), (b): Connection through the APDN (Fig. 4.9 (a))

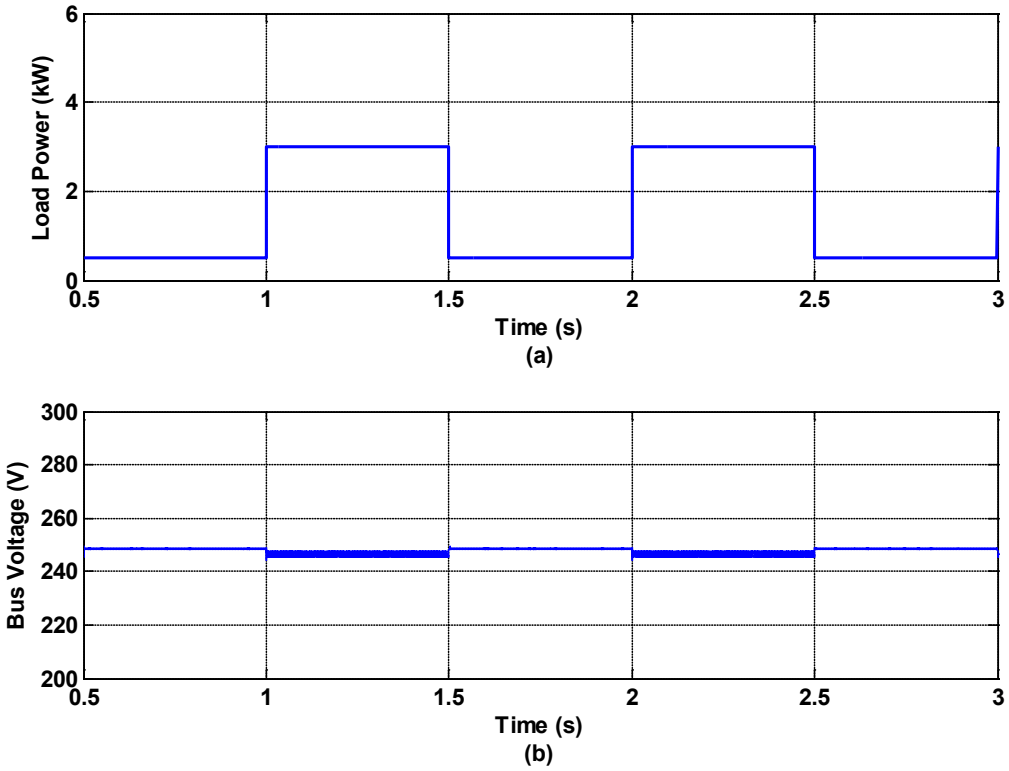

Fig. 4.12. Effectiveness of APDN for system expansion – (a): Profile of connected load, (b): Bus Voltage after modification to the original system

Classification		Characteristics
Original	Source	DC Source Input: 500V, Output: 250V
	Load	Constant Power Load : Regulated DC-DC Converter (500W)
Expansion	New Load	Constant Power Load with pulsed profile Regulated DC-DC Converter (0.5kW~3kW) Load Profile shown in Fig. 4.12 (a)

Table 4.3. Source/Load Characteristics considered for system expansion

4.6 CONCLUSION

This chapter discussed the application of APDN as modular interface block for implementing modular microgrid. The characteristics of APDN as an interconnection interface and a power buffer are explored. The advantages of using APDNs as a connection interface inside a power network are studied from an availability point of view in a quantitative manner by performing a comparison using Markov-based availability models. By having multiple bi-directional interface modules and embedded energy storage, APDNs are able to perform as a power buffer to handle power imbalances among sources and loads. As a power buffer, the APDN can be used to enable local energy management of zones decoupled from the rest of the network. Furthermore, such decoupling simplifies expansion planning of microgrids by enabling a modular approach based on a sectionalized power distribution architecture. Performance of the APDN used as a power buffer is verified by both simulation and experiments.

Chapter 5. Effect of Modular Operations and Microgrids

5.1 INTRODUCTION

Microgrids are being considered as a solution for implementing a resilient power network with higher operational flexibility. During the overall operation phase of microgrids, the microgrid configuration could change depending on operation needs. Examples of such configuration changes include addition or removal of sources, and connection of loads with varying dynamics. To achieve high level of operational flexibility, it is preferable for microgrids to accommodate such configuration modifications with minimized effort. In other words, microgrids should be able to support plug and play (PnP) operation [117]. This PnP characteristic can be achieved by considering modular implementation or modular operation of microgrids.

Modular implementation of microgrids can be realized by considering the use of modular circuit interfaces. Examples of such interfaces include multiple input converters (MICs) [25], and active power distribution nodes (APDNs) [118]. However, the advantage of having a modular configuration cannot be truly achieved without the use of autonomous or decentralized control approaches. Droop control is a common approach that enables decentralized control of microgrids [37] in which the control command for each source is generated by using only the local feedback information (e.g., voltage, and current) without a centralized controller. Hence, droop control enables modular operation of microgrids.

This chapter studies how a modular operation (i.e., PnP operation) can affect the transient performance of system frequency in an inverter-based microgrid. It is reasonable to predict that microgrids formed with power electronic interfaces would become more popular supported by the increased interest toward using distributed generation and renewable power source. Although the inverter-based connection

increases operational flexibility and may be preferable for modular operation of microgrids, the low inertia characteristics introduce challenges in maintaining stability [12]. For instance, consider a modular microgrid power system [67] as shown in Fig. 5.1. While the system has an inverter based architecture that is preferable for modular operation, it is necessary to study how the system would operate after the source configuration is modified. Modifications can occur for various reasons, such as maintenance [67] and system expansion [8]. This research considers the use of an inertia index based on the analogy between the inertia constant of synchronous generators and control parameters of droop controlled inverters [119], [120] to study the effect of modular operation on microgrid performance. It is shown that the inertia index value is related with the transient response characteristics (e.g., settling time) of the microgrid frequency to a power imbalance introduced to the system.

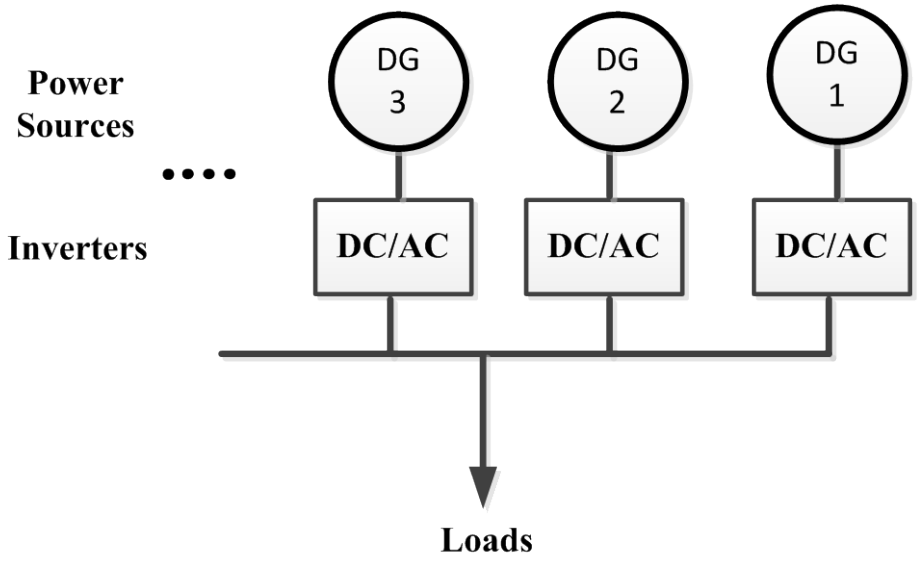

Fig. 5.1. Example of a Modular Microgrid System

5.2 INVERTER BASED MICROGRIDS AND INERTIA INDEX

5.2.1 System Inertia and Stability

Frequency stability of a power system highly depends on amount of inertia of the system. This could be explained using the dynamic equations of the synchronous generator as [119], [121]

$$2H\left(\frac{d\omega}{dt}\right) = P_m - P_e - D\omega \tag{5.1}$$

$$H = \frac{\frac{1}{2}J\omega_m^2}{S_b} \tag{5.2}$$

where H is the inertia constant of the generator, ω is the angular frequency, P_m is the mechanical shaft power, P_e is the electrical load power, D is the damping coefficient, J is the moment of inertia of the generator, ω_{m} is the synchronous angular velocity of the rotor, and S_b is the VA rating of the generator.

In case of a synchronous generator, rotor provides inertia to the power system so that the frequency deviation caused by power imbalances can be minimized. Equation (5.1) shows that a power system powered by a synchronous generator with a smaller inertia constant value will show a larger *df/dt*, rate of change of frequency (ROCOF), value for a same amount of power imbalance between the source and the load. As the overall frequency variation caused by a load disturbance is determined by the ROCOF value during transients, the inertia constant, H, plays an essential role so that the frequency deviation throughout the power transient period does not exceed frequency regulation requirements. For power systems with multiple generators connected, the equivalent system inertia constant could be calculated as [121]

$$H_{sys} = \frac{\sum_i S_i H_i}{S_{base}} \tag{5.3}$$

where S_i is the ratings, and H_i is the inertia constant of the i^{th} generator, and S_{base} is the microgrid base ratings.

While synchronous generators with large inertia are mostly used in conventional power systems, distributed generation sources (e.g., photovoltaic, fuel cells, and energy storage) are primarily used in microgrids. These distributed generation sources are typically connected to a microgrid through power electronic interfaces. High penetration of electronically coupled generation sources causes achieving stable operation points in microgrids to be more challenging compared to the cases in conventional "stiff" power systems. This difficulty can be explained by the fact that power electronic interfaces have low inertia compared to synchronous generators [12]. The intermittent nature of renewable energy sources, furthermore, increases the risk for the power system to experience power imbalances that could affect system stability [8].

5.2.2 Inverter Control Structure and System Dynamics

The schematic of an inverter connected to a microgrid is shown in Fig. 5.2, and the control structure of the inverter is shown in Fig. 5.3.

The considered control loop has a cascaded structure with the power control loop being the most outer (or slowest) loop and the current loop being the most inner (or fastest) loop. Considering its popularity, PI control is considered for both voltage and current control [42], [122], [123], and a feedforward term is added to address the coupling effect between the d-axis and q-axis.

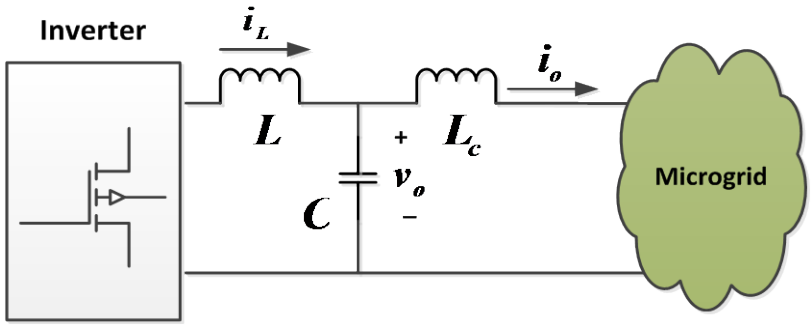

Fig. 5.2. Schematic of an inverter connected to a microgrid

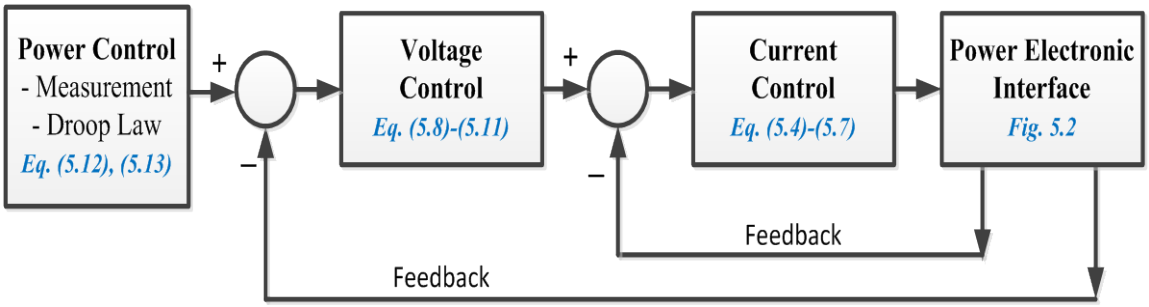

Fig. 5.3. Typical Cascaded Control Structure for a droop controlled inverter

Hence, the dynamic equations of the current control loop can be written as [122]

$$\frac{d\varphi_{id}}{dt} = e_{id} = i_{Ld}^{*} - i_{Ld} \tag{5.4}$$

$$\frac{d\varphi_{iq}}{dt} = e_{iq} = i_{Lq}^{*} - i_{Lq} \tag{5.5}$$

$$v_d^{*} = K_{ii}\varphi_{id} + K_{pi}e_{id} - \omega L i_{Lq} \tag{5.6}$$

$$v_q^{*} = K_{ii}\varphi_{iq} + K_{pi}e_{iq} + \omega L i_{Ld} \tag{5.7}$$

where L is the inductance value of the output filter, φ_{id}, and φ_{iq} are the state variables of the controller, K_{pi} and K_{ii} are the controller gains, i_{Ld} and i_{Lq} are the d-axis and q-axis component of the inductor current, ω is the synchronous angular frequency, v_d^* and v_q^* are the d-axis and q-axis component of the voltage command, i_{Ld}^* and i_{Lq}^* are the command values of the d-axis and q-axis current.

The state equations of the voltage controller can be written as [122]

$$\frac{d\varphi_{vd}}{dt} = e_{vd} = v_{od}^* - v_{od} \tag{5.8}$$

$$\frac{d\varphi_{vq}}{dt} = e_{vq} = v_{oq}^* - v_{oq} \tag{5.9}$$

$$i_{Ld}^* = -\omega C v_{oq} + K_{pv} e_{vd} + K_{iv} \varphi_{vd} + H i_{Ld} \tag{5.10}$$

$$i_{Lq}^* = \omega C v_{od} + K_{pv} e_{vq} + K_{iv} \varphi_{vq} + H i_{Lq} \tag{5.11}$$

where φ_{vd}, and φ_{vq} are the controller state variables, K_{iv} and K_{pv} are the controller gains, H is the feedforward gain, i_{Ld} and i_{Lq} are the d-axis and q-axis current, and C is the capacitance value of the output filter.

As the control loops of Fig. 5.3 are designed so that the bandwidth of each control loop is sufficiently far from others [42], it is reasonable to assume that the system dynamics can be characterized by the dynamics of the most outer control loop (i.e., the power control loop). As shown in Fig. 5.4, the power control loop consists of the power calculation block, power filter block, and the droop law.

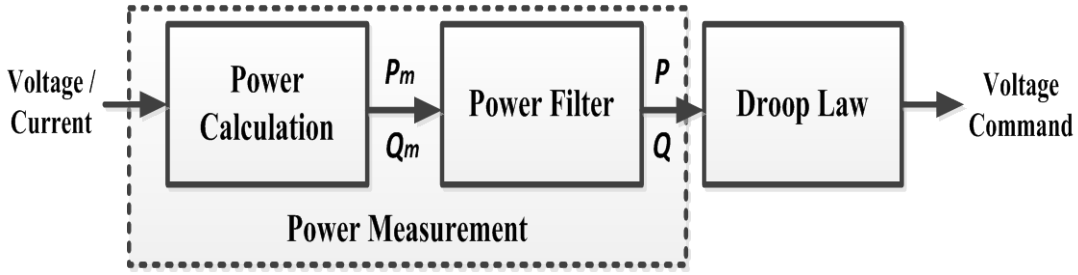

Fig. 5.4. Block Diagram of Power Control Loop

The power filter is a low pass filter as

$$\begin{cases} T\dfrac{dP}{dt} = -P + P_m \\ or \\ \dfrac{dP}{dt} = -\omega_c P + \omega_c P_m \end{cases} \tag{5.12}$$

where T and ω_c are the time constant and cut-off angular frequency of the power filter, P is the filtered power value, and P_m is the actual power value.

With the inverter controlled by the droop law of the form [120]

$$\omega^* = \omega_0 - m(P - P^*) \tag{5.13}$$

where ω_0 is the nominal angular frequency, ω^* is the reference of the angular frequency, and m is the frequency droop gain, the frequency dynamics of a droop controlled inverter can be written based on [119], [120] as

$$\frac{T}{m}\left(\frac{d\omega}{dt}\right) = P^* - P - \frac{1}{m}\omega \tag{5.14}$$

Equation (5.14) shows that both the time constant of the low pass filter, T, and the droop gain, m, affects the stability characteristics of the droop controlled microgrid..

5.2.3 Inertia Index

Equation (5.14) shows that the power filter time constant and the droop gain affects the transient response of the frequency. Furthermore, a comparison between (5.1) and (5.14) shows that the role of the T/m value of droop controlled inverters is analogous to that of the inertia constant of synchronous generators [119], [120].

In order to show that the power filter, (5.12), affects the transient response, a 220 Vrms/50Hz ac microgrid (i.e. Fig. 5.5 (b)) was simulated using MATLAB/SimpowerSystems. The cable impedance is set as Z_{cable}=0.3+j0.1, which has non-negligible resistance value as in most cases of microgrids [122]. The control parameter values are as the following [42], [122]: L=1.5 mH, C=50 uF, L_c=0.35 mH, m= 2×10^{-4} rad/s/W, n= 1×10^{-3}V/Var, K_{pi}=10.5, K_{ii}=16,000, K_{pv}=0.05, K_{iv}=390, H=0.75. Figure 5 (a) shows how the system frequency changes after the load is increased at t=1s in the droop controlled microgrid (i.e., Fig. 5(b)). The plot of Fig. 5 (a) was obtained by simulating the microgrid, while keeping the system parameters invariant for various values of the cut-off frequency of the power filter. As the droop gain is same in all of the simulation cases, the steady-state frequency value is the same for all simulation cases. However, it could be seen that the microgrid frequency shows a faster decrease to its steady-state value as the cut-off angular frequency, ω_c, increases.

Based on the previously discussed analogy (i.e., H of (5.1) and T/m of (5.14)), an inertia index for inverter based microgrids, H_{inv}, can be considered as

$$H_{inv} = \sum_{i=1}^{N} \left(\frac{T_i}{m_i}\right) = \sum_{i=1}^{N} \left(\frac{1}{\omega_{ci} m_i}\right) \tag{5.15}$$

where T_i is the time constant, ω_{ci} is the cut-off angular frequency of the power filter, m_i is the droop gain of the i^{th} inverter, and N is the total number of inverters that are connected to the microgrid.

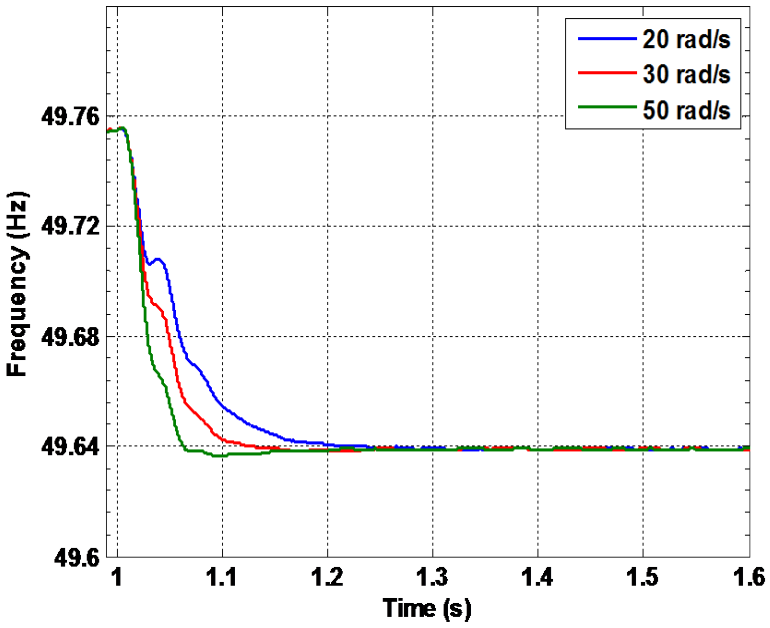

(a) Frequency

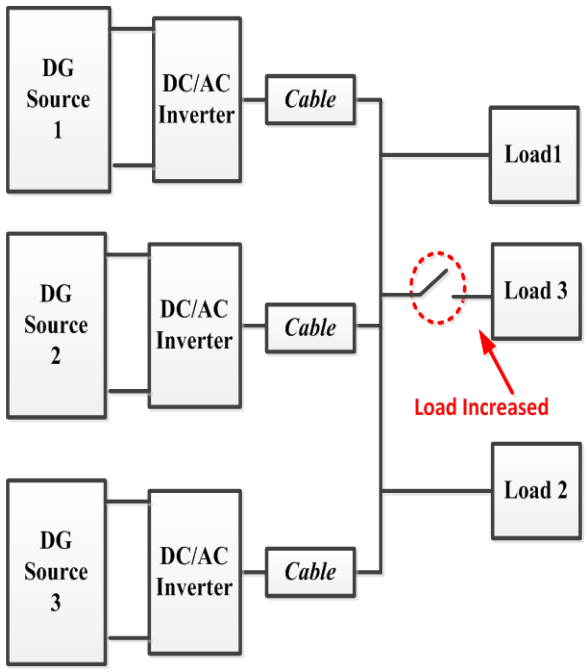

(b) Configuration

Fig. 5.5 Frequency and Configuration of Microgrid (Load Increased)

5.3 INERTIA INDEX AND MODULAR OPERATION

The H_{inv} value is determined not only by the settings of the power control loop (e.g., droop gain and time constant of the power filter) but also by the number of inverters that are connected. To demonstrate the change in the frequency dynamics, a microgrid with a configuration of Fig. 5.6(b) was simulated with different number of inverters (2 units vs. 3 units) connected.

Consider a microgird has three sources, and the cut off angular frequency of the power filter of each inverter was set as ω_c =40 rad/s. For this original configuration, an increase in the load power at t=0.5s resulted in a frequency droop from f=49.75 Hz to 49.63 Hz, as shown in blue line of Fig. 5.6(a), and the ROCOF during this period is calculated as 1.2 Hz/s. If one of the inverters are disconnected (i.e., Source 3 of Fig. 5.6(b)), so that only 2 sources are connected, and if the other parameter values are kept the same, then an increase in the load power at t=0.5 s results in a frequency drop from f=49.63 Hz to 49.45 Hz, as shown in the red line of Fig. 5.6(a). The ROCOF for this case is calculated as 1.8 Hz/s. The difference in the steady-state value can be explained by the fact that the power that a single inverter should handle is higher in the 2-unit case compared to that in the 3-unit case. It is worth to note the increase in the ROCOF value to the identical load increase in the 2-unit case (i.e., configuration after change) compared to the 3-unit case (i.e., configuration before change).

The difference in the ROCOF value can be explained by comparing the inertia index of the two configurations. As the power control loop is identical in both the 3-unit case and the 2-unit case, the inertia index of the 2-unit configuration is only 2/3 of the inertia index of the 3-unit case. This difference results in a response of the microgrid frequency as shown in Fig. 5.6(a).

Such a difference in the system response could be an obstacle for achieving modular operation of microgrids, as a removal of a power source results in changing the dynamics of the microgrid frequency. In this case, the system shows a larger ROCOF value during transients caused by the same amount of load disturbance. This may result in unnecessary operation of protection devices that uses the ROCOF value as a threshold value for their activation. For example, the protection or operation strategies (e.g., circuit breaker operation or load shedding algorithm) based on the original system settings may result in faulty operation and cause unnecessary load shedding or activations of protection devices (e.g., circuit breaker, and relays). Although it is possible to solve these issues by performing adjustments to the system (e.g., modification of protection devices threshold settings [124] and system management algorithms) whenever the configuration is changed, such operation strategy would decrease the advantages of operating a microgrid in a modular fashion [125].

Despite the fact that the frequency deviation at steady-state can be minimized by the control input of high level controllers of a microgrid hierarchical control framework [37], it is worth to note that the transient response of the microgrid frequency is mostly determined by the primary control level, which is the scope of this research. This can be explained by the different time scales between controllers at different hierarchical levels [37]. Hence, it is beneficial to use the inertia index so that the response characteristics of the microgrid frequency during power transients can be studied by simply comparing the inertia index, instead of performing simulation of the overall microgrid.

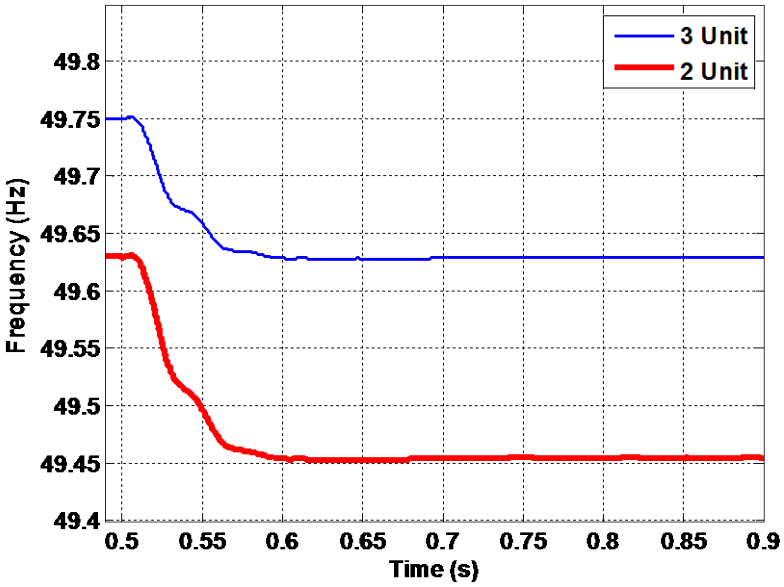

(a) Frequency

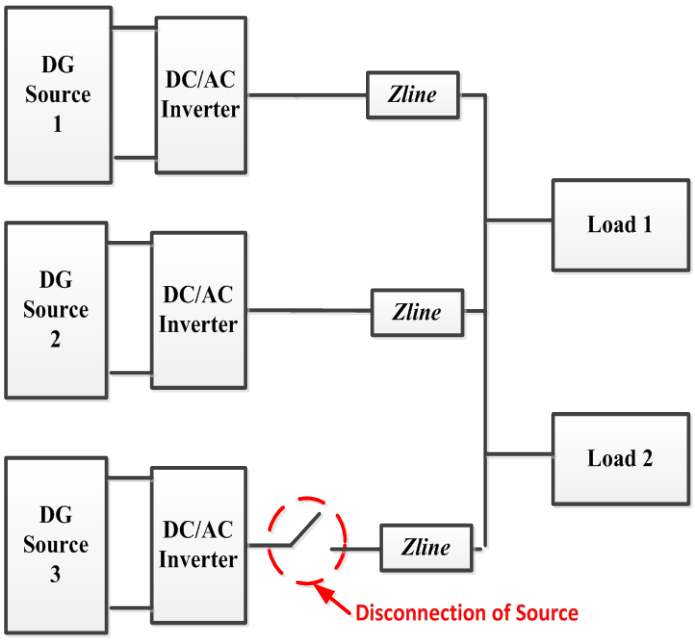

(b) Configuration

Fig. 5.6. Frequency and Configuration of a Microgrid (Source Disconnected)

5.4 APPLICATION OF INERTIA INDEX

As the inertial response characteristics of a power system is related to the inertia constant (i.e., H in (5.1)), this study considers the use of the inertia index for developing an approach to minimize the effect of source configuration modifications on the microgrid frequency transient response. As the inertia index is a function of both the number of source inverters connected, and the time constant of the power filter, it is possible to consider changing the time constant of the power filter when a change in the source configuration is detected. Although the power control loop significantly affects the microgrid frequency command dynamics as discussed in section 5.2, studies on how the time constant of the power filter could affect the system performance [127] is rather limited compared to the effect of the droop gain [1], [42], [38], [70] .

A possible approach to find a new cut off frequency, ω_c, that minimizes the effect of the change in the value of N is to update the power filter cut off frequency so that the inertia index of the original case and the modified case is identical. That is, finding the new cut-off angular frequency, $\omega_{ca,}$ that satisfies

$$\frac{N_b}{m\omega_{cb}} = \frac{N_a}{m\omega_{ca}} \tag{5.16}$$

where N_b is the number of sources connected to the microgrid before the configuration change, ω_{cb} is the cut-off frequency of the power filter before the configuration change, m is the droop gain, N_a is the number of sources connected to the microgrid after the configuration change, and ω_{ca} is the cut-off frequency of the power filter after the configuration change.

For the case that was discussed in the previous section (i.e., Fig. 5.6(b)), the new cut-off frequency of the low pass filter, ω_{ca}, can be found as

$$\frac{3}{40 \cdot m} = \frac{2}{\omega_{ca} \cdot m} \tag{5.17}$$

where ω_{ca} is the updated power filter time constant for the 2-unit case, and m is the frequency droop gain.

In order to verify the effectiveness of this approach, the same microgrid (i.e., Fig. 5.6(b)) was simulated using the same parameters except the time constant of the power filter. Figure 5.7 shows the microgrid frequency when only two units are connected with power filters that have different time constant values. In order to mitigate the increased ROCOF value caused by the sudden disconnection of sources, the cut-off angular frequency of the low pass filter was changed from ω_c=40 rad/s to ω_c=27 rad/s. It can be seen from Fig. 5.7, as a result, that the microgrid frequency shows a slower decrease to the new steady-state value by changing the low pass filter time constant. The reduction in the inertia constant caused by disconnecting one of the sources is complemented by changing the low pass filter time constant to a larger value. By changing the time constant of the low pass filter, the ROCOF value decreased from 1.8 Hz/s to 1.2 Hz/s.

This approach could be considered as a method to improve the stability characteristics of an inverter-based microgrid. Similar to a power grid with a large inertia constant, a slower frequency change would be desirable when operating an inverter based microgrid [126]. In case a frequency deviation happens as a result of power imbalance, it would be preferable to have a longer time available to perform corrective actions before the frequency reaches its threshold value.

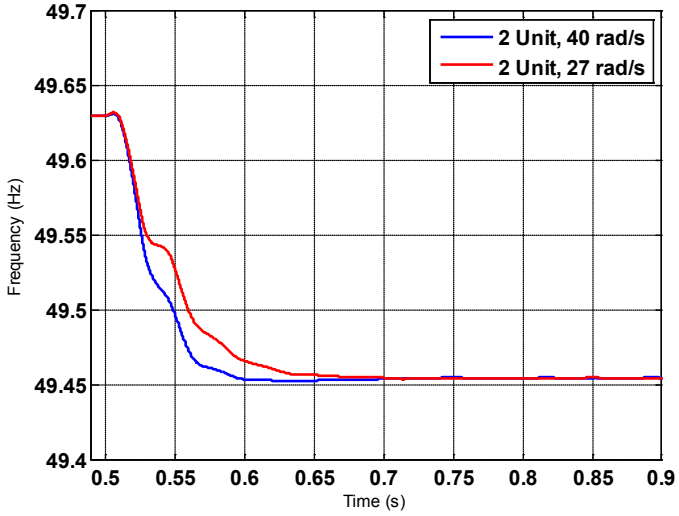

Fig. 5.7. Microgrid Frequency with different low pass filter characteristics

Considering that the system inertia changes depending on both the control parameters (e.g., droop gain, and power filter time constant) and source configuration, it is possible to consider a power control law that updates the time constant of the power filter depending on the source configuration as shown in Fig. 5.8. Once a change in the source configuration is detected, the power filter time constant can be changed according to the virtually stored table in Fig. 5.8. It is worth to note that there are operational constraints that the new time constant (or the cut-off frequency) of the power filter should satisfy [127]. The time constant should be selected so that the response of the inverter is not too slow and also that the inner voltage and current control loop is sufficiently faster than the most outer power control loop so that each cascaded control loop does not interact with other loops.

Still, it is possible to consider alternative approaches to minimize the change in transient performance caused by the plug and play operation of sources in microgrids. For

example, it is possible to apply an alternative droop law that includes a transient droop term given by [12]

$$\omega^* = \omega_0 - m_s(P - P^*) - m_{t1}\left(\frac{df}{dt}\right)^k (P - P^*) \tag{5.18}$$

where, m_s is the static droop gain, and m_{t1} is the transient droop gain that is active when only the *df/dt* value is large than the preset threshold value.

However, the control approach of (5.18) has higher level of complexity compared to the droop law in (5.13). Although the control approach of (5.18) introduces additional inertia to the system [12], further optimization on the controller gains is required to achieve satisfactory transient response characteristics (e.g., overshoot, settling time, etc.) [128]. In addition, the derivative term in the control law is known to be sensitive to noise and the performance of the derivation operation highly depends on the time step settings.

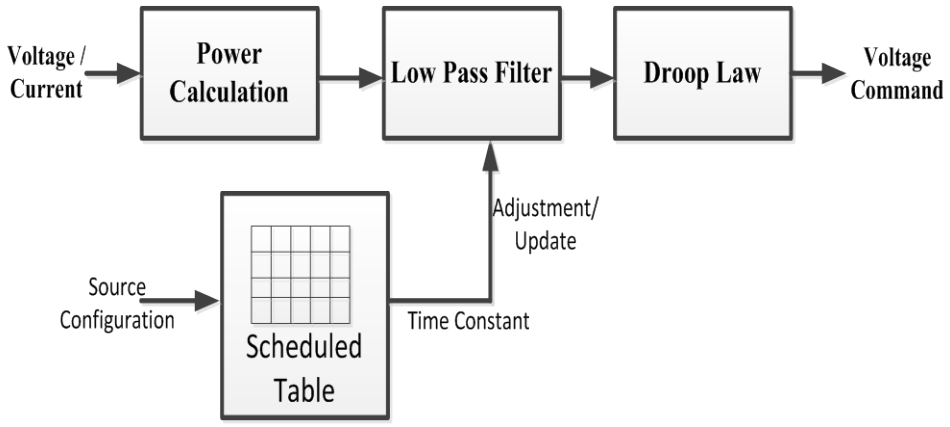

Fig. 5.8. Control with Time Constant Scheduled Low Pass Filter

5.5 CONCLUSION

This chapter studied the effect of modular operation on transient performance of frequency in an inverter based microgrid. Microgrids with high penetration of power electronic interfaces are known to have lower inertia compared to conventional power grid systems. Such a low inertia imposes challenges for frequency stability in inverter-based microgrids. Using the analogy between synchronous generators and droop controlled inverters, an inertia index that provides insights on the transient response of system frequency is studied. Based on the fact that the inertia index is a function of the number of source inverters, the inertia index can be used to study the effects of addition or removal of inverters to the microgrid frequency during transients This research also studied on how changing the time constant of the power measurement filter could mitigate the change in the microgrid frequency dynamics caused by modular operation.

Chapter 6. Conclusion

This dissertation discussed design and operation of modular microgrids with an open architecture. As microgrids are expected to accommodate various type of configuration changes (e.g., installation of new loads, removal/addition of sources) throughout the operation period, it is beneficial to study design and operation approaches of microgrids considering modularity (i.e., plug and play operation).

The use of active power distribution nodes (APDNs) as an interface block that enables a modular approach for microgrids is studied in this research. The bi-directional multiple-input multiple-output (MIMO) interface of APDNs can enhance power network operational flexibility by enabling and controlling multiple power flow paths. The embedded energy storage of the APDN can act as a power buffer by handling the power mismatch between sources and loads, and perform as a back-up power source during power loss. Based on these features of the APDN configuration—i.e. power electronic MIMO interface with embedded energy storage—power network planning, expansion, and protection coordination for ac, dc, or hybrid networks can be done in a modular fashion.

Considering the operation of APDN as an energy management interface inside a microgrid, this research investigated the characteristics of the interface and identified operation states of the APDN. As the state of the embedded energy storage plays a critical role in the performance of APDN, this research proposed two hierarchical control approaches. The first hierarchical controller, lower level for signals and higher level for energy management, focuses on maintaining the charge level of the embedded energy storage to the highest level to increase system availability. The other hierarchical approach considers a hierarchy such that the primary level performs load sharing by

using a droop law, and the secondary level manages energy storage in a decentralized manner. In order to effectively manage the embedded energy storage, the secondary controller switches between current control mode and voltage control mode depending on the state of energy storage. The control performance and energy management capability of both control approaches was verified by simulation and experiments. It is shown that the APDN performs autonomous power sharing between different power sources, and storage management, which is critical for using APDN as power routers. The developed control approach can also be used as a generalized control framework for storage integrated power electronic interfaces.

Furthermore, this dissertation explored the characteristics of using APDN as a connection interface inside a microgrid. By using a Makov-based availability model, it is shown that APDNs can improve system availability compared to conventional connection interfaces, such as circuit breakers. Although APDNs may have a higher part count compared to circuit breakers, availability comparison results show that the embedded energy storage of APDNs can outweigh the circuit complexity of APDNs. A simplified cost analysis result shows that the benefits of using APDNs increase as the criticality of the load increases. Compared to circuit breakers, APDNs are able to effectively handle series faults and interrupt dc currents based on the current limiting capability of the power electronic interface. Based on the capability of APDNs to handle power imbalance, two system design approaches of using APDN for microgrids are also introduced. It is shown that the APDN can be placed at major nodes of the microgrid to ensure that critical loads are not affected by source conditions. Furthermore, microgrid expansion can be performed in a simpler manner by connecting the expanded system through APDNs. This characteristic ensures that the operation of both the original system and the expanded system is not affected by the dynamics of each other. As a result,

APDNs enable open modular architectures for microgrids. The effectiveness of APDNs as an interface for microgrid operation and system expansion was also demonstrated.

Finally, the effect of modular operation on microgrids is also studied. Based on the analogy between synchronous generators and droop controlled inverters, an inertia index that provides insights on the microgrid frequency transient response is studied. As the inertia index is a function of the number of source inverters and the control parameters of the power control loop, the inertia index was used to study the effects of addition or removal of inverters to the microgrid frequency during transients.

The results of this dissertation can be used for modular design and operation of microgrids. For example, APDNs can be integrated within dc, ac or hybrid ac/dc microgrids to perform the roles of a power router and enable distributed power control. Furthermore, the proposed APDN, with the discussed hierarchical control approaches, can serve as a building block for enabling modular connection and distributed power management for future power systems. The APDN-enabled advanced power distribution architectures provide more cost effective and comprehensive solution in order to enhance power distribution grids availability during extreme events, such as storage, than traditional solutions suggested for electric utilities. The observations that are made regarding how the removal and addition of modular sources from a microgrid can also be considered during the design and operation phase of modular microgrids.

References

[1] Z. Miao, A. Domijian, Jr., and L. Fan, "Investigation of Microgrids with Both Inverter Interfaced and Direct AC-Connected Distributed Energy Resources," *IEEE Trans. Power Delivery*, vol. 26, no. 3, pp. 1634-1642, Jul. 2011.

[2] D. Salomonsson, L. Soder, and A. Sannino, "An Adaptive Control System for a DC Microgrid for Data Centers," *IEEE Trans. Industry Applications*, vol. 44, no. 6, pp. 1910-1917, Nov. 2008.

[3] J. Schonberger, R. Duke, and S. D. Round, "DC-Bus Signaling: A Distributed Control Strategy for a Hybrid Renewable Nanogrid," *IEEE Trans. Industrial Electronics*, vol. 53, no. 5, pp. 1453-1460, Oct. 2006.

[4] A. Kwasinski, "Advanced power electronic enabled distribution architectures: design, operation, and control," in *Proc. Int'l Conf. on Power Electronics-ECCE Asia*, 2011, pp. 1-8.

[5] N. Hatziargyriou, H. Asano, R. Iravani, and C. Marnay, "Microgrids", *IEEE Power & Energy Magazine*, vol. 5, no. 4, pp.78-94, Jul./Aug. 2007

[6] B. Kroposki, R. Lasseter, T. Ise, S. Morozumi, S. Papathanassiou, and N. Hatziargyriou, "Making Microgrids Work," *IEEE Power & Energy Magazine,* vol. 6, no. 3, pp.40-53, May/Jun. 2008.

[7] (2012, Jun.). Lincoln Laboratory Technical Report 1164, *Microgrid Study: Energy Security for DoD Installations*.

[8] M. Kim, and A. Kwasinski, "Distribution Interface for Microgrid operation and Expansion with Local Energy Management," in *Proc. IEEE 5th Int'l Symp. On Power Electronics for Distributed Generation Systems (PEDG)*, 2014, pp.1-8.

[9] T. L. Vandoorn, B. Meersman, J. D. M. De Kooning, and L. Vandevelde, "Analogy Between Conventional Grid Control and Islanded Microgrid Control Based on a Global DC-Link Voltage Droop," *IEEE Trans. Power Delivery*, vol. 27, no. 3, pp. 1405-1414, Jul. 2012.

[10] F. Katiraei, R. Iravani, N. Hatziagyriou, and A. Dimeas, "Microgrids Management," *IEEE Power and Energy Magazine*, vol. 6, no. 3, pp.54-65, May 2008.

[11] C. K. Sao, and P. W. Lehn, "Control and Power Management of Converter Fed Microgrids," *IEEE Trans. Power Systems*, vol. 23, no. 3, pp.1088-1098, Aug, 2008.

[12] N. Soni, S. Doolla, and M. C. Chandorkar, "Improvement of Transient Response In Microgrids using Virtual Inertia," *IEEE Trans. Power Delivery*, vol. 28, no. 3, pp.1830-1838, Jul. 2013.

[13] A. Kwasinski, and C. N. Onwuchekwa, "Dynamic Behavior and Stabilization of DC Microgrids with Instantaneous Constant-Power Load," *IEEE Trans. Power Electronics*, vol. 26, no.3, pp.822-834, Mar. 2011.

[14] F. Z. Peng, Y. W. Li, and L. M. Tolbert, "Control and Protection of Power Electronics Interfaced Distributed Generations Systems in a Customer-Driven Microgrid," in *Proc. IEEE Power & Energy Society General Meeting (PES)*, 2009, pp.1-8.

[15] P. Stulak, D. Godbole, and T. Samad, "Energy Management for Buildings and Microgrids," in *Proc. 5th IEEE Conf. on Decision and Control and European Control Conference* 2011, vol.2, pp.5150-5157.

[16] J. Mitra, and M. R. Vallem, “Determination of Storage Required to Meet Reliability Guarantees on Island-Capable Microgrids with Intermittent Source,” *IEEE Trans. Power Systems*, vol. 27, no. 4, pp. 2360-2367, Nov. 2012.

[17] T. Ersal, C. Ahn, D. L. Peters, J. W. Whitefoot, A. R. Mechtenberg, I. A. Hiskens, H. Peng, A. G. Stefanopoulou, P. Y. Papalambros, and J. L. Stein, “Coupling Between Component Sizing and Regulation Capability in Microgrids,” *IEEE Trans. Smart Grid*, vol. 4, no. 3, pp. 1576-1585, Sep. 2013.

[18] A. D. Dominguez-Garcia, J. G. Kassakian, and J. E. Schindall, “Reliability evaluation of the power supply of an electrical power net for safety-relevant applications,” *Journal of Reliability Engineering and System Safety*, vol. 91, no.5, pp.505-514, May 2006

[19] R. D. Telford, S. J. Galloway, and G. M. Burt, “Evaluating the Reliability & Availability of more-electric aircraft power systems,” in *Proc. 47th Universities Power Engineering Conference (UPEC),* 2012, pp.1-6.

[20] A. Kwasinski, V. Krishnamurthy, J. Song, and R. Sharma, “Availability Estimation of Micro-Grids for Resistant Power Supply During Natural Disaster,” *IEEE Trans. Smart Grid*, vol. 3, no. 4, pp. 2007-2018, Dec. 2012

[21] V. Krishnamurthy and A. Kwasinski, “Characterization of Power System Outages Caused by Hurricanes through Localized Intensity Indices,” in *Proc. IEEE Power and Energy Society General Meeting (PES),* 2013, pp.1-5

[22] D. Boroyevich, I. Cvetkovic, R. Burgos, and D. Dong, “Intergrid: A Future Electronic Energy Network?,” *IEEE Journal of Emerging and Selected Topics in Power Electronics*, vol. 1, no. 3, pp.127-138, Sep. 2013.

[23] W. Chen, X. Ruan, H. Yan, and C. K. Tse, "DC/DC Conversion Systems Consisting of Multiple Converter Modules: Stability, Control, and Experimental

Verifications," *IEEE Trans. Power Electronics*, vol. 24, no. 6, pp. 1463-1474, Jun. 2009.

[24] H. Kim, M. Falahi, T. M. Jahns, and M. W. Degner, "Inductor Current Measurement and Regulation Using a Single DC Link Current Sensor for Interleaved DC-DC Converters," *IEEE Trans. Power Electronics*, vol. 26, no. 5, pp. 1503-1510, May 2011.

[25] S. Bae, and A. Kwasinski, "Dynamic Modeling and Operation Strategy for a Microgrid with Wind and Photovoltaic Resources," *IEEE Trans. Smart Grid*, vol. 3, no. 4, pp. 1867-1876, Dec. 2012.

[26] Y. Chen, D. Y. Chen, Y. Wu, and F. Shih, "Small-Signal Modeling of Multiple-Output Forward Converters with Current-Mode Control," *IEEE Trans. Power Electronics*, vol. 11, no. 1, pp. 122-131, Jan. 1996.

[27] R. Zhao, and A. Kwasinski, "Controller analysis for active distribution nodes in advanced dc power systems," in *Proc. IEEE Control and Modeling for Power Electronics (COMPEL),* 2012, pp. 1-8.

[28] A. Kwasinski, "Quantitative Evaluation of DC Microgrids Availability: Effects of System Architecture and Converter Topology Design Choices," *IEEE Trans. Power Electronics*, vol. 26, no.3, pp. 835-851, Mar. 2011.

[29] A. Kwasinski, "Technological assessment of distributed generation systems operation during extreme events," in *Proc. of IEEE Int'l Symp. Power Electronics for Distributed Generation Systems (PEDG),* 2012, pp. 534-541.

[30] A. Kwasinski, "Towards a "Power-Net": Impact of Smart Grids Development for ICT Networks During Critical Events," in *Proc. 3rd Int'l Symp. on Applied Sciences in Biodmedical and Comm. Tech.-ISABEL* 2011, pp.1-8.

[31] X. She, A. Q. Huang, S. Lukic, and M. E. Baran, "On Integration of Solid-State Transformer with Zonal DC Microgrid," *IEEE Trans. Smart Grid*, Vol. 3, no. 2, pp. 975-985, Jun. 2012.

[32] W. Lin, and D. Jovcic, "High reliability Multiport Multiphase DC Hub," in *Proc. Industry Applications Society Annual Meeting (IAS)* 2013, pp. 1-8.

[33] H. Keyhani, and H. A. Toliyat, " A ZVS single-inductor multi-input multi-output DC-DC converter with the step up/down capability," in *Proc. IEEE Energy Conversion Congress and Exposition (ECCE)* 2013, pp. 5546-5552.

[34] B. T. Irving, and M. M. Jovanovic, "Analysis, design, and performance evaluation of droop current-sharing method," in *Proc. IEEE Applied Power Electronics Conference and Exposition (APEC),* 2000, pp. 235-241.

[35] Y. Pei, G. Jiang, X. Yang, and Z. Wang, "Auto-master-slave control technique of parallel inverters in distributed AC power systems and UPS," in *Proc. IEEE Applied Power Electronics Conference and Exposition (APEC)*, 2004, pp. 456-462.

[36] X. Sun, Y.-S. Lee, and D. Xu, "Modeling, analysis, and implementation of parallel multi-inverter system with instantaneous average-current-sharing scheme," *IEEE Trans. Power Electronics*, vol. 18, no. 3, pp. 844-856, May 2003.

[37] J. M. Guerrero, J. C. Vasquez, J. Matas, L. G. Vicuna, and M. Castilla, "Hierarchical Control of Droop-Controlled AC and DC Microgrids- A General Approach Toward Standardization," *IEEE Trans. Industrial Electronics*, vol. 58, no. 1, pp. 158-172, Jan. 2011.

[38] S. Anand, and B. G. Fernandes, "Reduced-Order Model and Stability Analysis of Low-Voltage DC Microgrid," *IEEE Trans. Industrial Electronics*, vol. 60, no. 11, pp.5040-5049, Nov. 2013.

[39] D. Boroyevich, I. Cvetkovic, D. Dong, R. Burgos, F. Wang, and F. Lee, "Future Electronic Power Distribution Systems – A contemplative view," in *Proc. Int'l Conf. on Optimization of Electrical and Electronic Equipment (OPTIM)* , 2010, pp. 1369-1380.

[40] J. Rocabert, A. Luna, F. Blaabjerg, and P. Rodriguez, "Control of Power Converters in Ac Microgrids," *IEEE Trans. Power Electronics*, vol. 27, no. 11, pp. 4734-4749, Nov. 2012.

[41] R. Majunmder, B. Chaudhuri, A. Ghosh, R. Majumder, G. Ledwich, and F. Zare, "Improvement of Stability and Load Sharing in an Autonomous Microgrid using Supplementary Droop Control Loop," *IEEE Trans. Power Systems*, vol. 25, no. 2, pp. 796-808, May 2010.

[42] Y. A.-R. I. Mohamed, and E. F. El-Saadny, "Adaptive Decentralized Droop Controller to Preserve Power Sharing Stability of Paralleled Inverters in Distributed Generation Microgrids," *IEEE Trans. Power Electronics*, vol. 23, no. 6, pp. 2806-2816, Nov. 2008.

[43] Y. Du, A. Q. Huang, X. Yu, and J. Li, "Droop Controller Design Methods for Isolated DC-DC Converter in DC Grid Battery Energy Storage Applications," in *Proc. IEEE Applied Power Electronics Conference and Exposition (APEC),* 2013, pp. 1630-1637.

[44] J. M. Guerrero, L. G. de Vicuna, J. Matas, M. Castilla, and J. Miret, "Output Impedance Design of Parallel-Connected UPS Inverters with Wireless Load-Sharing Control," *IEEE Trans. Industrial Electronics*, vol. 52, no. 4, pp.1126-1135, Aug. 2005.

[45] A. Bidram, and A. Davoudi, "Hierarchical Structure of Microgrids Control System," *IEEE Trans. Smart Grid*, vol. 3, no. 4, pp. 1963-1976, Dec. 2012.

[46] S. Anand, B. G. Fernandes, and J. M. Guerrero, "Distributed Control to Ensure Proportional Load Sharing and Improve Voltage Regulation in Low-Voltage DC Microgrids," *IEEE Trans. Power Electronics*, vol. 28, no. 4, pp. 1900-1913, Apr. 2013.

[47] X. Lu, J. M. Guerrero, K. Sun, and J. C. Vasquez, "An Improved Droop Control Method for DC Microgrids Based on Low Bandwidth Communication with DC Bus Voltage Restoration and Enhanced Current Sharing Accuracy," *IEEE Trans. Power Electronics*, vol. 29, no. 4, pp. 1800-1812, Apr. 2014.

[48] S. Moayedi, and A. Davoudi, "Distributed Cooperative Load Sharing in Parallel DC-DC Converters," in *Proc. IEEE Applied Power Electronics Conference and Exposition (APEC),* 2014, pp. 2907-2912.

[49] H. Behjati, A. Davoudi, and F. Lewis, "Modular DC-DC Converters on Graphs: Cooperative Control," *IEEE Trans. Power Electronics*, vol. 29, no. 12, pp. 6725-6741, Dec. 2014.

[50] V. Nasirian, S. Moayedi, A. Davoudi, and F. L. Lewis, "Distributed Cooperative Control of DC Microgrids," *IEEE Trans. Power Electronics*, vol. 30, no. 4, pp.2288-2303, Apr. 2015.

[51] Q. Shafiee, J. M. Guerrero, and J. C. Vasquez, "Distributed Secondary Control for Islanded Microgrids- A Novel Approach," *IEEE Trans. Power Electronics*, vol. 29, no.2, pp.1018-1031, Feb. 2014.

[52] A. Bidram, A. Davoudi, and F. L. Lewis, "A Multiobjective Distributed Control Framework for Islanded AC Microgrids," *IEEE Trans. Industrial Informatics*, vol. 10, no. 3, pp. 1785-1798, Aug. 2014.

[53] U. Ozguner, "Decentralized and Distributed Control Approaches and Algorithms," in *Proc. Conference on Decision and Control (CDC),* 1989, pp. 1289-1294.

[54] H. Fakham, D. Lu, and B. Francois, "Power Control Design of a Battery Charger in a Hybrid Active PV Generator for Load-Following Applications," *IEEE Trans. Industrial Electronics*, vol. 58, no. 1, pp. 85-94, Jan. 2011.

[55] P. Thounthong, S. Rael, and B. Davat, "Control Algorithm of Fuel Cell and Batteries for Distributed Generation System," *IEEE Trans. Energy Conversion*, vol. 23, no. 1, pp. 148-155, Mar. 2008.

[56] S. J. Chiang, H. Shieh, and M. Chen, "Modeling and Control of PV Charger System with SEPIC Converter," *IEEE Trans. Industrial Electronics*, vol. 56, no. 11, pp. 4344-4353, Nov. 2009.

[57] Z. Jiang, L. Gao, and R. A. Dougal, "Adaptive Control Strategy for Active Power Sharing in Hybrid Fuel Cell/Battery Power Sources," *IEEE Trans. Energy Conversion*, vol. 22, no. 2, pp. 507-515, Jun. 2007.

[58] *Reliability Prediction of Electronic Equipment*, U.S. Department of Defense, MIL-HDBK-217F, Feb. 1995.

[59] *RDF: 2000: Reliability data handbook, Union technique de L'Electricite*, UTE C 20-810, Jul. 2000.

[60] (2009, May). *Reliability Methodology for Electronic Systems, FIDES Guide 2009*.

[61] M. K. Alam, and E. H. Khan, "Reliability Analysis and Performance Degradation of a Boost Converter," *IEEE Trans, Industry Applications*, vol. 50, no. 6, Nov./Dec. 2014, pp.3986-3994.

[62] K. Zie, Z. Jiang, and W. Li, "Effect of Wind Speed on Wind Turbine Power Converter Reliability," *IEEE Trans. Energy Conversion*, vol.27, no.1, pp.96-104, Mar. 2012.

[63] S. Harb, and R. S. Balog, "Reliability of Candidate Photovoltaic Module-Integrated-Inverter (PV-MII) Topologies- A Usage Model Approach," *IEEE Trans. Power Electronics*, vol. 28, no. 6, pp.3019-3027, Jun. 2013

[64] F. Chan, and H. Calleja, "Reliability Estimation of Three Single-Phase Topologies in Grid-Connected PV Systems," *IEEE Trans. Industrial Electronics*, vol.58, no. 7, pp.2683-2689, Jul. 2011

[65] D. Hirschmann, D. Tissen, S. Schroder, and R. W. De Doncker, "Reliability Prediction for Inverters in Hybrid Electrical Vehicles," *IEEE Trans. Power Electronics*, vol. 22, no. 6, pp.2511-2517 Nov. 2007

[66] R. Burgos, G. Chen, F. Wang, D. Boroyevich, W. G. Odendaal, and J. D. Van Wyk, "Reliability-Oriented Design of Three-Phase Power Converters for Aircraft Applications, "*IEEE Trans. Aerospace and Electronic Systems*, vol. 48. no. 2, pp.1249-1263, Apr. 2012.

[67] S. V. Dhople, and A. D. Dominguez-Garcia, "Estimation of Photovoltaic System Reliability and Performance Metrics," *IEEE Trans. Power Systems*, vol. 27, no. 1, pp.554-563, Feb. 2012.

[68] P. Kundar, J. Paserba, and V. Ajjarapu, "Definition and Classification of Power System Stability," *IEEE Trans. Power Systems*, vol. 19, no. 2, pp.1387-1401, May 2004.

[69] M. J. Basler, and R. C. Schaefer, "Understanding Power-System Stability," *IEEE Trans. Industry Applications*, vol. 44, no. 2, pp.463-474, Mar./Apr. 2008.

[70] E. Barklund, N. Pogaki, M. Prodanovic, C. Hernandez-Aramburo, and T. Green, "Energy Management in autonomous microgrid using stability-constrained droop control of inverters," *IEEE Trans. Power Electronics*, vol. 23, no. 5, pp.2346-2352, Sep. 2008.

[71] N. Bottrell, M. Prodanovic, and T. C. Green, "Dynamic Stability of a Microgrid with and Active Load," *IEEE Trans. Power Electronics*, vol. 28, no. 11, pp. 5107-5119, Nov. 2013

[72] L. Corradini, P. Mattavelli, M. Corradin, and F. Polo, "Analysis of Parallel Operation of Uninterruptible Power Supplies Loaded Through Long Wiring Cables," *IEEE Trans. Power Electronics*, vol. 25, no. 4, pp.1046-1054, Apr. 2010.

[73] B. M. Eid, N. A. Rahin, J. Selvaraj, and A. H. El Khateb, "Control Methods and Objectives for Electronically Coupled Distributed Energy Resources in Microgrids: A Review," *IEEE Systems Journal*, to be published.

[74] A. A. A. Radwan, and Y. A.-R. I. Mohamed, "Assessment and Mitigation of Interaction Dynamics in Hybrid AC/DC Distribution Generation Systems," *IEEE Trans. Smart Grid*, vol. 3, no. 3, pp. 1382-1393, Sep. 2012.

[75] J. M. Guerrero, J. Matas, L. G. de Vicuna, M. Castilla, and J. Miret, "Decentralized Control for Parallel Operation of Distributed Generation Inverters using Resistive Output Impedance," *IEEE Trans. Industrial Electronics*, vol. 54, no. 2, pp.994-1004, Apr. 2007.

[76] R. Majumder, "Some Aspects of Stability in Microgrids," *IEEE Trans. Power Systems*, vol. 28, no. 3, pp.3243-3252, Aug. 2013.

[77] D. E. Olivares, A. Mehrizi-Sani, et al., "Trends in Microgrid Control," *IEEE Trans. Smart Grid*, vol. 5, no. 4, pp. 1905-1919, Jul. 2014.

[78] K. Sun, L. Zhang, and J. M. Guerrero, "A Distributed Control Strategy Based on DC Bus Signaling for Modular Photovoltaic Generation Systems with Battery Energy Storage," *IEEE Trans. Power Electronics*, vol. 26, no. 10, pp.3032-3045, Oct. 2011.

[79] J. A. P. Lopse, C. L. Moreira, and A. G. Madureira, "Defining Control Strategies for Microgirds Islanded Operation," *IEEE Trans. Power System*, vol. 21, no. 2, pp.916-924, May 2006.

[80] S.R. Holm, H. Polinder, J. A. Ferreira, P. van Gelder, and R. Dill , "A Comparison of Energy Storage Technologies as Energy Buffer in Renewable Energy Sources with respect to Power Capability," in *Proc. of IEEE Young Researchers Symp. in Electrical Power Engineering*, 2002.

[81] R. A. Dougal, S. Liu, and R. E. White, "Power and Life Extension of Battery-Ultracapacitor Hybrids," *IEEE Trans. Components and Packaging Tech.* vol. 25, no. 1, pp.120-131, Mar. 2002.

[82] A. Kuperman, and I. Aharon, "Design of a Semiactive Battery-Ultracapacitor Hybrid Energy Source," *IEEE Trans. Power Electronics*, vol. 28 no.2 , pp. 806-815, Feb. 2013.

[83] J. Zhan, J. Lai, and W. Yu, "Bidirectional DC-DC converter modeling and unified controller with digital implementation," in *Proc. IEEE Applied Power Electronics Conference and Exposition (APEC),* 2008, pp.1747-1753.

[84] A. K. Swain, M. J. Neath, U. K. Madawala, D. J. Thrimawaithana, "A Dynamic Multivariable State-Space Model for Bidirectional Inductive Power Transfer Systems," *IEEE Trans. Power Electronics*, vol. 27, no. 11, pp.4772-4780, Nov. 2012

[85] Jie Bao, Peter L. Lee, *Process Control: The Passive Systems Approach*, Springer, 2007.

[86] M. Cugnet, J. Sabatier, S. Laruelle, S. Grugeon, B. Sahut, A. Oustaloup, and J-M. Tarascon, "On Lead-Acid-Battery Resistance and Cranking-Capability Estimation," *IEEE Trans. Industrial Electronics*, vol. 57, no.3, pp.909-917, Mar. 2010.

[87] A. Emadi, *Handbook of Automotive Power Electronics and Motor Drives*, CRC Press, 2005.

[88] R. S. Balog, W. W. Weaver, and P. T. Krein, "The Load as an Energy Asset in a Distributed DC Smart Grid Architecture," *IEEE Trans. Smart Grid*, vol. 3, no. 1, pp.253-260, Mar. 2012.

[89] Z. Jiang, L. Gao, and R. A. Dougal, "Flexible Multiobjective Control of Power Converter in Active Hybrid Fuel Cell/Battery Power Sources," *IEEE Trans. Power Electronics*, vol. 20, no. 1, pp.244-253, Jan. 2005.

[90] K. J. Astrom and B. Wittenmark, *Computer-Controlled Systems*, 3rd ed. Prentice Hall, 1997.

[91] T.-S. Hwang, M. J. Tarca, and S.-Y. Park, "Dynamic Response Analysis of DC-DC Converter With Supercapacitor for Direct Borohydride Fuel Cell Power Conditioning System," *IEEE Trans. Power Electronics*, vol. 27, no. 8, pp. 3605-3615, Aug. 2012.

[92] R. W. Erickson and D. Maksimovic, *Fundamentals of Power Electronics*, 2nd ed. Springer, 2001.

[93] O. Hegazy, J. V. Mierlo, and P. Lataire, "Analysis, Modeling, and Implementation of a Multidevice Interleaved DC/DC Converter for Fuel Cell

Hybrid Electric Vehicles," *IEEE Trans. Power Electronics*, vol. 27, no. 11, pp.4445-4458, Nov. 2012.

[94] P. C. Loh, D. Li, Y. K. Chai, and F. Blaabjerg, "Hybrid AC-DC Microgrids With Energy Storages and Progressive Energy Flow Tuning," *IEEE Trans. Power Electronics*, vol. 28, no. 4, pp.1533-1543, Apr. 2013.

[95] Xu, and D. Chen, "Control and Operation of a DC Microgrid with Variable Generation and Energy Storage," *IEEE Trans. Power Delivery*, vol. 26, no. 4, pp. 2513-2522, Oct. 2011.

[96] T. Dragicevic, J. M. Guerrero, J. C. Vasquez, and D. Skrlec, "Supervisory Control of an Adaptive-Droop Regulated DC Microgrid With Battery Management Capability," *IEEE Trans. Power Electronics*, vol. 29, no.2, pp.695-706, Feb. 2014.

[97] S. Piller, M. Perrin, and A. Jossen, "Methods for state-of-charge determination and their applications," *Journal of Power Sources*, no. 96, pp.113-120, 2001.

[98] M. Charkhgard, and M. Farrokhi, "State-of-Charge Estimation for Lithium-Ion Batteries using Neural Networks and EKF," *IEEE Trans. Industrial Electronics*, vol. 57, no. 12, pp.4178-4187, Dec. 2010

[99] A. Kwasinski, and P. T. Krein, "Stabilization of Constant Power Loads in DC-DC Converters using Passivity-Based Control," in *Proc. Int'l Telecommunications Energy Conference (INTELEC),* 2007, pp.867-874.

[100] A. Kwasinski, and P. T. Krein, "Passivity-Based Control of Buck Converters with Constant-Power Loads," in *Proc. Power Electronics Specialists Conference (PESC),* 2007, pp.259-265.

[101] D. Chen, L. Xu, and L. Yao, "DC Voltage Variation Based Autonomous Control of DC Microgrids," *IEEE Trans. Power Delivery*, vol. 28, no. 2, pp. 637-647, Apr. 2013.

[102] A. Mohamed, V. Salehi, and O. Mohammed, "Real-Time Energy Management Algorithm for Mitigation of Pulse Loads in Hybrid Microgrids," *IEEE Trans. Smart Grid*, vol. 3, no. 4, pp. 1911-1922, Dec. 2012.

[103] M. Rodriguez, G. Stahl, L. Corradini, and D. Maksimovic, "Smart DC Power Management System based on Software-Configurable Power Modules," *IEEE Trans. Power Electronics,* vol. 28, no. 4, pp. 1571-1586, Apr. 2013.

[104] X. Feng, J. Liu, and F. Lee, "Impedance specifications for stable dc distributed power systems," *IEEE Trans. Power Electronics*, vol. 17, no. 2, pp. 157-162, Mar. 2002.

[105] X. Wang, F. Blaabjerg, and W. Wu, "Modeling and Analysis of Harmonic Stability in an AC Power-Electronics-Based Power System," *IEEE Trans. Power Electronics*, vol. 29, no. 12, Dec. 2014, pp.6421-6432.

[106] C. N. Onwuchekwa, and A. Kwasinski, "Dynamic Behavior of Single-Phase Full-Wave Uncontrolled Rectifiers with Instantaneous Constant-Power Loads," in *Proc. IEEE Energy Conversion Congress and Exposition (ECCE)* 2011, pp. 3472-3479.

[107] J. G. Kassakian, and T. M. Jahns, "Evolving and Emerging Applications of Power Electronics in Systems," *IEEE Journal of Emerging and Selected Topics in Power Electronics*, vol. 1, no. 2, pp.47-58, Jun. 2013.

[108] I. Moir, and A. G. Seabridge, *Military Avionics Systems*, John Wiley & Sons, 2006.

[109] J. Song, V. Krishnamurthy, A. Kwasinski, and R. Sharma, "Development of a Markov-Chain-Based Energy Storage Model for Power Supply Availability Assessment of Photovoltaic Generation Plants," *IEEE Trans. Sustainable Energy*, vol. 4, no. 2, pp. 491-500, Apr. 2013.

[110] J. D. Glover, M. S. Sarma, and T. J. Overbye, *Power System Analysis and Design*, Thomson, 2008

[111] P. Nuutinen, P. Peltoniemi, and P. Silventoninen, "Short-Circuit Protection in a Converter-Fed Low-Voltage Distribution Network," *IEEE Trans. Power Electronics*, vol. 28, no.4, pp. 1587-1597, Apr. 2013.

[112] V. Krishnamurthy, and A. Kwasinski, "Microgrid Performance during Extreme Events: Grid Availability," in Proc. *Microgrid RODEO (Research on Distributed Electricity Operations) Summit*, 2014.

[113] A. Kwasinski, "Local Energy Storage as a Decoupling Mechanism for Interdependent Infrastructures," in *Proc. Int'l Systems Conference* (SysCon) 2011, pp.435-441.

[114] (Dec. 2013). Ponemon Institute Research Report, *2013 Cost of Data Center Outages*.

[115] M. Kim, A. Kwasinski, and V. Krishnamurthy, "A Storage Integrated Power Electronic Interface for Higher Power Distribution Availability," *IEEE Trans. Power Electronics*, vol. 30, no. 5, May 2015, pp.2645-2659.

[116] D. J. Lee, and L. Wang, "Small-Signal Stability Analysis of an Autonomous Hybrid Renewable Energy Power Generation/Energy Storage System Part 1: Time-Domain Simulations," *IEEE Trans. Energy Conversion*, vol. 23, no. 1, pp.311-320, Mar. 2008.

[117] S. Dasgupta, S. N. Mohan, S. K. Sahoo, and S. K. Panda, "A Plug and Play Operational Approach for Implementation of an Autonomous-Micro-Grid System," *IEEE Trans. Industrial Informatics*, vol. 8, no. 3, Aug. 2012, pp.615-629.

[118] M. Kim, and A. Kwasinski, "Decentralized Hierarchical Control of Active Power Distribution Nodes," *IEEE Trans. Energy Conversion*, vol. 29, no. 4, Dec. 2014, pp.934-943.

[119] J. Schiffer, D. Goldin, J. Raisch, and T. Sezi, "Synchronization of droop-controlled microgrids with distributed rotational and electronic generation," in *Proc. 52nd Annual Conf. on Decision and Control (CDC)* 2013, pp.2334-2339.

[120] S. D'Arco, and J. A. Sul, "Equivalence of Virtual Synchronous Machines and Frequency-Droops for Converter-Based Microgrids," *IEEE Trans. Smart Grid*, vol. 5, no.1, pp.394-395, Jan. 2014.

[121] M. H. J. Bollen, and F. Hassan, *Integration of Distributed Generation in the Power System*, Wiley-Press, 2011.

[122] N. Pogaku, M. Prodanovic, and T. C. Green, "Modeling, Analysis, and Testing of Autonomous Operation of an Inverter-Based Microgrid," *IEEE Trans. Power Electronics*, vol. 22, no. 2, pp.617-625, Mar. 2007.

[123] A. A. A. Radwan, and Y. A.-R. I. Mohamed, "Analysis and Active-Impedance-Based Stabilization of Voltage-Source Rectifiers Loads in Grid-Connected and Isolated Microgrid Applications," *IEEE Trans. Sustainable Energy,* vol. 4, no. 3, Jul. 2013, pp.563-576.

[124] J. O'Sullivan, A. Rogers, D. Flynn, P. Smith, A. Mullane, and M. O'Malley, "Studying the Maximum Instantaneous Non-Synchronous Generation in an Island

System- Frequency Stability Challenges in Ireland," *IEEE Trans. Power Systems*, vol. 29, no.6, pp.2943-2951, Nov. 2014.

[125] M. Kim, and A. Kwasinski, "Stability Characterization of Inverter based Microgrids considering Configuration changes," to be presented at *European Conference on Power Electronics and Applications (EPE 2015-ECCE Europe),* 2015.

[126] J. Liu, Y. Miura, and T. Ise, "Dynamic Characteristics and Stability Comparisons between Virtual Synchronous Generator and Droop Control in Inverter-based Distributed Generators," in *Proc. of Int'l Power Electronics Conference (IPEC)* 2014, pp.1536-1543.

[127] I. P. Nikolakakos, I. A. Al-Zyoud, H. H. Zeineldin, M. S. El-Moursi, and A. S. Al-Hinai, " Enhancement of Islanded Droop-Controlled Microgrid Performance via Power Filter Design," in *Proc. of IEEE Power & Energy Society General Meeting (PES),* 2014, pp.1-5.

[128] M. A. Torres L., L. A. C. Lopes, L. A. Moran T, J. R. Espinoza C, "Self-Tuning Virtual Synchronous Machine: A Control Strategy for Energy Storage Systems to Support Dynamic Frequency Control," *IEEE Trans. Energy Conversion*, vol. 29, no. 4, pp.833-840, Dec. 2014.